

ENGINEERING PROTEIN-BASED BIOMATERIALS WITH BIOLOGICAL
AND MECHANICAL CUES TO DIRECT CELLULAR BEHAVIOR

Thesis by

Stacey Ann Maskarinec

In Partial Fulfillment of the Requirements

for the Degree of

Doctor of Philosophy

California Institute of Technology

Pasadena, CA

2009

(Defended March 17, 2009)

© 2009

Stacey A. Maskarinec

All Rights Reserved

Acknowledgements

I would like to thank my advisor, David Tirrell, for his tremendous support and guidance throughout my graduate work. I sincerely appreciate the intellectual independence that he fostered in the laboratory, and I hope to emulate his open-mindedness, creativity, and scientific rigor in my own career. I would also like to thank the members of my committee, Robert Grubbs, Anand Asthagiri, and Guruswami Ravichandran for their thoughtful comments and advice. I will always be extremely thankful for the experience of learning and working in Professor Ravichandran's laboratory, and for his kindness and unending encouragement. I am grateful for the opportunity to have spent the last five years at Caltech conducting research under the tutelage of such great scientists.

Thank you to all members of the Tirrell lab past and present. I have really enjoyed working in the lab with such great people and I am grateful for their friendship and scientific enthusiasm. In particular, I would like to thank Rebecca Connor for so many great memories, and for teaching me how to always approach science with a curious mind, perseverance, and humility. I would also like to thank Chethana Kulkarni, Julie Champion, and Shelly Tzlil for their kind support and advice both scientific and otherwise.

A portion of this work was performed in collaboration with Christian Frank, an amazing graduate student in Professor Ravichandran's laboratory. I thank him for all his hard work, dedication, patience, and for teaching me, several times, the basics of mechanics. Most of all, I thank him for his friendship.

This work would not be possible without the help from fantastic support staff at Caltech. I am thankful to Rochelle Diamond in the flow cytometry facility, and the staff at the Proteomic Exploration Laboratory, especially Geoff Smith and Mike Sweredoski. I deeply appreciate all the time and effort they spent teaching me how to perform proteomic research.

I am truly lucky to have made some wonderful friends at Caltech – Melissa Pope, Katie Brenner, Katie Galloway, and Sarah DeFusco. Sharing funny stories about life and work every Thursday at lunch has been a great source of strength, support, and balance for me during my graduate work.

Finally, my deepest gratitude goes to my family, especially my parents and my husband. I thank my parents for their unfailing love, encouragement, patience, and for all the sacrifices they made for me to have such wonderful opportunities. Any accomplishment that I have made has been because they gave me the courage and better-designed wings. And to my husband, Derek, I am so grateful for his unconditional love, and for encouraging me to strive to fulfill all my hopes and dreams. I thank him for always believing in me.

Abstract

Biomaterials play critical roles in tissue engineering, reconstructive surgery, and regenerative medicine. Constructing biomaterials through protein engineering offers a unique and powerful solution to the challenges posed by the creation of well-defined, multi-functional materials that must provide structural support, as well as guide cell and tissue behavior. This thesis describes the construction, characterization, and application of protein-based biomaterials composed of photoreactive artificial extracellular matrix (aECM) proteins. These proteins consist of mechanical and biological motifs derived from natural proteins: an elastin-like backbone containing a photocrosslinking site dictates the mechanical properties of the material, and an RGD binding domain from fibronectin mediates cell attachment. aECM proteins were assembled at the genetic level and expressed in a bacterial host. Manipulation of an aminoacyl-tRNA synthetase of the expression strain permitted the incorporation of the photoreactive noncanonical amino acid, *para*-azidophenylalanine (pN_3Phe), within the elastin subunit of the protein.

An evaluation of the mechanical and biological properties of photoreactive aECM proteins has been performed. Nanoindentation experiments using atomic force microscopy (AFM) demonstrated that the elastic moduli of photocrosslinked protein films lie within the range of native elastins and that the mechanical properties of films can be tuned by altering the incorporation of pN_3Phe in the protein or adjusting the irradiation dosage. Cell spreading experiments showed that cell attachment to protein films is sequence-specific to the presence of the RGD cell-binding domain. Patterning of protein films using standard photolithography methods allowed for the generation of cellular arrays.

A molecular characterization of cellular response to engineered aECM proteins has been initiated using mRNA microarrays and the proteomic technique, BONCAT (bio-orthogonal noncanonical amino acid tagging). These methods provide information regarding changes in the cellular expression of mRNA transcripts and proteins in response to the biochemical composition of protein-based materials.

Cell-mediated deformation of the extracellular matrix in all three spatial dimensions was tracked and quantified using a newly developed method that combines time-lapse laser scanning confocal imaging and digital volume correlation. Analysis of the displacement profiles of migrating cells illustrates that, in addition to in-plane (x,y) forces, cells also exert significant normal (z) forces. A new “push-pull” aspect of cell migration was detected in the normal displacement profiles of monitored cells suggesting that cells simultaneously “push” and “pull” the underlying matrix while exploring their microenvironment.

Table of Contents

Acknowledgements	iii
Abstract	v
1 Introduction	1
1.1 Designing functional biomaterials	2
1.2 The role of mechanical properties in biomaterials design	3
1.2.1 Elastin-like polypeptides	3
1.2.2 Crosslinking mechanisms	4
1.2.3 Controlled degradability of structural scaffolds	5
1.2.4 Effect of mechanical properties on cellular behavior	5
1.3 The role of biochemical properties in biomaterials design	7
1.3.1 Choice of adhesive proteins and peptide domains	7
1.3.2 Density and presentation of active protein and peptide domains	8
1.3.3 Temporally controlled presentation of active proteins and peptide domains	10
1.4 Outline of thesis	12
1.5 References	14
2 Design and Construction of Photoreactive Artificial Extracellular Matrix Proteins	19
2.1 Abstract	20
2.2 Introduction	22
2.3 Materials and Methods	24
2.3.1 Cloning of photoreactive aECM proteins	24
2.3.2 Protein expression and purification	28
2.3.3 aECM protein characterization	29
2.3.4 Preparation of photocrosslinked films for cell studies and mechanical testing ..	30
2.3.5 Cell maintenance	32
2.3.6 Cell spreading experiments	32
2.3.7 AFM equipment	33
2.3.8 AFM measurements: film thickness and force curves	34
2.4 Results and Discussion	35
2.4.1 Characterization of aECM proteins	35
2.4.2 PEGylated and photocrosslinked aECM films for cell studies	38
2.4.3 Cell spreading results	39
2.4.4 AFM results: film thickness and elastic moduli measurements	40
2.5 Conclusions	42
2.6 References	44
3 Lithographic Patterning of Photoreactive Cell-Adhesive Proteins	48
3.1 Abstract	49
3.2 Introduction	50
3.3 Materials and Methods	51
3.3.1 Cloning of aECM-N ₃ constructs	51
3.3.2 Protein expression and purification	52
3.3.3 Mechanical testing	53
3.3.4 Photolithographic patterning of aECM-N ₃ proteins	53
3.3.5 Cell culture	54
3.3.6 Cell patterning	55

3.3.7	Cell spreading	56
3.3.8	Atomic force microscopy	57
3.4	Results and Discussion	57
3.4.1	Expression and characterization of aECM-N ₃ proteins	57
3.4.2	Kinetics of photodecomposition	59
3.4.3	Mechanical testing	60
3.4.4	Cell patterning	60
3.4.5	Cell spreading	62
3.5	Conclusions	63
3.6	Acknowledgements	63
3.7	References	64
4	Towards Exploring the Proteomic Profile of Rat-1 Fibroblasts on Artificial Extracellular Matrix Proteins	68
4.1	Abstract	69
4.2	Introduction	70
4.3	Materials and Methods	75
4.3.1	Cell culture	75
4.3.2	Cell synchronization through contact inhibition	76
4.3.3	aECM protein expression and purification	76
4.3.4	Cell spreading experiments	77
4.3.5	Microarray analysis	78
4.3.6	Cell lysis and protein extraction for proteomic analysis	79
4.3.7	Affinity purification	80
4.3.8	Sample preparation for tandem mass spectrometry analysis	81
4.3.9	Analysis of tandem mass spectrometry data	83
4.4	Results and Discussion	84
4.4.1	Cell synchronization through contact inhibition	84
4.4.2	Cell spreading results	85
4.4.3	mRNA microarray results	87
4.4.4	BONCAT results	90
4.5	Conclusions and Future Work	94
4.6	References	97
5	Depth Perception: Quantifying Cellular Traction Forces in Three Dimensions	101
5.1	Abstract	102
5.2	Introduction	103
5.3	Materials and Methods	106
5.3.1	Preparation of activated coverslips	106
5.3.2	Preparation of polyacrylamide films	106
5.3.3	Functionalization of polyacrylamide films with fibronectin	107
5.3.4	Characterization of FN-modified films	108
5.3.5	Film thickness measurements	109
5.3.6	Mechanical characterization of thin films	109
5.3.7	Cell culture	110
5.3.8	Confocal microscopy and time-lapse imaging	111
5.3.9	Calculation of displacements, strains, stresses, and forces	112
5.3.10	Traction force inhibition using blebbistatin	113

5.4	Results and Discussion.....	113
5.4.1	Characterization of FN-modified films	113
5.4.2	Mechanical Testing	113
5.4.3	Analysis of cellular traction forces in 3D: in-plane and normal components ..	116
5.4.4	Analysis of cellular traction forces in 3D: a time evolution of the force components.....	119
5.4.5	Analysis of cellular traction forces in 3D: “push-pull” phenomena	121
5.4.6	Traction force inhibition with blebbistatin	124
5.5	Conclusions	125
5.6	References	125
6	Conclusion.....	129
6.1	Summary	130
6.2	Future Directions	131
6.3	References	132
	Appendix A	134
	Appendix B	167
	Appendix C	206

List of Figures

Figure 2-1. Photoreactive aECM protein sequences	24
Figure 2-2. Schematic of the protocol for cloning aECM proteins	25
Figure 2-3. SDS-PAGE analysis of the purification of aECM proteins	35
Figure 2-4. LC-MS spectra of purified (A) RGD-N ₃ and (B) RDG-N ₃ proteins	37
Figure 2-5. HUVEC spread areas on (A) fibronectin; positive control, (B) BSA; negative control, (C) RGD-N ₃ , and (D) RDG-N ₃	39
Figure 2-6. AFM topography scans of photocrosslinked RGD-N ₃ protein	40
Figure 2-7. Representative loading indentation profiles for thin films of photocrosslinked RGD-N ₃ protein	42
Figure 3-1. Characteristics of aECM-N ₃ proteins	51
Figure 3-2. Representative ¹ H NMR spectra of an aECM-N ₃ construct expressed in media supplemented with phenylalanine or with <i>p</i> N ₃ Phe	58
Figure 3-3. Incorporation of <i>p</i> N ₃ Phe into the CS5-N ₃ protein as a function of concentration in the expression medium	59
Figure 3-4. AFM images of patterned RGD-N ₃	61
Figure 3-5. Confocal microscopy of Rat-1 fibroblasts attached to photopatterned RGD-N ₃	62
Figure 3-6. Rat-1 fibroblast cell spread areas on (A) fibronectin, (B) BSA, (C) RGD-N ₃ , and (D) RDG-N ₃	63
Figure 4-1. aECM protein sequences	73
Figure 4-2. Schematic of BONCAT methodology	74
Figure 4-3. Chemical structures of methionine (Met) and azidohomoalanine (Aha)	75
Figure 4-4. FACS analysis of Rat-1 fibroblasts before (A) and after (B) cell synchronization by contact inhibition	85
Figure 4-5. Images of cells captured after 2 hours of spreading	86
Figure 4-6. Rat-1 cell spread areas on (A) FN, (B) BSA, (C) RGD-N ₃ , (D) RDG-N ₃	87
Figure 4-7. Gene ontology analysis of newly synthesized proteins in Aha-treated samples using DAVID	93
Figure 4-8. Pathway analysis of the imported list from Aha-treated samples using DAVID	94
Figure 5-1. Schematic of a representative gel sample with microscope objective	105
Figure 5-2. Detailed schematic of the compression tests	110
Figure 5-3. Incremental loading tests using polyacrylamide samples	114
Figure 5-4. Representative stress-strain curves of loading and unloading cycles on cylindrical hydrated polyacrylamide samples	114
Figure 5-5. Displacement contour slices along the long axis of the cell and corresponding line plots as a function of depth for samples of varying heights	118
Figure 5-6. Time evolution of displacement and traction force contours during cell migration for a single cell	120
Figure 5-7. 3-D “push-pull” phenomenon observed in the z-plane displacement profiles of tracked cells	123
Figure 5-8. Traction force inhibition using blebbistatin	124

List of Tables

Table 2-1. Theoretical and measured amino acid compositions of RGD-N ₃ and RDG-N ₃ proteins.....	38
Table 4-1. Selected list of differentially expressed mRNA transcripts from ratio experiments with FN, RGD-N ₃ , and RDG-N ₃ samples	90
Table 4-2. List of identified newly synthesized proteins shown to play a role in cell-ECM interactions, focal adhesion formation, and cytoskeletal reorganization.....	92
Table 5-1. Mechanical characterization results for polyacrylamide substrates from unconfined uniaxial compression experiments	115

1 Introduction

Portions of this text are taken from:

Maskarinec, S.A., and D.A. Tirrell, *Protein Engineering Approaches to Biomaterials Design*. Current Opinion in Biotechnology, 2005. **16(4)**: 422-426.

Reproduced with permission of publisher.

1.1 Designing functional biomaterials

The design of functional biomaterials that elicit specific cellular behavior constitutes a major challenge for the fields of tissue engineering and materials science. Efforts to develop such materials have principally involved the design of scaffolds and hydrogels to mimic the dynamic interactions between cells and the extracellular matrix *in vivo* [1, 2], and the incorporation of extracellular adhesion ligands and growth factors into engineered materials has proven effective in directing cellular response in many applications [3-5]. Innovative methods to fabricate “smart,” or stimuli-responsive, biomaterials that react to cell-mediated processes or to environmental changes in pH or temperature have allowed materials to play more interactive roles in tissue morphogenesis [6, 7]. In order to construct materials that promote specific cellular fates, it is essential to assert greater control over both the structural properties and biochemical characteristics of these materials.

In this context, the use of protein-based biomaterials provides a uniquely powerful approach to the control of macromolecular structure and function. The growing ease of expression of recombinant protein polymers promises to expand the use of protein-based materials, both in the investigation of basic cellular processes and in therapeutic applications. Advances in microfabrication technology and controlled release systems have also expanded the possibilities for control of the spatial and temporal patterns in which proteins can be presented to cells [8]. These methods have yielded important new insights into the mechanisms by which cells sense and respond to signals, and have enhanced substantially the repertoire of techniques available for materials design.

In comparison with other areas of protein engineering, biomaterials design presents unique challenges because of the crucial role of mechanical behavior in determining success or failure in materials applications. Materials design often begins with consideration of mechanical behavior – identifying and optimizing the properties needed to produce stable platforms for tissue replacement or regeneration. The biological properties of the material are then modified to enhance tissue specificity, cellular activity and biocompatibility.

1.2 The role of mechanical properties in biomaterials design

1.2.1 Elastin-like polypeptides

Materials for use in tissue engineering must provide structure and support to regenerating tissue while accommodating cellular infiltration and homeostasis. A logical strategy for the design of synthetic materials with the requisite mechanical properties utilizes structural motifs derived from extracellular matrix proteins [9]. Artificial proteins incorporating elastin-like polypeptides represent a class of materials whose physical properties are remarkably similar to those of native elastin. Moreover, these proteins are tunable at the genetic level to match the requirements of specific applications [10, 11]. For example, repeats of elastin-like polypeptides (ELP) with the amino acid sequence (VPGZG)_x, where Z is any amino acid except proline, have been developed for use in vascular grafts. Lysine residues have been encoded at regular intervals in such protein sequences to allow for crosslinking by difunctional electrophiles. Variation in the stoichiometric ratio of crosslinker and protein enabled the preparation of films with moduli spanning the range reported for native elastins [11, 12].

Similar ELPs have been engineered to function as injectable scaffolds for cartilaginous tissue repair [13]. Thermally responsive ELPs were designed to exhibit liquid-like behavior at room temperature, permitting simple suspension of chondrocytes; however, upon reaching physiological temperatures (*in situ* upon injection), the ELP mixture aggregates into a stiff gel-like coacervate. Cells become entrapped within an elastic three-dimensional matrix with mechanical properties comparable to those reported for collagen and hyaluronan-based scaffolds commonly used to promote cartilage regeneration [13]. Since the physical properties of ELPs are genetically encodable, the potential exists for the formulation of specialty ELPs to augment healing in specific cartilaginous tissues that are prone to injury.

1.2.2 Crosslinking mechanisms

Another approach to modulating the mechanical properties of protein-based materials involves the use of defined crosslinking reactions. To facilitate site-specific solid-state crosslinking using both UV and visible light photoinitiators, Nagapudi and coworkers functionalized the lysine residues of elastin-like polypeptide repeats with acrylate moieties [14]. Electrospinning of these proteins into fibers followed by photoirradiation produced highly extensible networks appropriate for cell culture. Elbjerrami et al. reported a similar enhancement in the mechanical properties of collagen gels through lysyl oxidase (LO) mediated crosslinking. Gels seeded with LO-transfected vascular smooth muscle cells exhibited nearly a two-fold increase in both the elastic modulus and tensile strength as compared to scaffolds containing mock-transfected cells [15].

1.2.3 *Controlled degradability of structural scaffolds*

Scaffold degradation can be synchronized with cellular repair such that materials can be replaced by functional tissue over a time interval that minimizes structural destabilization. The use of recombinant proteins in biomaterials offers this additional design advantage, since proteins can be engineered to incorporate amino acid sequences that are susceptible to selected cellular proteases. Halstenberg and coworkers functionalized poly(ethylene glycol) (PEG)-based hydrogels with an engineered artificial protein containing two plasmin degradation sites, a heparin binding site, an RGD binding motif to promote cell adhesion, and repeating amino acid sequences based on fibrinogen and antithrombin III [16]. The resulting hydrogel facilitated sequence-specific cellular adhesion through the RGD domain, possessed serine-protease degradability, and exhibited mechanical integrity adequate to sustain cellular growth *in vitro* on a timescale comparable to those of normal wound healing processes. Similarly, specific elastase target sequences were cloned into protein polymers to allow for programmed turnover of these matrices by cell-mediated processes [17, 18]. The elastase cut site was strategically placed within the artificial protein to allow for liberation of a hexapeptide known to promote cellular proliferation and wound healing responses.

1.2.4 *Effect of mechanical properties on cellular behavior*

In addition to their crucial role in providing structural support, the mechanical properties of biomaterials have been shown to impact cellular behavior [19]. The efficacy of several silk and collagen based substrates to support chondrogenesis of cultured human mesenchymal stem cells (hMSC) was found to be influenced primarily by scaffold

degradation rates rather than by chemical composition [19]. Samples of crosslinked collagen and slowly degrading silks promoted cell differentiation and matrix deposition whereas uncrosslinked collagen samples collapsed prematurely and were unable to support significant cartilaginous tissue formation.

This observation, in concert with others that demonstrate the connection between substrate mechanics and cellular response, has prompted investigators to examine the use of spatial variation in mechanical properties as a design strategy for engineered materials. Gray and coworkers produced fibronectin-coated polymeric substrates containing micropatterned square islands of increased stiffness and observed that cells initially plated uniformly over the surface reposition themselves on the rigid islands of the substrate over the course of several days [20]. Mechanically-directed migration has also been observed on gradient-compliant photocrosslinkable polyacrylamide-based hydrogels [21]. For vascular smooth muscle cells cultured on these gradient substrates, preferential migration was exhibited toward the region of highest elastic modulus, whereas cells distributed on uniformly compliant substrates displayed no such directional movement. As indicated by the authors, the substantial accumulation of cells on stiffer portions of the substrate suggests that the detailed nature of the gradient pattern may be important in controlling the extent of cell migration [21, 22]. More recently, mechanical gradients have been used to manipulate other cellular processes including attachment and spreading [23].

1.3 The role of biochemical properties in biomaterials design

Protein-based materials offer special advantages for providing biochemical instructions to guide cellular behavior, in that the identity and presentation of bioactive ligands may be engineered to elicit various cellular phenotypes. In establishing qualitative design strategies for the fabrication of biomaterials, three general approaches have emerged to induce cellular behavior and guide tissue morphogenesis using both naturally and artificially derived proteins: altering the identity of adhesive proteins and peptide domains; modulating the density and spatial presentation of proteins and peptide domains; and optimizing the temporally controlled presentation of proteins and peptide domains.

1.3.1 *Choice of adhesive proteins and peptide domains*

A dominant theme in biomaterials research over the past decade has addressed the judicious inclusion of adhesion ligands that interact with specific cellular receptors. Heilshorn and coworkers have reported artificial extracellular matrix (aECM) proteins in which elastin-like sequences alternate with CS5 cell binding domains derived from fibronectin to enable adhesion of human umbilical vein endothelial cells (HUVEC) through the $\alpha_4\beta_1$ integrin [24]. Incorporation of the CS5 domain facilitated sequence-specific adhesion to aECM proteins and sustained cellular attachment under dynamic stresses characteristic of the vascular system. In a companion study, Liu et al. were able to increase both the rate and extent of cell spreading and attachment on similar aECM proteins by replacing the CS5 ligand with the well-characterized RGD cell binding domain [25]. HUVEC formed focal adhesions and normal stress fibers on the RGD-

modified surfaces through the $\alpha_v\beta_3$ integrin, demonstrating that cellular response to aECM proteins can be modulated by the careful selection of cell binding domains that foster distinct ligand-receptor interactions. In a related approach, the adhesive pentapeptide YIGSR was incorporated into a dually modified polyurethaneurea-based material designed by Jun and West to promote endothelialization through specific adhesion receptors [26]. The second modification involved the use of PEG chains as soft segments in the polymer to limit nonspecific platelet and protein adhesion.

Targeting the adhesion of a particular cell type to a material surface has also been achieved by using a non-integrin based ligand. Gobin et al. grafted the elastin-derived amino acid sequence VAPG, known to bind to a peripheral membrane receptor on smooth muscle cells, into photopolymerizable hydrogels based on acrylate-terminated derivatives of PEG [27]. Inclusion of the VAPG sequence promoted the specific adhesion of vascular smooth muscle cells while deterring adhesion of endothelial cells, fibroblasts, and platelets.

1.3.2 Density and presentation of active protein and peptide domains

Cellular processes including adhesion, migration, and proliferation are strongly influenced by the surface density as well as the spatial distribution of bioactive domains [8, 28]. Gaudet and coworkers recently demonstrated that fibroblast spreading, motility, and contractility could be modulated by varying collagen surface densities. Interestingly, as collagen surface density was increased, cell spreading did not increase as expected, but rather decreased, suggesting that beyond a certain collagen surface density fibroblasts interact differently with the underlying substrate [29]. This transition density or threshold

concentration matched the average calculated density of cell surface integrin receptors, a result that supports the notion that increased cell spreading is precluded by saturation of available cell surface integrin receptors.

Heilshorn and coworkers investigated the importance of cell-binding domain context on cell adhesion and spreading on engineered aECM proteins containing crosslinking sites located either within the interior or within the terminal portions of the protein chains [30]. Terminally crosslinked aECM proteins supported robust cell spreading and adhesion. However, crosslinking at sites within the repeating units of the protein resulted in a notable decrease in cellular response, suggesting that protein modification remote from the putative receptor-binding sequence could result in conformational changes affecting ligand affinity or accessibility. In order to probe the effects of protein conformation and context on cell adhesion, the Mrksich group developed a generalized model system that allows for control of the density, patterning, and orientation of immobilized engineered fusion proteins presented on a surface [31]. The engineered protein of interest comprises the 10th domain of fibronectin (for cell adhesion) fused to the serine esterase cutinase which reacts to form a covalent adduct to a phosphonate ligand presented on tri(ethylene glycol)-terminated self-assembled monolayers (SAMs). This immobilization strategy minimizes unwanted protein-substrate contacts, and offers considerable versatility as a method for screening protein-cell interactions.

Control over the spatial presentation of protein ligands is an especially valuable tool for guiding morphogenetic processes that rely on gradient patterns for proper development. Although the influence of soluble gradients on cellular behavior has been

extensively characterized, cellular response to immobilized gradients has only recently been investigated. By using microfluidic devices, substrate-bound gradients of extracellular signaling molecules can be formed on scales relevant for cell studies [32, 33]. In introducing this technology, Whitesides and coworkers demonstrated that the axonal polarity of rat hippocampal neurons could be oriented along increasing surface density gradients of adsorbed laminin [34]. Kapur et al. observed that axonal specification and extension of pheochromocytoma cells could also be guided along an immobilized gradient of nerve growth factor in a manner akin to that observed with a gradient of the solubilized protein [35]. The surface gradient resulted in morphologically thicker neuronal processes as compared to those treated with the soluble growth factor, suggesting that cells may activate different response mechanisms depending on the method of gradient presentation.

In order to preserve gradient fidelity for long term cell studies, Gunawan and coworkers covalently immobilized counter gradients of collagen I and laminin on carboxy-terminated SAMs using active-ester linking chemistry [36]. The expression profiles of two cell cycle progression markers could be directly controlled by the local ratio of extracellular matrix proteins.

1.3.3 Temporally controlled presentation of active proteins and peptide domains

The growth and repair of many tissues is coordinated through the temporally controlled liberation of soluble signals such as growth factors [5]. Design of materials to regulate these dynamic processes has centered on the fabrication of controlled release systems with defined dose and delivery kinetics for the purpose of eliciting localized and

measurable cellular responses. Richardson and coworkers developed a polymeric scaffold that allows for the coordinated and sequential release of vascular endothelial growth factor (VEGF) and platelet-derived growth factor (PDGF) for use in therapeutic angiogenesis [37]. The two growth factors were incorporated into a single material by mixing pre-encapsulated PDGF microspheres with a particulate polymer mixture containing lyophilized VEGF before processing into a porous matrix. Mixing VEGF with polymer particles resulted in rapid release of this factor, initiating angiogenesis, while slow degradation of microspheres released PDGF to support vessel growth and maturation. Toward the same goal, Ehrbar et al. covalently attached a recombinant version of VEGF containing a protease sensitive cleavage site to fibrin gel matrices, allowing the rate of growth factor release to be regulated by local cellular enzymatic activity [38]. Cell-demanded release of VEGF from remodeled fibrin scaffolds increased the formation of structurally intact and morphologically regular vascular beds in embryonic chicken chorioallantoic membranes.

Karageorgiou and coworkers have reported covalent coupling of active growth factors to materials to allow for induction of cellular responses that require delivery of the factor for prolonged periods of time [39]. Immobilization of bone morphogenetic protein-2 (BMP-2) on silk scaffolds was found to be more effective in inducing osteogenic differentiation of bone marrow stromal cells than addition of soluble BMP-2 to the growth medium [40].

1.4 Outline of thesis

The goal of this thesis is to characterize the cellular response to both biological and mechanical cues presented in the form of artificial extracellular matrix (aECM) proteins. These aECM proteins consist of two carefully chosen components: an elastin-derived amino acid sequence, (VPGVG)_x, and a fibronectin-derived cell binding domain, RGD. A crosslinking site introduced into the (VPGVG)_x sequence dictates the mechanical properties of the protein films, while the RGD binding domain mediates cell attachment. Crosslinking is facilitated through the incorporation of the noncanonical amino acid, *para*-azidophenylalanine (*p*N₃Phe), into the elastin backbone. Irradiation of protein films with ultraviolet light initiates photocrosslinking within the material that can be tuned by adjusting the irradiation dosage or by controlling the extent of *p*N₃Phe incorporation in the protein. Chapter 2 outlines the design and construction of this protein as well as a negative control protein. Marissa Mock initiated the cloning work, and I completed the genetic assembly of both proteins and performed the expression and characterization. The cell spreading experiments were performed in collaboration with Julie Liu. I received technical advice from Paul Nowatzki regarding use of the AFM. I conducted the AFM work and wrote the chapter.

Chapter 3 demonstrates an application of the photoreactive aECM proteins using photolithographic techniques to generate protein patterns for directed cell attachment. Isaac Caricco, Sarah Heilshorn, and Marissa Mock originally developed this project, demonstrating the ability to pattern cells using another photoreactive aECM protein containing a CS5 binding domain. I developed a new photopatterning method to pattern RGD-based proteins and used these surfaces to create cellular arrays. I also demonstrated

that attachment to these protein patterns is sequence-specific to the RGD domain. Issac Caricco performed the mechanical characterization, and Christian Franck and Paul Nowatzki obtained the AFM data.

Chapter 4 focuses on the use of the proteomic technique BONCAT (bio-orthogonal noncanonical amino acid tagging), to identify newly synthesized proteins that are expressed when cells are deposited on aECM proteins and fibronectin. Jennifer Hodas and Daniela Dieterich designed and synthesized the disulfide tag (DST) used in the BONCAT experiments, and Jennifer Hodas developed the BONCAT DST protocol. Dr. Janek Szychowski synthesized the azidohomoalanine used in the experiments. I made modifications to the provided protocol in order to conduct cell spreading experiments, and all of the mass spectrometry work was performed at the Proteomic Exploration Laboratory at Caltech. I also conducted mRNA microarray analysis to quantify the extent of differential gene expression that results when cells are deposited on aECM proteins compared to fibronectin. Following mRNA extraction and purification, all microarray chips were prepped and scanned by the Millard and Muriel Jacobs Genetics and Genomics Laboratory at Caltech. I also performed cell spreading experiments on aECM proteins and fibronectin. Lastly, I analyzed the collected data and wrote the chapter.

Chapter 5 describes the tracking and quantification of cellular traction forces in three-dimensions using laser scanning confocal imaging and digital volume correlation. Time-lapse confocal imaging of migrating 3T3 fibroblasts on fibronectin (FN)-modified polyacrylamide gels of varying thickness revealed significant in-plane (x, y) and normal (z) displacements, demonstrating that cells exert forces in all three dimensions when exploring their extracellular environment. All of this work was performed in

collaboration with Christian Franck, an aeronautics graduate student in Professor Ravichandran's Laboratory at Caltech.

1.5 References

1. Kleinman, H.K., D. Philp, and M.P. Hoffman, *Role of the extracellular matrix in morphogenesis*. Current Opinion in Biotechnology, 2003. **14**(5): 526-532.
2. Hubbell, J.A., *Materials as morphogenetic guides in tissue engineering*. Current Opinion in Biotechnology, 2003. **14**(5): 551-558.
3. Griffith, L.G., and G. Naughton, *Tissue engineering - Current challenges and expanding opportunities*. Science, 2002. **295**(5557): 1009-1014.
4. Hirano, Y., and D.J. Mooney, *Peptide and protein presenting materials for tissue engineering*. Advanced Materials, 2004. **16**(1): 17-25.
5. Sakiyama-Elbert, S.E., and J.A. Hubbell, *Functional biomaterials: Design of novel biomaterials*. Annual Review of Materials Research, 2001. **31**: 183-201.
6. Anderson, D.G., J.A. Burdick, and R. Langer, *Materials science - Smart biomaterials*. Science, 2004. **305**(5692): 1923-1924.
7. Lutolf, M.P., and J.A. Hubbell, *Synthetic biomaterials as instructive extracellular microenvironments for morphogenesis in tissue engineering*. Nature Biotechnology, 2005. **23**(1): 47-55.
8. Raghavan, S., and C.S. Chen, *Micropatterned environments in cell biology*. Advanced Materials, 2004. **16**(15): 1303-1313.
9. van Hest, J.C.M., and D.A. Tirrell, *Protein-based materials, toward a new level of structural control*. Chemical Communications, 2001(19): 1897-1904.

10. Lee, J., C.W. Macosko, and D.W. Urry, *Mechanical properties of cross-linked synthetic elastomeric polypentapeptides*. *Macromolecules*, 2001. **34**(17): 5968-5974.
11. Di Zio, K., and D.A. Tirrell, *Mechanical properties of artificial protein matrices engineered for control of cell and tissue behavior*. *Macromolecules*, 2003. **36**(5): 1553-1558.
12. Nowatzki, P.J., and D.A. Tirrell, *Physical properties of artificial extracellular matrix protein films prepared by isocyanate crosslinking*. *Biomaterials*, 2004. **25**(7-8): 1261-1267.
13. Betre, H., et al., *Characterization of a genetically engineered elastin-like polypeptide for cartilaginous tissue repair*. *Biomacromolecules*, 2002. **3**(5): 910-916.
14. Nagapudi, K., et al., *Photomediated solid-state cross-linking of an elastin-mimetic recombinant protein polymer*. *Macromolecules*, 2002. **35**(5): 1730-1737.
15. Elbjeirami, W.M., et al., *Enhancing mechanical properties of tissue-engineered constructs via lysyl oxidase crosslinking activity*. *Journal of Biomedical Materials Research Part A*, 2003. **66A**(3): 513-521.
16. Halstenberg, S., et al., *Biologically engineered protein-graft-poly(ethylene glycol) hydrogels: A cell adhesive and plasmin-degradable biosynthetic material for tissue repair*. *Biomacromolecules*, 2002. **3**(4): 710-723.
17. Girotti, A., et al., *Design and bioproduction of a recombinant multi(bio)functional elastin-like protein polymer containing cell adhesion sequences for tissue*

- engineering purposes*. Journal of Materials Science-Materials in Medicine, 2004. **15**(4): 479-484.
18. Welsh, E.R., and D.A. Tirrell, *Engineering the extracellular matrix: A novel approach to polymeric biomaterials. I. Control of the physical properties of artificial protein matrices designed to support adhesion of vascular endothelial cells*. Biomacromolecules, 2000. **1**(1): 23-30.
 19. Meinel, L., et al., *Engineering cartilage-like tissue using human mesenchymal stem cells and silk protein scaffolds*. Biotechnology and Bioengineering, 2004. **88**(3): 379-391.
 20. Gray, D.S., J. Tien, and C.S. Chen, *Repositioning of cells by mechanotaxis on surfaces with micropatterned Young's modulus*. Journal of Biomedical Materials Research Part A, 2003. **66A**(3): 605-614.
 21. Wong, J.Y., et al., *Directed movement of vascular smooth muscle cells on gradient-compliant hydrogels*. Langmuir, 2003. **19**(5): p. 1908-1913.
 22. Lo, C.M., et al., *Cell movement is guided by the rigidity of the substrate*. Biophysical Journal, 2000. **79**(1): p. 144-152.
 23. Zaari, N., et al., *Photopolymerization in microfluidic gradient generators: Microscale control of substrate compliance to manipulate cell response*. Advanced Materials, 2004. **16**(23-24): p. 2133-2137.
 24. Heilshorn, S.C., et al., *Endothelial cell adhesion to the fibronectin CS5 domain in artificial extracellular matrix proteins*. Biomaterials, 2003. **24**(23): p. 4245-4252.

25. Liu, J.C., S.C. Heilshorn, and D.A. Tirrell, *Comparative cell response to artificial extracellular matrix proteins containing the RGD and CS5 cell-binding domains*. Biomacromolecules, 2004. **5**(2): 497-504.
26. Jun, H.W., and J.L. West, *Modification of polyurethaneurea with PEG and YIGSR peptide to enhance endothelialization without platelet adhesion*. Journal of Biomedical Materials Research Part B-Applied Biomaterials, 2005. **72B**(1): 131-139.
27. Gobin, A.S., and J.L. West, *Val-ala-pro-gly, an elastin-derived non-integrin ligand: Smooth muscle cell adhesion and specificity*. Journal of Biomedical Materials Research Part A, 2003. **67A**(1): p. 255-259.
28. Koo, L.Y., et al., *Co-regulation of cell adhesion by nanoscale RGD organization and mechanical stimulus*. Journal of Cell Science, 2002. **115**(7): 1423-1433.
29. Gaudet, C., et al., *Influence of type I collagen surface density on fibroblast spreading, motility, and contractility*. Biophysical Journal, 2003. **85**(5): 3329-3335.
30. Heilshorn, S.C., J.C. Liu, and D.A. Tirrell, *Cell-binding domain context affects cell behavior on engineered proteins*. Biomacromolecules, 2005. **6**(1): 318-323.
31. Murphy, W.L., et al., *Substrates for cell adhesion prepared via active site-directed immobilization of a protein domain*. Langmuir, 2004. **20**(4): 1026-1030.
32. Jeon, N.L., et al., *Generation of solution and surface gradients using microfluidic systems*. Langmuir, 2000. **16**(22): 8311-8316.

33. Jeon, N.L., et al., *Neutrophil chemotaxis in linear and complex gradients of interleukin-8 formed in a microfabricated device*. Nature Biotechnology, 2002. **20**(8): 826-830.
34. Dertinger, S.K.W., et al., *Gradients of substrate-bound laminin orient axonal specification of neurons*. Proceedings of the National Academy of Sciences of the United States of America, 2002. **99**(20): 12542-12547.
35. Kapur, T.A., and M.S. Shoichet, *Immobilized concentration gradients of nerve growth factor guide neurite outgrowth*. Journal of Biomedical Materials Research Part A, 2004. **68A**(2): 235-243.
36. Gunawan, R.C., et al., *Regiospecific control of protein expression in cells cultured on two-component counter gradients of extracellular matrix proteins*. Langmuir, 2005. **21**(7): 3061-3068.
37. Richardson, T.P., et al., *Polymeric system for dual growth factor delivery*. Nature Biotechnology, 2001. **19**(11): 1029-1034.
38. Ehrbar, M., et al., *Cell-demanded liberation of VEGF(121) from fibrin implants induces local and controlled blood vessel growth*. Circulation Research, 2004. **94**(8): 1124-1132.
39. Karageorgiou, V., et al., *Bone morphogenetic protein-2 decorated silk fibroin films induce osteogenic differentiation of human bone marrow stromal cells*. Journal of Biomedical Materials Research Part A, 2004. **71A**(3): 528-537.

2 Design and Construction of Photoreactive Artificial Extracellular Matrix Proteins

2.1 Abstract

In vivo, cells integrate a complex set of physical and chemical signals as well as spatial gradients of these signals to maintain proper tissue function. There has been much progress in the artificial replication of these cellular microenvironments by producing substrates with either tailored surface chemistries or regions of variable substrate rigidity, yet there has been minimal advancement in the design of materials that allow for the modulation of both properties simultaneously to study and direct cellular response. The work described here begins to address this challenge through the fabrication of photoreactive artificial extracellular matrix (aECM) proteins with independently tunable chemical and mechanical properties. These aECM proteins consist of two carefully chosen components: an elastin-derived amino acid sequence (VPGVG)_x, and a fibronectin-derived cell-binding domain, RGD. A crosslinking site introduced into the (VPGVG)_x sequence dictates the mechanical properties of protein films, while the RGD binding domain mediates cell attachment. The unique construction of the aECM proteins allows both the mechanical (elastic modulus) and chemical (cell-binding domain density) properties of the films to be varied in concert to evaluate the impact of multiple cues on cellular behavior.

aECM proteins were genetically engineered using recombinant DNA technologies and produced in an *Escherichia coli* expression host. Manipulation of an aminoacyl-tRNA synthetase of the bacterial expression strain permitted the incorporation of a non-canonical amino acid, *para*-azidophenylalanine (*p*N₃Phe), within the elastin subunit of the protein. Cell experiments using photocrosslinked aECM proteins demonstrated that HUVEC (human umbilical vein endothelial cells) attachment to these surfaces was

sequence-specific to the adhesive RGD sequence present within the protein. Additionally, micromechanical measurements of aECM films using atomic force microscopy (AFM) were performed to determine the elastic modulus (E) of these materials. The average E obtained for the photocrosslinked RGD protein film investigated was 0.53 ± 0.02 MPa.

2.2 Introduction

The Tirrell laboratory has developed a family of aECM proteins for use as biomaterials in a variety of biomedical applications including vascular graft engineering [1-5] and the development of artificial corneal onlays [6]. aECM proteins are composed of a repeating structural motif derived from elastin coupled to periodically spaced cell-binding domain sequences from fibronectin [7]. Elastin-like multimers of the amino acid sequence (VPGIG) were originally chosen to serve as the backbone of the aECM proteins in vascular graft engineering, as elastin is abundant in the walls of small muscular arteries [8, 9]. These short repeating sequences of elastin have also been shown to reproduce mechanical compliance in the appropriate range for many soft-tissue applications [5].

These proteins have been shown to form films with tunable mechanical properties that also promote cell attachment [4, 10]. In order to achieve a material with tunable mechanical properties, a crosslinking site was included within the construct to serve as a target for one of several chemical crosslinking reactions [10-12]. Variation in the degree of crosslinking allowed the preparation of films with desired mechanical properties. Tensile strength measurements to quantify the mechanical properties of these materials demonstrated elastic moduli that span the range characteristic of native elastins (0.3–0.6 MPa) [10].

To mediate selective endothelial cell adhesion, materials were designed to contain the CS5 cell-binding domain from the IIICS region of fibronectin, as the REDV portion of its sequence is recognized by the $\alpha_4\beta_1$ integrin on endothelial cells and has been shown not to induce binding of fibroblasts, vascular smooth muscle cells, or platelets [13, 14]. Protein constructs were also prepared containing the RGD sequence from the tenth type

III domain of fibronectin, which endothelial cells are known to bind through $\alpha_v\beta_3$ and $\alpha_5\beta_1$ integrins [15]. Corresponding HUVEC experiments performed on these films established that endothelial cell adhesion to constructed aECM proteins is specific to the presentation of appropriate cell binding domains [3, 4]. Moreover, it was demonstrated that the strength of adhesion to the artificial substrate was retained at shear stresses well above normal physiological values [4]. Further experiments using phase contrast and fluorescence microscopy confirmed that aECM proteins promote HUVEC spreading and proliferation to a confluent cell monolayer [2, 4].

Experiments performed using artificial proteins in the Tirrell laboratory, as well as other reports in the literature, have demonstrated that cells respond to physical and chemical signals as well as gradients of these signals [16-20]. Although there has been much progress in controlling cellular behavior by altering the spatial organization of either chemical or mechanical signals [18, 19], minimal advancement has been made in fabricating substrates that allow for the simultaneous modulation of surface chemistry and substrate mechanics. The ability to reproduce such conditions *in vitro* would provide a novel environment in which to examine the interplay of competing signals affecting cellular response on engineered materials.

To analyze how cells interact with biomaterials of varying properties *in vitro*, we have expanded the aECM protein family through the addition of photoreactive aECM proteins. These proteins contain an elastin-derived amino acid sequence (VPGVG)_x, and a fibronectin-derived cell-binding domain, RGD (Figure 2-1). A photocrosslinking site introduced into the (VPGVG)_x sequence dictates the mechanical properties of protein films, while the RGD binding domain mediates cell attachment. A scrambled negative

control protein was also generated by swapping the position of one amino acid in the cell-binding domain (RGD→RDG). Manipulation of the phenylalanyl-tRNA synthetase (PheRS) [21] of the bacterial expression strain permitted the incorporation of the non-canonical amino acid, *para*-azidophenylalanine (pN_3Phe), within the elastin subunit of the protein. Photochemical crosslinking at pN_3Phe sites provides control over the elastic modulus of the material that can be altered by adjusting the irradiation dosage at 365 nm or by varying the incorporation levels of pN_3Phe in the protein. The unique construction of the aECM proteins allows both the chemical (cell-binding domain density) and mechanical (elastic modulus) properties of the films to be controlled independently, thus enabling the investigation of their combined effects on cellular behavior.

RGD- N_3
MMASMTGGQQMGGHHHHHHDDDDK(LDASFLDYAVTGRRGDSPASSKPIAASA((VPGVG)₂VPGFG(VPGVG)₂)₅VP)₃)LE
T7 tag His tag RGD cell-binding domain elastin-like domain

RDG- N_3
MMASMTGGQQMGGHHHHHHDDDDK(LDASFLDYAVTGRRDGSPASSKPIAASA((VPGVG)₂VPGFG(VPGVG)₂)₅VP)₃)LE
T7 tag His tag scrambled RDG domain elastin-like domain

Figure 2-1. Photoreactive aECM protein sequences. Each protein contains a T7 tag, a heptahistidine tag, a cell-binding domain, and an elastin-like repeat.

2.3 Materials and Methods

2.3.1 Cloning of photoreactive aECM proteins

The genes encoding the aECM proteins were constructed using the cloning scheme shown in Figure 2-2 [22]. To obtain plasmids harboring these genes, a plasmid containing the desired elastin-like repeat and a different domain (SC5) was used to perform a cell-binding domain swap (pEC2-SC5-ELF₅, cloned by Dr. Marissa Mock) [23]. In order to increase the efficiency of the swap procedure, the SC5-ELF₅ insert was

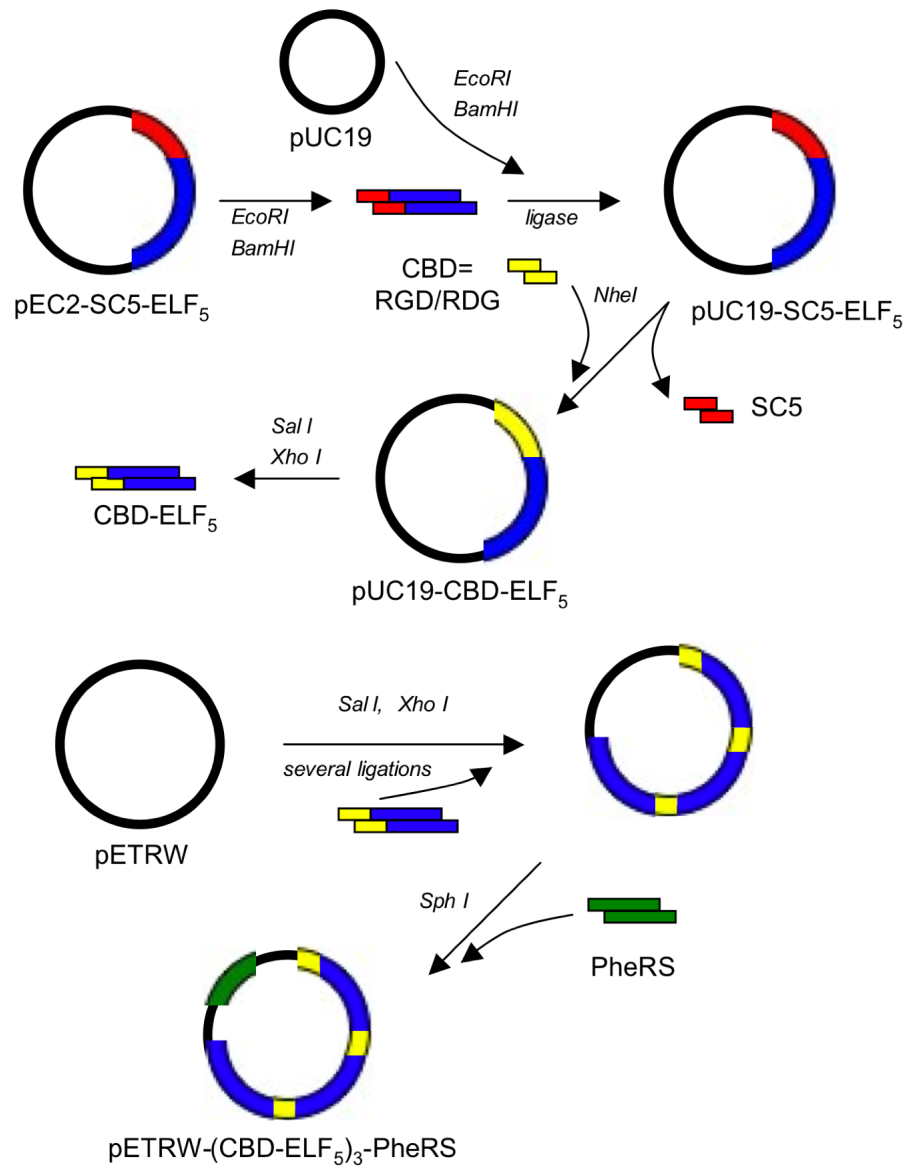


Figure 2-2. Schematic of the protocol for cloning aECM proteins.

first isolated by enzymatic digestion with *EcoRI* and *BamHI* (New England Biolabs, Ipswich, MA) and cloned into a high copy pUC19 plasmid to create pUC19-SC5-ELF₅. Next, synthetic oligonucleotides (Qiagen, Valencia, CA) encoding the RGD and RDG domains were annealed, phosphorylated, and ligated using T4 DNA ligase (Roche Applied Science, Indianapolis, IN) into a pEC2 plasmid to produce pEC2-RGD and pEC2-RDG (this step was omitted from the cloning figure). To remove the SC5 domain from the plasmid for the domain exchange, the SC5-containing plasmid was digested with *Nhe I* (New England Biolabs) and the digestion mixture was separated using gel electrophoresis (1% agarose). The digested plasmid was excised from the gel and the SC5 domain was discarded. To complete the domain exchange, pEC2-RGD and pEC2-RDG plasmids were digested with *Nhe I* to isolate the target domains. These domains were gel purified (1% agarose) and ligated into the *Nhe I* sites in the digested pUC19-SC5-ELF₅ plasmid to create pUC19-RGD-ELF₅ and pUC19-RDG-ELF₅. The ligation was allowed to proceed for 1.5 hours at 25°C, and the ligation mixture was subsequently transformed into *E. coli* XL1-Blue cells (Stratagene, Wilmington, DE). Transformed cells were plated on ampicillin (Sigma, St. Louis, MO) selection plates for overnight growth.

Transformants were grown in 2 x YT liquid cultures, miniprepmed (QIAprep Spin Miniprep Kit, Qiagen), and screened using a *Nhe I* test digestion to confirm the presence of the inserted domains. All samples were sent for sequencing (Laragen, Los Angeles, CA) using designed primers (Qiagen) to validate the orientation of inserted domains.

To obtain RGD-ELF₅ and RDG-ELF₅ cassettes for the next ligation step, pUC19-RGD-ELF₅ and pUC19-RDG-ELF₅ plasmids were digested with *Sal I* and *Xho I* (New England Biolabs) and the reaction mixtures were purified by gel electrophoresis (1%

agarose). The cohesive ends produced by *Sal I* and *Xho I* are sequence compatible, enabling the insertion of several gene cassettes into the plasmids. This procedure maintains a single *Xho I* site necessary for the insertion of additional DNA cassettes.

Using this method, RGD-ELF₅ and RDG-ELF₅ cassettes were ligated into an *Xho I*-digested pETRW expression vector (designed by Ralf Weberskirch). This expression vector contains a bacteriophage T7 promoter that allows for gene expression upon induction with isopropyl-1- β -D-thiogalactosidase (IPTG, Calbiochem, San Diego, CA), a heptahistidine tag, and an enterokinase cleavage site (amino acid sequence DDDDK in Figure 2-1). The ligation mixture was incubated at 16°C for 12 hours and transformed into *E. coli* XL1-Blue cells. Transformed cells were plated onto kanamycin (Sigma) selection plates for overnight growth. Transformants were grown in liquid cultures of 2 x YT and minipreped. A test digestion using restriction enzymes *BglII* (New England Biolabs) and *Xho I* was performed to confirm the presence of the inserted cassettes. Since the insertion of three cassettes is required for each construct, the ligation procedure was repeated several times to generate the plasmids, pETRW-(RGD-ELF₅)₃ and pETRW-(RDG-ELF₅)₃. The sequence of the inserted cassettes was confirmed by sequencing using designed primers (Qiagen).

To create the final plasmids, the gene encoding a mutant *E. coli* phenylalanyl-tRNA synthetase (Ala294Gly) was isolated from a vector kindly provided by Dr. Peter Kast [21]. This mutant phenylalanyl-tRNA synthetase (PheRS) allows the incorporation of *p*N₃Phe in place of phenylalanine when protein expression is induced in a phenylalanine auxotrophic expression host [24]. A cell stock containing this vector was minipreped and digested with *Sph I* (New England Biolabs) to isolate the PheRS gene.

The PheRS gene was gel purified (1% agarose) and ligated into *Sph I*-linearized pETRW-(RGD-ELF₅)₃ and pETRW-(RDG-ELF₅)₃ plasmids. The ligation mixture was incubated at 16°C for 12 hours and transformed into *E. coli* XL1-Blue cells. The cells were plated on kanamycin selection plates for overnight growth. Colonies were picked from the transformation plate and grown in 2 x YT media. The liquid cultures were miniprep and screened for gene insertion using a test digestion with *Sph I*. All samples were sent for sequencing using designed primers (Qiagen). This cloning procedure produced both pETRW-(RGD-ELF₅)₃-PheRS and pETRW-(RDG-ELF₅)₃-PheRS plasmids. These plasmids were then transformed into a phenylalanine auxotrophic derivative of *E. coli*, designated AF-IQ [25], for protein expression under chloramphenicol (Sigma) and kanamycin selection. When expressed in the presence of *p*N₃Phe, these DNA constructs produced proteins RGD-N₃ and RDG-N₃.

2.3.2 Protein expression and purification

Expression of RGD-N₃ and RDG-N₃ proteins was performed using a medium shift procedure to allow for the incorporation of *p*N₃Phe [12]. Briefly, overnight starter cultures were inoculated in 5 mL of 2 x YT media containing kanamycin and chloramphenicol. The turbid overnight cultures were then used to inoculate 1 L expression cultures of M9 minimal media (-phenylalanine) supplemented with 80 mg of phenylalanine and antibiotics. The cultures were grown at 37°C in a shaking incubator to an optical density (OD₆₀₀) > 1.0. Expression was induced with 1 mM IPTG for 10 minutes to allow for functional copies of PheRS to be synthesized before the cultures were centrifuged (10 min, 5000g, 4°C). The cell pellets were washed twice in 250 ml of

0.9% chilled NaCl by shaking, and resuspended in newly prepared M9 minimal media (without phenylalanine) to a volume of 1 L. The cultures were then supplemented with 80 mg of phenylalanine (positive control) or solid pN_3Phe (250 and 350 mg, Bachem, Bubendorf, Switzerland). The cultures were left to incubate, shaking at 37°C for 15 minutes before a second induction with 1 mM IPTG. After 4 hours of protein expression, the cells were harvested by centrifugation (10 min, 10,000g, 4°C). The pelleted cells were resuspended in 20 mL of TEN buffer (10 mM Tris-HCl, pH 8.0, 1 mM EDTA, 100 mM NaCl) and frozen at -80°C. The cell pellets were defrosted for 4 hours at 37°C with 10 µg/ml of deoxyribonuclease I, 10 µg/ml of ribonuclease A, and 50 µg/ml of phenylmethylsulfonyl fluoride. The target proteins were centrifuged at a temperature above the expected lower critical solution temperature (LCST, 60 min, 25,000g, 25°C) and then were extracted from the pellets into 4 M urea at 4°C [26]. The suspensions were clarified by centrifugation below the expected LCST (60 min, 25,000g, 2°C) and the supernatants were loaded into dialysis tubing (VWR, West Chester, PA, MWCO: 12–14,000 Da) and dialyzed against filtered deionized water at 4°C for 3 days. The dialysis products were centrifuged (60 min, 25,000g, 2°C) and the supernatants containing the target proteins were frozen and lyophilized.

2.3.3 *aECM protein characterization*

2.3.3.1 *Sodium dodecyl sulfate-polyacrylamide gel electrophoresis (SDS-PAGE)*

The expression and purification of photoreactive aECM proteins was monitored by gel electrophoresis using previously described protocols [4].

2.3.3.2 *Liquid chromatography-mass spectrometry*

Lyophilized samples of RGD-N₃ and RDG-N₃ proteins (less than 200 µg) were submitted for molecular weight analysis at the Protein/Peptide MicroAnalytical Laboratory in the Beckman Institute at Caltech.

2.3.3.3 *Amino acid analysis*

Purified protein samples (< 10 µg) along with a solid sample of *p*N₃Phe were sent for amino acid analysis at the Molecular Core Facility at the University of California, Davis.

2.3.3.4 *¹H NMR analysis*

¹H NMR analysis of purified RGD-N₃ and RDG-N₃ proteins was performed to determine the level of *p*N₃Phe incorporation. Samples were prepared at a concentration of 1 mM in DMSO-d₆ (Cambridge Isotope Laboratories, Andover, MA) and analyzed using a 600 MHz ¹H NMR (Varian) at Caltech.

2.3.4 *Preparation of photocrosslinked films for cell studies and mechanical testing*

2.3.4.1 *Irradiation setup*

Dry protein films were irradiated using unfiltered UV light (365 nm) from a high-pressure arc lamp (Oriel Q, 100 watts at 5 amps; measured intensity = 1.5 mW/mm²). The lamp was allowed to warm up for at least fifteen minutes before use.

2.3.4.2 *Substrate preparation for cell spreading experiments*

Substrates for cell spreading experiments were prepared following a protocol developed by former lab members, Drs. M.L. Mock and J.C. Liu [23, 27]. Circular glass coverslips (12 mm diameter, Corning, Corning, NY) were sonicated for 25 minutes in a saturated solution of potassium hydroxide in ethanol. Coverslips were rinsed individually with a stream of ethanol followed by a stream of distilled water and dried. Clean coverslips were spotted with 8 μ l of a 12.5 mg/ml solution of RGD-N₃ or RDG-N₃ and were spin-coated for 100 seconds at 1400 rpm on a Specialty Coating Systems model P-6000 spin coater. Protein-coated slides were dried at 50°C for 4 hours before a 60 second exposure to UV light to allow for sub-quantitative photocrosslinking. The protein films were then reacted with alkynyl-mPEG-SPA-5000 in a Cu(I)-catalyzed azide-alkyne [3+2] cycloaddition reaction in phosphate buffered saline (PBS) at pH 7.5 (200 μ M CuSO₄, 400 μ M tris(2-carboxyethyl)phosphine hydrochloride, 200 μ M tris-triazole ligand, 200 μ M alkynyl-mPEG-5000 [28]. Substrates were then rinsed for 1 hour in 1 mM EDTA, for 12 hours in 0.05% SDS, and for 2 hours in distilled water. The prepared substrates were adhered to the bottom of a well in a 6-well tissue culture plate by applying sterilized vacuum grease around the back edge of the coverslip. All wells had been previously blocked with a 0.2% solution of bovine serum albumin (BSA) in PBS. The covalent attachment of PEG molecules to the surface of protein films was performed to deter nonspecific cell attachment observed in preliminary experiments using these proteins.

The alkynyl-mPEG-5000 used in the [3+2] cycloaddition reaction was produced by dissolving 100 mg of mPEG-SPA-5000 (Nektar, Huntsville, AL) in an excess of propargylamine. The reaction mixture was left to stir overnight, and then was then poured

into 200 ml of ether. The precipitated product was collected by centrifugation and analyzed by ^1H NMR. The degree of PEGylation on protein surfaces was evaluated by X-ray photoelectron spectroscopy (XPS).

2.3.4.3 Substrate preparation for AFM measurements

RGD- N_3 substrates for AFM measurements were prepared by dissolving 10 mg of protein in 100 μl in water at 4°C . The solution was centrifuged (14,000g, 5 min) and the supernatant was added to the surface of base-cleaned (saturated potassium hydroxide in ethanol) 12 mm diameter glass coverslips. Samples were spin-coated for 30 seconds at 7000 rpm at 4°C , and left to dry at 4°C before exposure to UV light for 5 minutes. Uncrosslinked, soluble protein was removed by rinsing the substrate with water.

2.3.5 Cell maintenance

HUVEC (BioWhittaker, Walkersville, MD) were maintained in a 37°C , 5% CO_2 humidified incubator. The cells were grown in Endothelial Growth Medium-2 (EGM-2, 2% serum, BioWhittaker), which was replaced with new media every two days. Near confluent HUVEC cultures were passaged non-enzymatically by treatment with 0.61 mM EDTA (Gibco, Grand Island, NY). Only cell passages 2–10 were used for experiments; no differences between cell passages were noted.

2.3.6 Cell spreading experiments

Photocrosslinked substrates (RGD- N_3 and RDG- N_3 proteins) were adhered to the bottom of a 6-well tissue culture plate using vacuum grease as described above. For a

positive control, fibronectin (10 $\mu\text{g/ml}$ solution in PBS, Millipore, Billerica, MA) was adsorbed overnight in a 6-well plate at 4°C. For a negative control, heat-inactivated BSA (2 mg/ml solution in PBS) was adsorbed overnight in a 6-well plate at 4°C. All substrates were blocked with a 0.2% BSA solution for 30 minutes at room temperature and rinsed three times with PBS before cell seeding. HUVEC were resuspended in endothelial cell basal media (EBM-2, BioWhittaker) and added to each well at a density of 5.0×10^3 cell/cm² and placed in a humidified incubator (total volume = 3 ml). After 30 minutes, the plates were removed from the incubator and cells were imaged using a 10x phase contrast objective on a Nikon Eclipse TE 300 inverted microscope. Images were captured on a Sony CCD color video camera equipped with MetaMorph® imaging software (Molecular Devices, Sunnyvale, CA). The cells were manually traced using Image J provided by the National Institutes of Health to quantify the spread area. For each substrate, approximately 200 cells were traced in 4 independent experiments.

2.3.7 *AFM equipment*

Images and force curves of photocrosslinked protein films were obtained using a Park Scientific Instruments M5 atomic force microscope located in Aeronautical Engineering at Caltech. Samples were imaged using pyramidal-tipped triangular silicon nitride cantilevers (Veeco, Plainview, NY) with a listed spring constant of 0.58 N/m. To collect force curves from indented samples, a spherical tip with an attached SiO₂ particle (600 nm diameter, Novascan, Ames, IA) was used. The spring constant for this assembly was determined by calibrating it against two reference cantilevers and was calculated to be 0.25 N/m.

2.3.8 *AFM measurements: film thickness and force curves*

2.3.8.1 *Film thickness measurements*

Photocrosslinked RGD-N₃ films were scratched along the length of the coverslip with a pair of fine forceps to reveal the underlying glass substrate. The revealed surface was confirmed to be glass, based on its linear force profile when indented. The edge of this scratch was used as a reference point for imaging the film thickness. Scans of 30 μm x 30 μm were performed and the film thickness was recorded. The reported thickness was calculated by averaging measurements obtained at several locations ($n \geq 5$).

2.3.8.2 *Force curves*

Indentation measurements were obtained on a hydrated RGD-N₃ sample at room temperature according to a previously described protocol [12]. The glass microsphere-cantilever assembly was placed above the location where the sample thickness was measured (identified using a coupled optical microscope and visual markers) to associate indentation values with a known film thickness. The tip was then indented into the protein sample. The force and the z-displacement were recorded. Force curves were generated by plotting the loading force (nN) versus the z-displacement (nm). The indentation range was set relative to the contact point (-150 nm, +1350 nm), thereby limiting the deformation force to $\sim 20\text{--}30$ nN. The same spot was indented repeatedly, and the indentation-retraction cycles were 10 seconds in duration (tip speed = 3 $\mu\text{m}/\text{sec}$). Measurements were performed at several spots (> 1 mm apart) on the substrate.

2.4 Results and Discussion

2.4.1 Characterization of aECM proteins

2.4.1.1 SDS-PAGE

Protein expression and purification of newly constructed aECM proteins were tracked using SDS-PAGE (Figure 2-3). Aliquots of cultures representing equal numbers of cells (determined by the OD₆₀₀) were collected before and after induction (t = 0 and t = 4 hours) and resuspended in 4 M urea. These aliquots, along with samples of the collected pellets and supernatants from the LCST purification process, also prepared in 4 M urea, were loaded on a 12% polyacrylamide gel and size fractionated by electrophoresis (135 V, 75 min). The presence of the aECM proteins is apparent throughout the expression and purification; the purified target RGD-N₃ and RDG-N₃

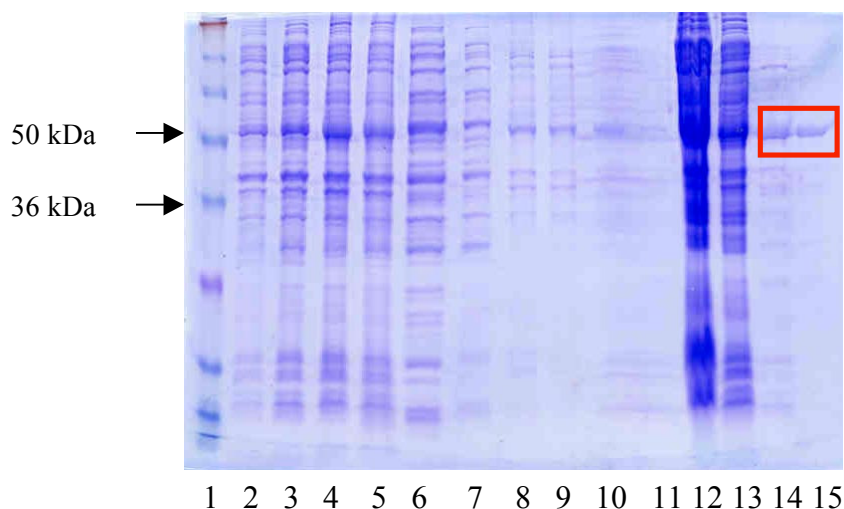


Figure 2-3. SDS-PAGE analysis of the purification of aECM proteins. Lane 1 of the gel contains the molecular weight marker; lanes 2 and 3 contain the pre-induction samples (t = 0 hr); lanes 4 and 5 contain the post-induction samples (t = 4 hr); lanes 6 and 7 contain the pellets of the first LCST cycle; lanes 8 and 9 contain the supernatants of the first LCST cycle; lanes 10 and 11 contain the supernatants of the second LCST cycle; lanes 12 and 13 contain the pellets of the second LCST cycle; and lanes 14 and 15 contain purified RGD-N₃ and RDG-N₃ proteins (red box), respectively.

proteins were detected near the calculated molecular weight of 42.99 kDa (red box).

Previous work indicates that aECM proteins run at higher apparent molecular weights than predicted [27]. For 1 L cultures grown to a final $OD_{600} = 1.20$, approximately 45 mg of each protein was recovered following purification.

2.4.1.2 Liquid chromatography-mass spectrometry (LC-MS)

LC-MS was performed to verify the molecular weight of the purified aECM proteins. The spectra of both RGD- N_3 and RDG- N_3 proteins showed a peak at $\sim 42,990$ amu, which indicates the presence of the purified proteins containing phenylalanine (Figure 2-4). The observed masses of the proteins are within 0.01% of the calculated mass. The broader peak observed in the spectra represents the distribution of proteins with varying levels of pN_3 Phe incorporation. The calculated molecular weight of proteins containing 100% incorporation of pN_3 Phe incorporation is ~ 43.73 kDa.

2.4.1.3 Amino acid analysis

Amino acid analysis was performed to determine the amino acid composition of the purified RGD- N_3 and RDG- N_3 proteins. The HPLC (high performance liquid chromatography) spectra of the hydrolyzed protein samples displayed peaks corresponding to amino acids present in the designed proteins (data not shown). The data was analyzed by dividing the amount of each recovered amino acid by the total recovered for all amino acids to generate a mole percent. These values were then compared to theoretical values calculated using the known amino acid sequence (Table 2-1). Only a small variation in the theoretical and observed values was detected for most amino acids

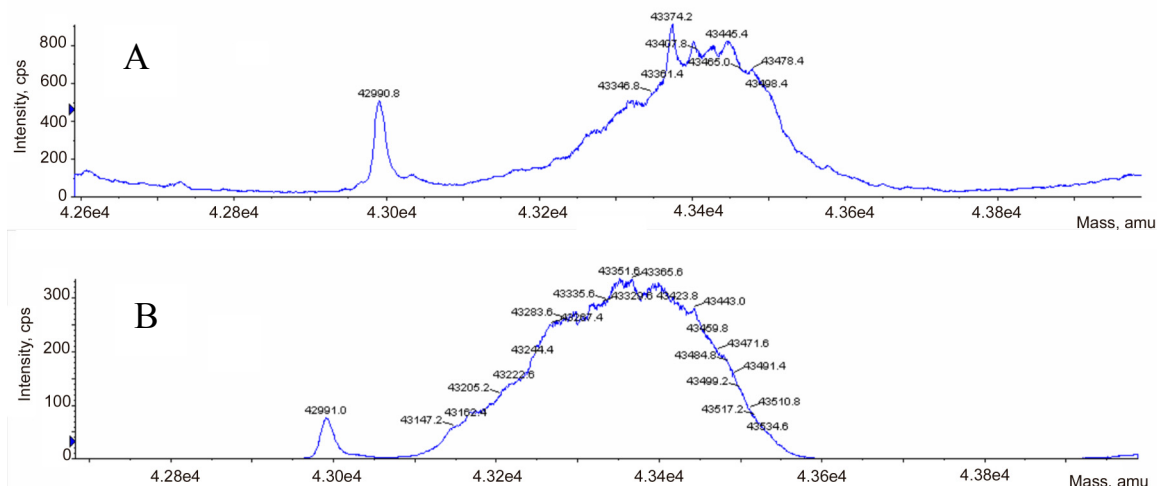


Figure 2-4. LC-MS spectra of purified (A) RGD-N₃ and (B) RDG-N₃ proteins. In each spectrum, the peak at 42.99 kDa represents protein containing 100% phenylalanine, and the broader peak represents proteins containing varying amounts of *p*N₃Phe.

(less than 1 mol%). The deviation in the theoretical and observed mol% for phenylalanine residues is the result of partial replacement of this residue by *p*N₃Phe.

2.4.1.4 ¹H NMR Analysis

The incorporation of *p*N₃Phe into proteins was determined by comparing the ¹H NMR spectra of proteins expressed in the presence of phenylalanine and *p*N₃Phe. The spectra of the two proteins are identical except for the presence of two additional doublets in the spectra of the proteins expressed in *p*N₃Phe (¹H NMR: δ 7.26 (d, *J* = 8.4 Hz, 2H), 6.98 (d, *J* = 7.8, 2H)). These peaks result from the aromatic protons of *p*N₃Phe, and the area under these peaks was integrated to give an incorporation percentage. The level of *p*N₃Phe incorporation into proteins was modulated by varying the concentration of *p*N₃Phe in the expression media. RGD-N₃ and RDG-N₃ cultures expressed in the presence of 250 mg/L and 350 mg/L of *p*N₃Phe yielded incorporation percentages of 15% and 51%, respectively.

Table 2-1. Theoretical and measured amino acid compositions of RGD-N₃ and RDG-N₃ proteins. The deviation in the theoretical and observed mol% for phenylalanine residues is the result of partial replacement of this residue by *p*N₃Phe.

Amino Acid	Theoretical mol%	aECM-RGD mol%	aECM-RDG mol%
Ala (A)	4	4.7	4.5
Arg (R)	0.7	0.4	0.8
Asn (N)	0	0	0
Asp (D)	2.8	3.4	3.1
Cys (C)	0	0	0
Glx (Q and E)	0.7	1.5	1.3
Gly (G)	32.6	32.3	32.2
His (H)	1.4	1.5	1.5
Ile (I)	0.7	1	1
Leu (L)	1.4	2	1.9
Lys (K)	0.9	1.2	1.1
Met (M)	0.9	1.1	0.8
Phe (F)	3.7	0.9	1.4
Pro (P)	17.2	16.7	16.8
Ser (S)	3.3	3.1	3.1
Thr (T)	0.9	1.1	1
Trp (W)	0	0	0
Tyr (Y)	0.6	0.4	0.8
Val (V)	28.3	28.8	28.8
Total	100.1	100.1	100.1

2.4.2 PEGylated and photocrosslinked aECM films for cell studies

To create samples appropriate for cell spreading studies, RGD-N₃ and RDG-N₃ protein films were first sub-quantitatively photocrosslinked with UV light before undergoing a Cu(I)-catalyzed azide-alkyne [3+2] cycloaddition reaction with alkynyl-mPEG. The alkynyl-mPEG was synthesized through the reaction of an activated ester form of the PEG molecule with propargylamine. The reaction occurred with 50% conversion, and the product was analyzed using ¹H NMR (data not shown). The degree of PEGylation was quantified using XPS by comparing the carbon/nitrogen ratio before and

after the PEGylation reaction. The XPS data indicated that an average of 1–2 PEG molecules per protein chain were successfully attached (data not shown).

2.4.3 Cell spreading results

To examine the sequence-specific nature of HUVEC spreading on the newly constructed aECM proteins, a series of cell spreading experiments was performed on uniformly photocrosslinked RGD-N₃ and RDG-N₃ proteins. HUVEC attained a greater measured cell area and exhibited well-spread morphologies on RGD-N₃ films as compared to the RDG-N₃ films. Cell areas achieved on the RGD-N₃ samples mimic those results obtained for the positive control of fibronectin, whereas the cell areas measured on the RDG-N₃ samples matched the areas measured on the negative control of BSA (Figure 2-5). The observation that HUVEC spread on RGD-N₃ films and not on RDG-N₃ films

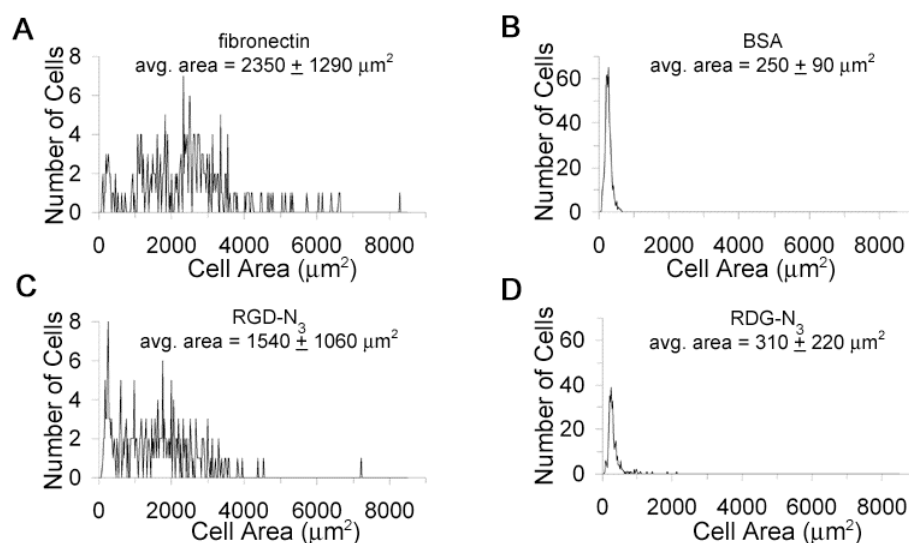


Figure 2-5. HUVEC spread areas on (A) fibronectin; positive control, (B) BSA; negative control, (C) RGD-N₃, and (D) RDG-N₃. The observation that HUVEC spread well on RGD-N₃ films and not on RDG-N₃ films indicates that cells recognize the RGD cell-binding domain specifically.

indicates that cells recognize the RGD cell-binding domain specifically. Moreover, the ability of HUVEC to recognize and spread on the RGD-N₃ protein suggests that photocrosslinking reactions that form the film do not render the RGD domain inactive.

2.4.4 AFM results: film thickness and elastic moduli measurements

2.4.4.1 Film thickness measurements

Thin films of photocrosslinked RGD-N₃ protein appeared smooth and uniform when imaged by AFM. An average film thickness of 205.5 ± 9.3 nm was obtained for dry samples (Figure 2-6), and a film thickness of 371 nm was acquired for a hydrated sample. Film thicknesses across the length of the sample did not deviate more than $\pm 10\%$ from the average. Films were made using a sample of RGD-N₃ protein with 51 % *p*N₃Phe incorporation.

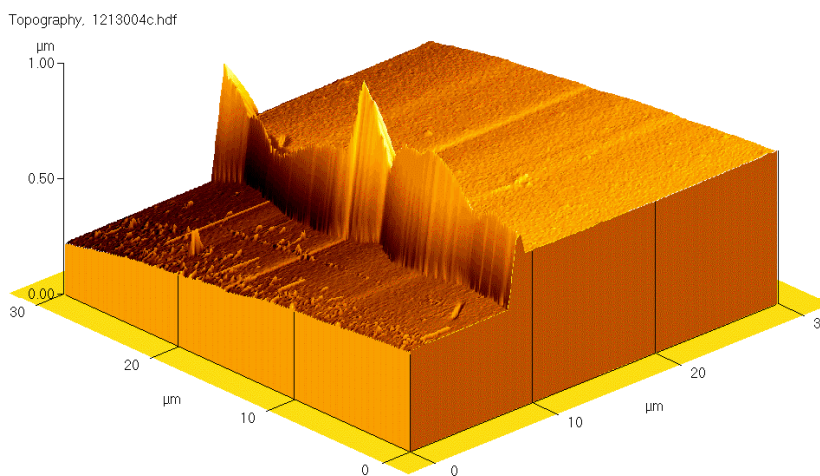


Figure 2-6. AFM topography scans of photocrosslinked RGD-N₃ protein. The film (right side of image) was scratched to reveal the underlying glass substrate (left side of image). The scales are not zeroed, but have been exaggerated in order to highlight the height difference between the glass substrate and the sample. The sharp spikes in the image are artifacts of the scratching procedure. The average height of this dry film was 205.5 ± 9.3 nm.

2.4.4.2 Elastic moduli measurements

A representative loading force curve obtained by nanoindentation of a photocrosslinked RGD-N₃ protein film (*p*N₃Phe content = 51%) is shown in Figure 2-7. The elastic modulus of the sample was extracted from the acquired data by using a model developed by Dimitriadis and coworkers [29]. This model describes the indentation profile of linear-elastic films of finite height using a spherical indenter, which corresponds to the experimental conditions in this study. The following equation summarizes the model assuming a Poisson ratio $\nu = 0.5$ (incompressible; a sensible assumption for biological and rubbery materials):

$$(1) \quad F = \frac{16E}{9} R^{1/2} \delta^{3/2} [1 + 1.133\chi + 1.283\chi^2 + 0.769\chi^3 + 0.0975\chi^4]$$

where F is the loading force, E is the elastic modulus, and δ is the indentation depth obtained using a rigid sphere of radius R . The first segment of the equation is derived from the classical Hertz contact model [30]. Additional terms have been added to the classical equation to form the Dimitriadis model which accounts for the finite height (h) of the sample, where χ is:

$$(2) \quad \chi = \sqrt{R\delta} / h$$

In this study, R corresponds to the radius of the glass bead attached to the cantilever, and the film height is the value measured during AFM topography scans.

In order to extract E , equation (1) was fitted to the obtained AFM indentation data according to a previously described protocol [12]. The indentation depth (δ) was calculated by subtracting the tip deflection from the total (z) displacement. The loading force (F) values used in the calculation were obtained by first identifying the contact point (Figure 2-7), the point where the indenter makes initial contact with the sample.

The contact point of the loading curve was assigned visually since the “snap-to-contact” point, or initial point, was easily identifiable. Force values beyond the contact point represent actual indentation data and were used in the calculation.

Using the data collected from the force curves, the elastic modulus was calculated at each data point. A single value of E was assigned to the sample by averaging the model-predicted moduli from 15 nm to 10% strain. The average E obtained for this RGD- N_3 sample was 0.53 ± 0.02 MPa, which lies in the range of values obtained using similar photocrosslinkable aECM proteins [12].

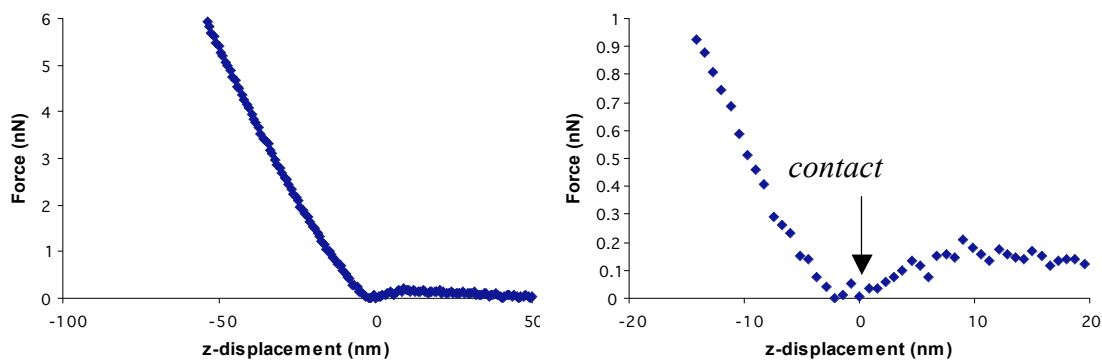


Figure 2-7. Representative loading indentation profiles for thin films of photocrosslinked RGD- N_3 protein. The loading force data is plotted against the z -displacement (indentation depth). The plot on the left shows the nature of the loading curve for an entire experiment, and the plot on the right is a magnified view to show the contact point assignment. These measurements were obtained on hydrated samples.

2.5 Conclusions

The construction and characterization of photoreactive aECM proteins has been successfully completed. SDS-PAGE, LC-MS, 1H NMR, and amino acid analysis confirmed the molecular weight and composition of the designed proteins. Varying the amount of pN_3 Phe added to the expression media altered the incorporation level of

*p*N₃Phe into proteins. HUVEC attachment to photocrosslinked films was found to be specific to the presence of the RGD cell-binding domain, and the elastic modulus of a hydrated protein thin film was acquired by nanoindentation. The average *E* obtained for the RGD-N₃ sample investigated was 0.53 ± 0.02 MPa.

References

1. Welsh, E.R., and D.A. Tirrell, *Engineering the extracellular matrix: A novel approach to polymeric biomaterials. I. Control of the physical properties of artificial protein matrices designed to support adhesion of vascular endothelial cells*. Biomacromolecules, 2000. **1**(1): 23-30.
2. Heilshorn, S.C., et al., *Endothelial cell adhesion to the fibronectin CS5 domain in artificial extracellular matrix proteins*. Biomaterials, 2003. **24**(23): 4245-4252.
3. Heilshorn, S.C., J.C. Liu, and D.A. Tirrell, *Cell-binding domain context affects cell behavior on engineered proteins*. Biomacromolecules, 2005. **6**(1): 318-323.
4. Liu, J.C., S.C. Heilshorn, and D.A. Tirrell, *Comparative cell response to artificial extracellular matrix proteins containing the RGD and CS5 cell-binding domains*. Biomacromolecules, 2004. **5**(2): 497-504.
5. Liu, J.C., and D.A. Tirrell, *Cell Response to RGD Density in Cross-Linked Artificial Extracellular Matrix Protein Films*. Biomacromolecules, 2008. **9**(11): 2984-2988.
6. Nowatzki, P.J., *Characterization of crosslinked artificial protein films*. PhD Thesis, 2006, California Institute of Technology.
7. Panitch, A., and D.A. Tirrell, *Artificial Extracellular Matrix Protein for Graft Design*, in *Tissue Engineering of Prosthetic Grafts* (P. Zilla, R.G. Greisler, eds.), 1999, Landes Company, p. 577-581.
8. Ross, M., et al., *Histology: A Text and Atlas*, 1995, Baltimore, MD: Williams & Wilkins.

9. Chandran, K.B., *Cardiovascular Biomechanics*, 1992, New York: University Press.
10. Nowatzki, P.J. and D.A. Tirrell, *Physical properties of artificial extracellular matrix protein films prepared by isocyanate crosslinking*. *Biomaterials*, 2004. **25**(7-8): 1261-1267.
11. Di Zio, K. and D.A. Tirrell, *Mechanical properties of artificial protein matrices engineered for control of cell and tissue behavior*. *Macromolecules*, 2003. **36**(5): 1553-1558.
12. Nowatzki, P.J., et al., *Mechanically tunable thin films of photosensitive artificial proteins: Preparation and characterization by nanoindentation*. *Macromolecules*, 2008. **41**(5): 1839-1845.
13. Humphries, M.J., et al., *Identification of an Alternatively Spliced Site in Human-Plasma Fibronectin That Mediates Cell Type-Specific Adhesion*. *Journal of Cell Biology*, 1986. **103**(6): 2637-2647.
14. Hubbell, J.A., et al., *Endothelial Cell-Selective Materials for Tissue Engineering in the Vascular Graft Via a New Receptor*. *Bio-Technology*, 1991. **9**(6): 568-572.
15. Pytela, R., M.D. Pierschbacher, and E. Ruoslahti, *A 125/115-kDa Cell-Surface Receptor Specific for Vitronectin Interacts with the Arginine-Glycine-Aspartic Acid Adhesion Sequence Derived from Fibronectin*. *Proceedings of the National Academy of Sciences of the United States of America*, 1985. **82**(17): 5766-5770.
16. Maskarinec, S.A., and D.A. Tirrell, *Protein engineering approaches to biomaterials design*. *Current Opinion in Biotechnology*, 2005. **16**(4): 422-426.

17. Lutolf, M.P., and J.A. Hubbell, *Synthetic biomaterials as instructive extracellular microenvironments for morphogenesis in tissue engineering*. Nature Biotechnology, 2005. **23**(1): 47-55.
18. Lo, C.M., et al., *Cell movement is guided by the rigidity of the substrate*. Biophysical Journal, 2000. **79**(1): 144-152.
19. Dertinger, S.K.W., et al., *Gradients of substrate-bound laminin orient axonal specification of neurons*. Proceedings of the National Academy of Sciences of the United States of America, 2002. **99**(20): 12542-12547.
20. Heilshorn, S.C., *Design and Characterization of Artificial Extracellular Matrix Proteins For Use As Small-Diameter Vascular Grafts*. PhD Thesis, 2004, California Institute of Technology.
21. Kast, P., *Pkss – a 2nd-Generation General-Purpose Cloning Vector for Efficient Positive Selection of Recombinant Clones*. Gene, 1994. **138**(1-2): 109-114.
22. Liu, C.Y., M.L.J. Apuzzo, and D.A. Tirrell, *Engineering of the extracellular matrix: Working toward neural stem cell programming and neurorestoration - Concept and progress report*. Neurosurgery, 2003. **52**(5): 1154-1165.
23. Mock, M.L., *Protein modification through in vivo incorporation of noncanonical amino acids*. PhD Thesis, 2005, California Institute of Technology.
24. Kirshenbaum, K., I.S. Carrico, and D.A. Tirrell, *Biosynthesis of proteins incorporating a versatile set of phenylalanine analogues*. Chembiochem, 2002. **3**(2-3): 235-237.

25. Yoshikawa, E., et al., *Genetically-Engineered Fluoropolymers - Synthesis of Repetitive Polypeptides Containing P-Fluorophenylalalanine Residues*. *Macromolecules*, 1994. **27**(19): 5471-5475.
26. Lee, J., C.W. Macosko, and D.W. Urry, *Phase transition and elasticity of protein-based hydrogels*. *Journal of Biomaterials Science-Polymer Edition*, 2001. **12**(2): 229-242.
27. Liu, J.C., *Endothelial cell response to artificial extracellular matrix proteins*. PhD Thesis, 2006, California Institute of Technology.
28. Beatty, K.E., et al., *Selective dye-labeling of newly synthesized proteins in bacterial cells*. *Journal of the American Chemical Society*, 2005. **127**(41): 14150-14151.
29. Dimitriadis, E.K., et al., *Determination of elastic moduli of thin layers of soft material using the atomic force microscope*. *Biophysical Journal*, 2002. **82**(5): 2798-2810.
30. Hertz, H., *Über die Berührung Fester Elastischer Körper (On the Contact of Elastic Solids)*. *Journal für die reine und angewandte Mathematik*, 1881. **92**: 156-171.

3 Lithographic Patterning of Photoreactive Cell-Adhesive Proteins

Reproduced with permission from:

Carrico, I.S., Maskarinec, S.A., Heilshorn, S.C., Mock, M.L., Liu, J.C., Nowatzki, P.J., Franck, C., Ravichandran, G., and D.A. Tirrell. *Lithographic Patterning of Photoreactive Cell-Adhesive Proteins*. Journal of the American Chemical Society, 2007. **129(16)**: 4874-4875.

Copyright 2007 American Chemical Society

3.1 Abstract

We describe a novel, simple method for the photolithographic patterning of cell-adhesive proteins. Intrinsically photoreactive proteins are synthesized in *Escherichia coli* through incorporation of the noncanonical, photosensitive amino acid *para*-azidophenylalanine. Upon ultraviolet irradiation at 365 nm, proteins form crosslinked films with elastic moduli that can be tuned by varying the concentration of photoreactive amino acid in the expression medium. Films of these proteins can be directly patterned using standard photolithographic techniques. We demonstrate the utility of this method of protein patterning by creating stable arrays of fibroblast cells on an engineered protein "photoresist".

3.2 Introduction

Control of the spatial arrangement of proteins on surfaces is essential in a number of emerging technologies, including protein microarrays, biosensors, tissue engineering, and regenerative medicine [1-4]. Patterning is also a powerful tool in cell biology, wherein cell arrays are used to elucidate the factors that mediate migration, proliferation, and cell-cell interactions [5-9]. Although photolithography holds a preeminent place as a patterning method in the microelectronics industry, optical lithography of proteins has been hampered by the need either to use traditional chemical photoresists or to modify proteins chemically by attachment of photoreactive functional groups; both methods can compromise protein function [10].

Production of a protein “photoresist” without the need for post-translational chemical modification would require an intrinsically photoreactive protein. Recently, the incorporation of photoreactive, noncanonical amino acids into proteins via site-specific and residue-specific techniques has been reported [11-15]. Here we describe the microbial expression of artificial proteins bearing the photosensitive noncanonical amino acid *para*-azidophenylalanine (pN_3Phe). The recombinant proteins, designated artificial extracellular matrix proteins with aryl azides (aECM- N_3), belong to a family of engineered proteins designed to exhibit mechanical properties similar to those of native elastins and to support adhesion of mammalian cells through cell-binding domains (CS5 or RGD) derived from fibronectin (Figure 3-1 (A)) [16-19]. These proteins can be crosslinked efficiently upon irradiation at 365 nm. The physical properties of the crosslinked films can be controlled by changing the pN_3Phe content, and thin films can be patterned on surfaces via photolithographic techniques. We demonstrate the utility of

CS5:	MMASMTGGQQM	MGHHHHHHH	MG(LDGEEIQIGHIP	<u>REDVDY</u> HLYPG((VPGVG) ₂ VPGFG(VPGVG) ₂) ₅ VP) ₃ LE
	T7 tag	His tag	CS5 cell-binding domain	elastin-like repeats
RGD:	MMASMTGGQQM	MGHHHHHHH	DDDDK(LDASFLDYAVTGR	<u>RGD</u> SPASSKPIAASA((VPGVG) ₂ VPGFG(VPGVG) ₂) ₅ VP) ₃ LE
	T7 tag	His tag	RGD cell-binding domain	elastin-like repeats
RDG:	MMASMTGGQQM	MGHHHHHHH	DDDDK(LDASFLDYAVTGR	<u>RDG</u> SPASSKPIAASA((VPGVG) ₂ VPGFG(VPGVG) ₂) ₅ VP) ₃ LE
	T7 tag	His tag	scrambled RGD cell-binding domain	elastin-like repeats

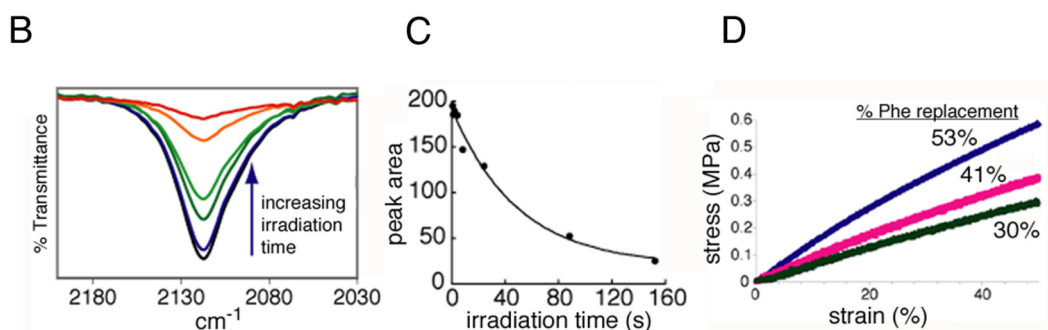


Figure 3-1. Characteristics of aECM-N₃ proteins. (A) Primary sequences of aECM-N₃ variants. (B) FTIR demonstrates loss of the characteristic azide asymmetric stretch as a function of irradiation time of CS5-N₃ films. (C) Peak area versus irradiation time yields a first-order decay with $t_{1/2} = 34$ sec. (D) Uniaxial tensile testing of irradiated mold-cast films.

3.3.1 Cloning of aECM-N₃ constructs

Synthetic oligonucleotides encoding the CS5 cell-binding domain were annealed, phosphorylated, and ligated into pEC2 to produce pEC2-CS5 [20]. An oligonucleotide encoding the elastin-like repeat (VPGVG)₂VPGFG(VPGVG)₂ was similarly ligated into pUC19 (New England Biolabs, Ipswich, MA) between the *Eco*RI and *Bam*HI sites. The insert was excised with *Ban*I and self-ligated to form multimers. The multimerization mixture was ligated into *Ban*I-linearized pEC2-CS5. Transformants with the pentamer

sequence were selected, digested with *Xho*I and *Sal*I, and ligated into a modified pET28a plasmid (Novagen, San Diego, CA). This step was repeated twice to obtain the final [CS5(ELF)₅]₃ construct under control of the T7 promoter. A similar cloning strategy was used for the RGD and RDG constructs. The *pheRS** gene encoding the alpha subunit of the A294G mutant of *E. coli* phenylalanyl-tRNA synthetase was subcloned into the *Sph*I site from the pKSS vector kindly provided by Dr. Peter Kast [21]. The final plasmids were designated pNS-CS5-ELF [22], pSM-RGD-ELF, and pSM-RDG-ELF.

3.3.2 Protein expression and purification

aECM-N₃ proteins were expressed in a phenylalanine auxotrophic *E. coli* strain, termed AF-IQ [23], harboring either pNS-CS5-ELF, pSM-RGD-ELF, or pSM-RDG-ELF. To express proteins from these strains, a culture was grown overnight in 2 x YT medium and used to inoculate 1L of M9AA medium supplemented with antibiotics kanamycin and chloramphenicol (Sigma). At an OD₆₀₀ of 1.0, expression of the target proteins and the T7 RNA polymerase was induced by adding 1 mM isopropyl-b-D-thiogalactoside (IPTG). After 10 minutes, the cells were washed twice with 0.9% NaCl and resuspended in M9 medium containing 19 amino acids (excluding phenylalanine) to a final volume of 1 L. The cultures were supplemented with either 25 mg/L phenylalanine (positive control) or up to 350 mg of *p*N₃Phe and grown for 4 hours. Protein expression was monitored by SDS-PAGE and Western blotting using an anti-T7 tag horseradish peroxidase conjugated antibody (Novagen). Cells were harvested after 4 hours by centrifugation (10,000g, 10 min, 25°C), and the cell pellets were resuspended in 20 mL of TEN buffer (10 mM Tris, 1 mM EDTA, 0.1 M NaCl) by sonication and

subsequently frozen. The frozen lysate was treated with 1 mM phenylmethylsulfonylfluoride and 10 $\mu\text{g/mL}$ of both DNase and RNase. The resulting mixture was agitated for 4 hours at 37°C and later centrifuged at a temperature above the expected lower critical solution temperature (LCST) of the protein (22000g, 60 min, 25°C). The target protein was extracted from the pellet into 4 M urea at 4°C. The resulting suspension was clarified by centrifugation (22000g, 60 min, 2°C), and the supernatant was dialyzed in cold (4°C) distilled water for 3 days, frozen, and lyophilized. Typical experiments yielded 40 mg of protein per liter of culture.

3.3.3 *Mechanical testing*

Samples were prepared in Teflon molds by drying 10% aECM-N₃ solutions in DMSO overnight at 50°C followed by irradiation with a 100 W mercury lamp for 30 minutes. Samples were removed from the molds, swollen in 4°C water overnight, cut into test strips, and finally equilibrated in PBS at 37°C. Films were approximately 3 mm x 10 mm. Tensile testing of equilibrated films was performed at 37°C in phosphate buffered saline at pH 7.4. Films were extended at a rate of 10% length/minute using an Instron-5542 (Instron Corporation, Canton, MA) with a 5N load cell. The data was acquired using the Instron Series IX Software for Windows (Merlin version).

3.3.4 *Photolithographic patterning of aECM-N₃ proteins*

Passivated glass slides were prepared by treatment with a silane. Standard glass microscope slides (Corning) were immersed in a solution of concentrated H₂SO₄ for 1 hour. After a thorough washing with water, slides were placed into a boiling solution of

NH₄OH/H₂O₂/H₂O (1:1:5) for 30 minutes. The slides were gently shaken in a 1% (v/v) solution of 2-[methoxy(polyethylenoxy)propyl] trimethoxysilane (Gelest) in toluene for 30 minutes. The slides were rinsed immediately with toluene, followed by a stream of methanol and water. The functionalized slides were then cured at 100°C for 30 minutes. Each PEO-modified slide was cut into 4 similarly sized pieces using a diamond cutter, and individual substrate pieces were covered dropwise with 10 µL of a 12.5 mg/mL solution of aECM-N₃ in DMSO that had been centrifuged for 1 minute at 14,000 rpm to remove particulates. Substrates were spun for 30 seconds at 1000 rpm on a Specialty Coating Systems model P-6000 spin coater. Protein-coated slides were dried at 50°C for 4 hours. Exposure of protein to sunlight was avoided until photolithography was complete. Protein-coated slides were irradiated for 60 seconds at 365nm using a Karl Suss mask aligner under a chrome-on-quartz mask prepared by Dr. Michael Diehl via chrome deposition and stripping from a 3000 dpi transparency. Irradiated substrates were washed for 4.5 hours in 6 M guanidine hydrochloride to remove soluble protein from the masked regions. Protein-patterned substrates were then rinsed for 5 minutes in filtered water and sterilized by an ethanol rinse before use.

3.3.5 *Cell culture*

Rat-1 fibroblasts (ATCC, Manassas, VA) were maintained in a 37°C, 5% CO₂ humidified environmental chamber. The cells were grown in Dulbecco's Modified Eagle Medium (DMEM, 10% fetal calf serum, Gibco), which was replaced every two days. Near-confluent Rat-1 cultures were passaged by treatment with trypsin (0.05% trypsin/EDTA) at 37°C for 2–5 minutes (Invitrogen) and resuspended in 2 mL of serum-

free DMEM. Cells were then centrifuged (1050 rpm, 3 min), and resuspended in fresh serum-free DMEM at a concentration of 1.0×10^6 cells/mL.

3.3.6 *Cell patterning*

Patterned substrates were placed in a 6-well plate, and Rat-1 fibroblasts (6.0×10^5 cells/substrate, $\sim 1.0 \times 10^5$ cells/cm²) were deposited on the patterned surfaces in a total of 3 mL of serum-free DMEM. After 4 hours of incubation, phase contrast images were captured with a Nikon Eclipse TE 300 microscope. Fluorescence images were acquired using a laser scanning confocal microscope consisting of a confocal system (Nikon C-1) combined with an inverted optical microscope (Nikon TE-2000-U). To fix and fluorescently label cell patterns, the substrates were washed three times with PBS before treatment with chilled acetone at -20°C for 5 minutes. The substrates were again rinsed with PBS and blocked with a 10% BSA solution for 30 minutes at room temperature. Afterwards, 1 μ L of a monoclonal anti-T7 tag primary antibody (Novagen) was added and allowed to incubate at room temperature for 1.5 hours. Individual substrates were then transferred to a standard Petri dish (VWR) containing a solution of 0.1% BSA and placed on a waver to wash for 10 minutes. A secondary antibody/phalloidin solution composed of 425 μ L PBS, 62.5 μ L secondary antibody (Cy2-labeled anti-mouse, 0.5 mg/mL, Chemicon), and 12.5 μ L rhodamine phalloidin (6.6 μ M, Invitrogen) was added per sample for 1 hour in the dark. Labeled samples were washed in 0.1% BSA for 10 minutes on a waver. The samples were then rinsed three times with PBS without agitation, and mounted with a glass coverslip using 25 μ L of Biomeda gel/mount

(Biomedica Corporation, Foster City, CA) solution. The samples were dried at room temperature for 1 hour and sealed with clear fingernail polish.

3.3.7 *Cell spreading*

Cell spreading experiments were performed on uniformly crosslinked films to determine whether the nature of cell attachment to protein-coated surfaces is sequence-specific to the RGD cell-binding domain. RGD-N₃ and RDG-N₃ substrates were prepared by spin coating 10 μ L of a 12.5 mg/mL protein solution at 1000 rpm for 30 seconds onto base-cleaned (saturated potassium hydroxide in ethanol) coverslips (12 mm diameter). Substrates were dried at 50°C overnight and uniformly irradiated for 60 seconds using an unfiltered Oriel 100W medium pressure mercury lamp. Substrates were rinsed with water for several minutes before being sterilized by an ethanol rinse.

For the positive control, 1 mL of a 10 μ g/mL fibronectin solution in PBS was adsorbed overnight in a 6-well plate at 4°C. The wells were rinsed three times with PBS, and blocked with a 2 mg/mL BSA solution for 30 minutes at room temperature and rinsed three times. For the negative control, 1 mL of a 2 mg/mL BSA solution in PBS was adsorbed overnight in a 6-well plate at 4°C. The wells were rinsed three times with PBS, and blocked with a 2 mg/mL BSA solution for 30 minutes at room temperature and rinsed three times. RGD-N₃ and RDG-N₃ substrates were adhered to the bottom of a BSA-blocked well by applying sterilized vacuum grease around the edge of the coverslips. Rat-1 cells were resuspended in serum-free media and seeded in a total volume of 3 mL per well at a density of 2.0×10^3 cells/cm². For quantification of spread area, pictures were obtained 4 hours post-seeding using a Nikon Eclipse TE 300

microscope. Cell areas were manually traced using ImageJ v. 1.33q (National Institutes of Health, Bethesda, MD). For each substrate, at least 200 cells in total were examined in at least 3 independent experiments.

3.3.8 Atomic force microscopy

Topographical scans of RGD-N₃ protein patterns were obtained with an AutoProbe M5 atomic force microscope (Park Scientific Instruments, Woodbury, NY) in a constant-force contact mode, using pyramidal tips (0.58 N/m, Veeco DNP-S). Imaging was performed dry or in water. When imaging in water, a glass slide was affixed to the back of the cantilever mount in the path of the laser, and the space between the sample and the slide was filled with water to provide a smooth and constant optical interface.

3.4 Results and Discussion

3.4.1 Expression and characterization of aECM-N₃ proteins

aECM-N₃ variants were expressed in *E. coli* cultures supplemented with *p*N₃Phe. Incorporation of *p*N₃Phe into the recombinant proteins relies on activation of the photosensitive amino acid by the phenylalanyl-tRNA synthetase (PheRS) of the bacterial expression host. The PheRS used for this study was a previously characterized mutant with relaxed substrate specificity [24]. This method results in statistical decoding of phenylalanine (Phe) codons placed at regular intervals in the coding sequence [24]. Proteins were expressed in a Phe auxotrophic *E. coli* strain and purified by exploiting the temperature-dependent phase behavior of proteins that contain elastin-like repeats [25]. Incorporation efficiency was determined by integration of the aromatic proton signals in

the ^1H NMR spectra of the purified proteins (Figure 3-2); the extent of Phe replacement varied from 13% to 53%, depending on the concentration of $p\text{N}_3\text{Phe}$ in the expression medium (Figure 3-3).

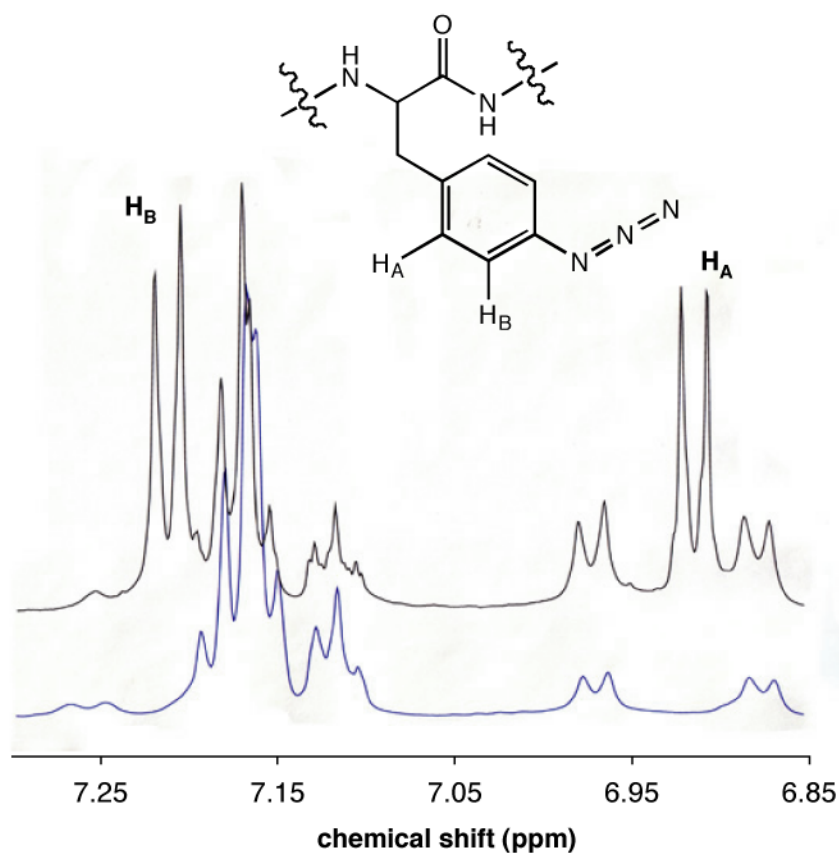


Figure 3-2. Representative ^1H NMR spectra (6.85–7.30 ppm region) of an aECM- N_3 construct expressed in media supplemented with phenylalanine (bottom spectrum) or with 250 mg/L $p\text{N}_3\text{Phe}$ (top spectrum). Spectra are identical except for two additional doublets in the top spectrum assigned to the aromatic protons of $p\text{N}_3\text{Phe}$; integration indicates replacement of 53% of the phenylalanine residues by $p\text{N}_3\text{Phe}$. 600 MHz spectra were taken on 1 mM samples in $\text{DMSO}-d_6$ at 23°C .

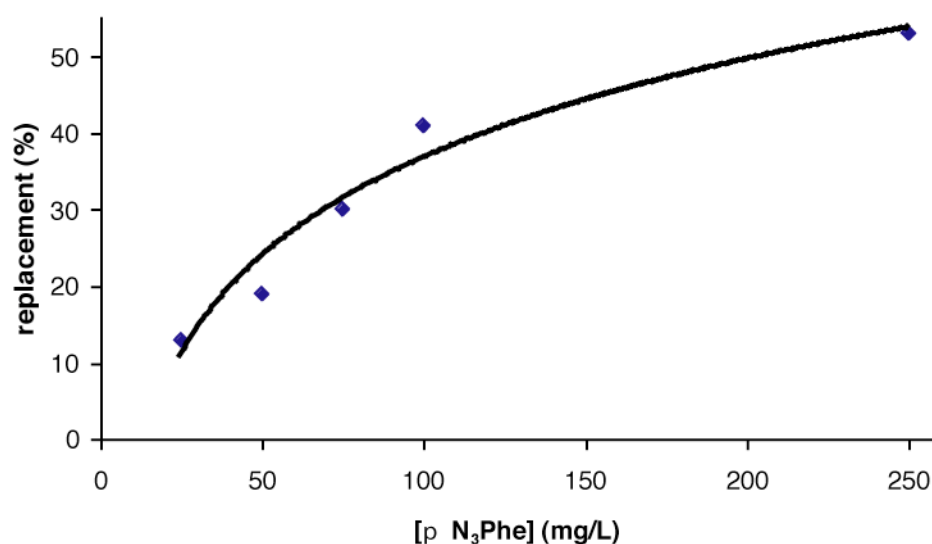


Figure 3-3. Incorporation of pN_3Phe into the CS5- N_3 protein as a function of concentration in the expression medium.

3.4.2 Kinetics of photodecomposition

Understanding the response of the photoreactive protein to irradiation is crucial for high-resolution pattern formation. We measured the rate of azide decomposition under irradiation by monitoring loss of the characteristic infrared asymmetric stretch at 2130 cm^{-1} (Figure 3-1 (B)) [26]. Measurements were performed on thin films of CS5- N_3 spin-coated directly onto zinc selenide wafers and irradiated using a Karl Suss contact aligner filtered to 365 nm in constant intensity (7 mW/cm^2) mode, with a quartz wafer in place of the mask. Azide loss under these conditions was rapid, following first-order kinetics with a half-life of 34 s (Figure 3-1 (C)). It is noteworthy that none of the other infrared bands were noticeably altered, indicating that irradiation under the conditions used here activates the aryl azide without substantial modification of the other canonical amino acids. Aryl azides have been used previously to effect photochemical crosslinking in protein and nucleic acid systems [27, 28].

3.4.3 *Mechanical testing*

Elastic moduli of irradiated CS5-N₃ films were determined by uniaxial tensile testing under simulated physiological conditions (Figure 3-1 (D)). As expected, the elastic modulus correlated with the extent of *p*N₃Phe incorporation. Irradiated CS5-N₃ films in which 30, 41, or 53% of the encoded Phe residues were replaced by *p*N₃Phe yielded elastic moduli of 0.53 ± 0.10 , 0.94 ± 0.09 , and 1.39 ± 0.09 MPa, respectively, values near the range characteristic of elastins (0.3–0.6 MPa) [16]. Replacement of less than 20% of the encoded Phe residues produced films too weak to test, and films made without *p*N₃Phe yielded no evidence of crosslinking. The capacity to vary the modulus by altering the *p*N₃Phe concentration in the expression medium is an attractive feature of this method, as recent work has highlighted the role of mechanical transduction mechanisms in mediating the physiology of adherent cells [29, 30].

3.4.4 *Cell patterning*

To investigate the potential of photoreactive proteins as substrates for studies of cell adhesion and growth, we created patterns of adherent fibroblasts on proteins patterned by photolithography. Protein films created by spin coating 12.5 mg/mL solutions of RGD-N₃ in dimethylsulfoxide directly on poly(ethylene oxide) (PEO)-coated glass slides were clear and homogeneous by optical microscopy. Protein films were irradiated for 60 s at 365 nm through a chrome-on-quartz mask. Stripping of the masked areas was accomplished by washing in 6 M guanidine hydrochloride.

Fluorescence immunolabeling with an anti-T7 tag antibody showed that the protein was localized only within the irradiated areas of the pattern. Films prepared from

protein lacking pN_3Phe formed no detectable patterns even after prolonged exposure. Non-contact atomic force microscopy (AFM) of RGD- N_3 patterns revealed uniform protein films. Films spun at 1000 rpm were 467 or 750 nm thick when imaged dry or hydrated, respectively. (Figure 3-4).

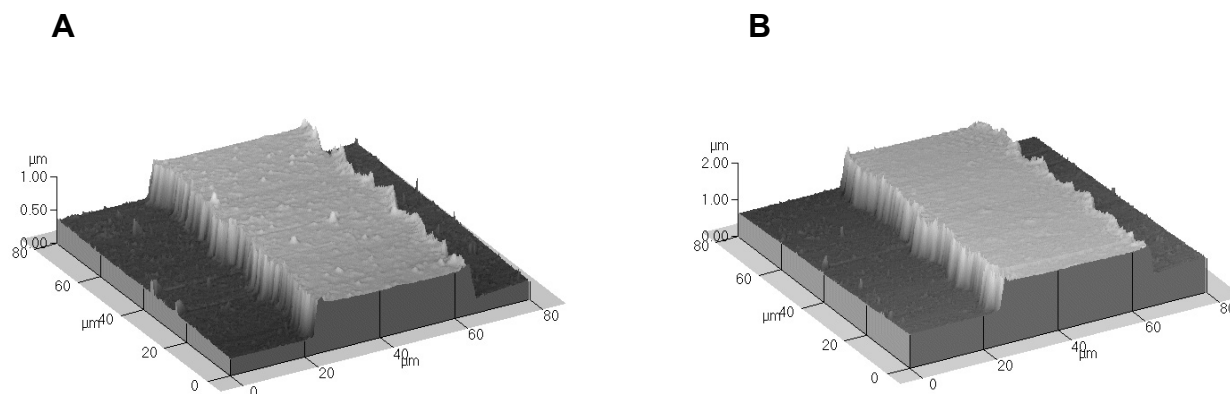


Figure 3-4. AFM images of patterned RGD- N_3 . The images were recorded on (A) dried or (B) hydrated patterned films in constant-force mode with an autoprobe M5 atomic force microscope (Park Scientific).

To create cell arrays, Rat-1 fibroblasts were deposited on RGD- N_3 patterns in the absence of serum. After 4 hr of incubation, the unattached cells were removed by mild washing with phosphate buffered saline (PBS) revealing cell patterns (Figure 3-5). Cell monolayers in the interior of the protein regions were indistinguishable from monolayers grown on fibronectin coatings; however, cells positioned along the RGD- N_3 pattern edges were elongated parallel to the pattern border, consistent with previous studies [31].

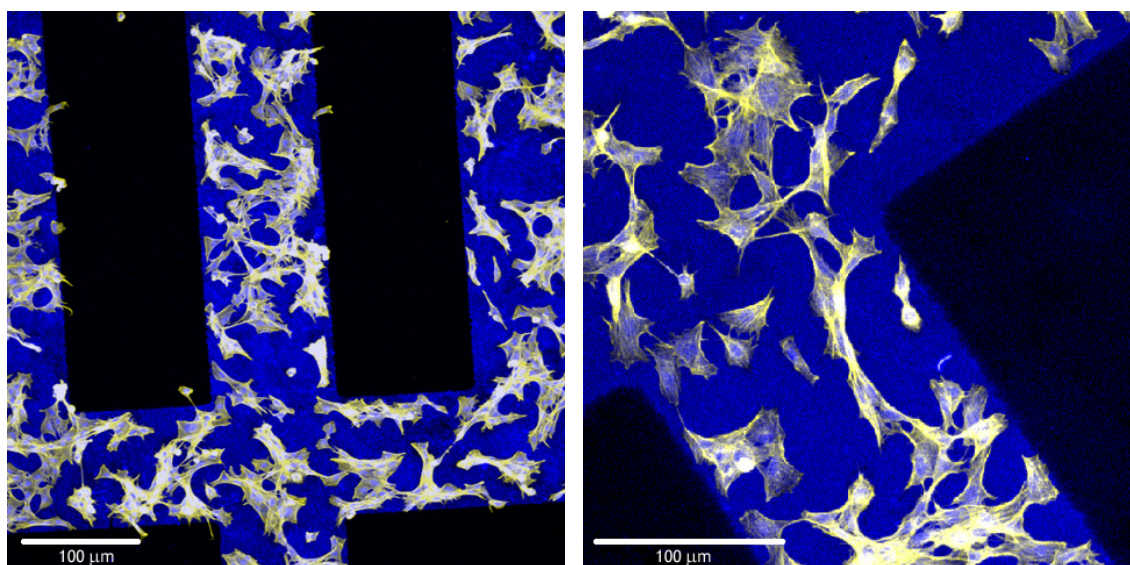


Figure 3-5. Confocal microscopy of Rat-1 fibroblasts attached to photopatterned RGD-N₃. Immunostaining with anti-T7 (blue) demonstrates colocalization of aECM-N₃ protein and cells (stained with rhodamine phalloidin (yellow)). Scale bars represent 100 μ m.

3.4.5 *Cell spreading*

To determine whether cells specifically recognize the RGD cell-binding domain, we compared cell spreading on uniformly photocrosslinked RGD-N₃ and RDG-N₃ (sequence-altered, negative control) films (Figure 3-6). After 4 hr of incubation, Rat-1 cells spread well on RGD-N₃ films, although the extent of spreading was reduced in comparison to that observed on the fibronectin control. In contrast, cells did not spread on RDG-N₃ and resembled cells plated on bovine serum albumin (BSA).

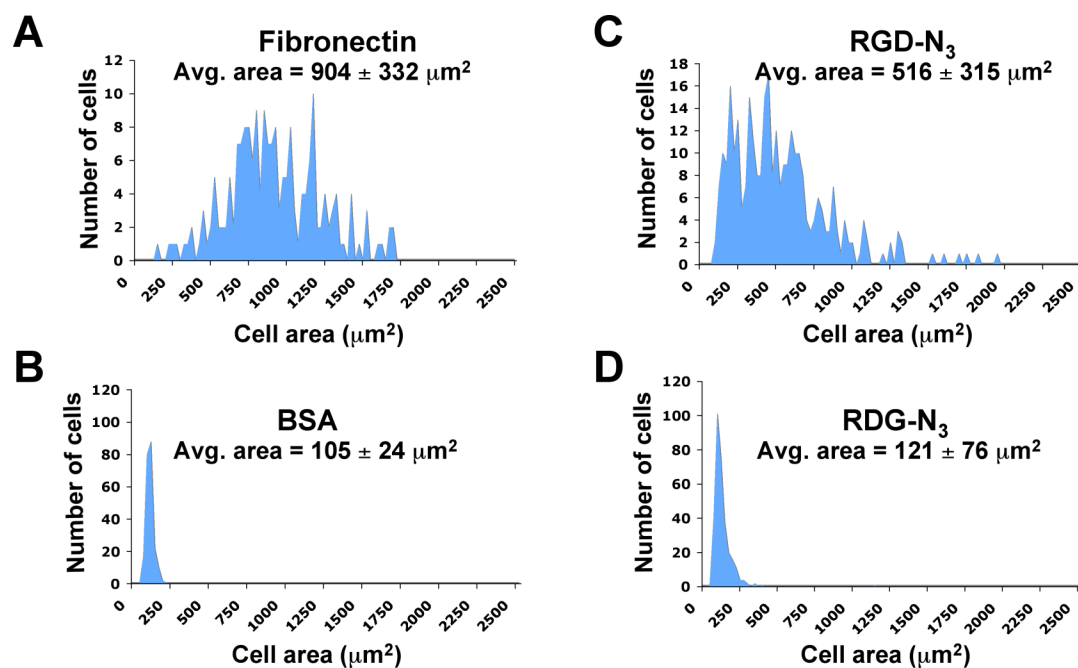


Figure 3-6. Rat-1 fibroblast cell spread areas on (A) fibronectin, (B) BSA, (C) RGD-N₃, and (D) RDG-N₃. RGD-N₃ supports sequence-specific cell spreading.

3.5 Conclusions

The availability of intrinsically photoreactive proteins enables new approaches to protein patterning. The technical simplicity of the method allows rapid production of samples with a wide variety of feature shapes and sizes, while permitting straightforward engineering of the elastic modulus of the crosslinked protein. The method is a promising approach to the study of adherent cells, providing control over mechanical properties, ligand-receptor interactions, and geometric shape. Applications in medical devices, tissue engineering, and array technologies are readily imagined.

3.6 Acknowledgements

We thank Michael Diehl, Alireza Ghaffari, and Nandita Sharma for helpful discussion, and Kechun Zhang for help in preparing the patterned substrates. Support was

provided by the NSF Center for the Science and Engineering of Materials at Caltech, NIH 62523 and EB 01971, an NIH predoctoral fellowship to SAM, a Whitaker Graduate Fellowship to JCL, and the Joseph J. Jacobs Institute for Molecular Engineering for Medicine.

3.7 References

1. Ekins, R.P., *Multi-Analyte Immunoassay*. Journal of Pharmaceutical and Biomedical Analysis, 1989. **7**(2): 155-168.
2. Tan, W., and T.A. Desai, *Layer-by-layer microfluidics for biomimetic three-dimensional structures*. Biomaterials, 2004. **25**(7-8): 1355-1364.
3. Templin, M.F., et al., *Protein microarray technology*. Trends in Biotechnology, 2002. **20**(4): 160-166.
4. Christman, K.L., V.D. Enriquez-Rios, and H.D. Maynard, *Nanopatterning proteins and peptides*. Soft Matter, 2006. **2**(11): 928-939.
5. Voldman, J., *BioMEMS – Building with cells*. Nature Materials, 2003. **2**(7): 433-434.
6. Shim, J., et al., *Micro- and nanotechnologies for studying cellular function*. Current Topics in Medicinal Chemistry, 2003. **3**(6): 687-703.
7. Corey, J.M., and E.L. Feldman, *Substrate patterning: an emerging technology for the study of neuronal behavior*. Experimental Neurology, 2003. **184**: S89-S96.
8. Rozkiewicz, D.I., et al., *Covalent microcontact printing of proteins for cell patterning*. Chemistry—a European Journal, 2006. **12**(24): 6290-6297.

9. Suh, K.Y., et al., *A simple soft lithographic route to fabrication of poly(ethylene glycol) microstructures for protein and cell patterning*. Biomaterials, 2004. **25**(3): 557-563.
10. Blawas, A.S. and W.M. Reichert, *Protein patterning*. Biomaterials, 1998. **19**(7-9): 595-609.
11. Kirshenbaum, K., I.S. Carrico, and D.A. Tirrell, *Biosynthesis of proteins incorporating a versatile set of phenylalanine analogues*. Chembiochem, 2002. **3**(2-3): 235-237.
12. Zhang, K.C., M.R. Diehl, and D.A. Tirrell, *Artificial polypeptide scaffold for protein immobilization*. Journal of the American Chemical Society, 2005. **127**(29): 10136-10137.
13. Chin, J.W., et al., *Addition of a photocrosslinking amino acid to the genetic code of Escherichia coli*. Proceedings of the National Academy of Sciences of the United States of America, 2002. **99**(17): 11020-11024.
14. Chin, J.W., et al., *Addition of p-azido-L-phenylalanine to the genetic code of Escherichia coli*. Journal of the American Chemical Society, 2002. **124**(31): 9026-9027.
15. Bose, M., et al., *The incorporation of a photoisomerizable amino acid into proteins in E-coli*. Journal of the American Chemical Society, 2006. **128**(2): 388-389.
16. Di Zio, K. and D.A. Tirrell, *Mechanical properties of artificial protein matrices engineered for control of cell and tissue behavior*. Macromolecules, 2003. **36**(5): 1553-1558.

17. Heilshorn, S.C., et al., *Endothelial cell adhesion to the fibronectin CS5 domain in artificial extracellular matrix proteins*. *Biomaterials*, 2003. **24**(23): 4245-4252.
18. Heilshorn, S.C., J.C. Liu, and D.A. Tirrell, *Cell-binding domain context affects cell behavior on engineered proteins*. *Biomacromolecules*, 2005. **6**(1): 318-323.
19. Liu, J.C., S.C. Heilshorn, and D.A. Tirrell, *Comparative cell response to artificial extracellular matrix proteins containing the RGD and CS5 cell-binding domains*. *Biomacromolecules*, 2004. **5**(2): 497-504.
20. Cantor, E.J., PhD Thesis, 1997, University of Massachusetts, Amherst.
21. Kast, P., *Pkss – a 2nd-Generation General-Purpose Cloning Vector for Efficient Positive Selection of Recombinant Clones*. *Gene*, 1994. **138**(1-2): 109-114.
22. Sharma, N., PhD Thesis, 2001, University of Massachusetts, Amherst.
23. Yoshikawa, E., et al., *Genetically-Engineered Fluoropolymers – Synthesis of Repetitive Polypeptides Containing P-Fluorophenylalanine Residues*. *Macromolecules*, 1994. **27**(19): 5471-5475.
24. Ibba, M., and D. Soll, *Aminoacyl-tRNA synthesis*. *Annual Review of Biochemistry*, 2000. **69**: 617-650.
25. Welsh, E.R., and D.A. Tirrell, *Engineering the extracellular matrix: A novel approach to polymeric biomaterials. I. Control of the physical properties of artificial protein matrices designed to support adhesion of vascular endothelial cells*. *Biomacromolecules*, 2000. **1**(1): 23-30.
26. Pretsch, E., P. Buhlmann, and C. Affolter. *Structure Determination of Organic Compounds: Tables of Spectral Data* (W. Fresenius, J.F.K. Huber, E. Pungor, G.

- A. Rechnitz, T. West, eds.), 2000, Verlag Berlin Heidelberg New York: Springer-Verlag.
27. Costas, C., et al., *RNA-protein crosslinking to AMP residues at internal positions in RNA with a new photocrosslinking ATP analog*. Nucleic Acids Research, 2000. **28**(9): 1849-1858.
 28. Cleary, M.A., P.S. Pendergrast, and W. Herr, *Structural flexibility in transcription complex formation revealed by protein-DNA photocrosslinking*. Proceedings of the National Academy of Sciences of the United States of America, 1997. **94**(16): 8450-8455.
 29. Engler, A., et al., *Substrate compliance versus ligand density in cell on gel responses*. Biophysical Journal, 2004. **86**(1): 617-628.
 30. Ingber, D.E., *Mechanosensation through integrins: Cells act locally but think globally*. Proceedings of the National Academy of Sciences of the United States of America, 2003. **100**(4): 1472-1474.
 31. Zhang, S.G., et al., *Biological surface engineering: a simple system for cell pattern formation*. Biomaterials, 1999. **20**(13): 1213-1220.

4 Towards Exploring the Proteomic Profile of Rat-1 Fibroblasts on Artificial Extracellular Matrix Proteins

4.1 Abstract

A first assessment of a biomaterial's biological performance most commonly involves the examination of macroscopic cellular behaviors such as spreading, adhesion, or migration *in vitro*. In this study, we have begun to expand this characterization of cellular response to include an investigation of the alterations in gene transcription and protein expression that occur during cell-biomaterial interaction. Rat-1 fibroblasts were deposited on biomaterials consisting of either adsorbed artificial extracellular matrix (aECM) proteins or fibronectin and allowed to spread for 2 hr. Cellular response was then analyzed in the following three ways: (1) by morphological analysis, through the measurement of cell spread area; (2) by transcriptomic analysis, through evaluation of gene expression levels using microarray technology; and (3) by proteomic analysis, through the utilization of the technique, BONCAT (bio-orthogonal noncanonical amino acid tagging), to detect newly synthesized proteins. Fibronectin and aECM proteins containing the biologically active RGD cell-binding domain were shown to promote cell spreading, and preliminary results indicate that cells deposited on fibronectin showed expression of genes and proteins associated with focal adhesion formation and cytoskeletal organization. Conversely, materials composed of aECM protein harboring a biologically inactive RDG domain did not promote cell spreading, and upregulation of mRNA transcripts encoding for factors involved in apoptosis and proteolysis were detected.

4.2 Introduction

New generations of synthetic biomaterials are required to be highly instructive and architecturally complex, interacting with cells and tissues through both chemical and mechanical cues to promote behaviors that aid healing and regeneration [1, 2]. However, despite the vast number of sophisticated biomaterials constructed in the last several years, characterization of cell-biomaterial interaction has remained largely superficial, evaluating phenotypic responses such as the extent of adhesion or migration [3, 4]. Although these measurements provide valuable information regarding cell behavior on materials, a cell interacting with a biomaterial has been shown to exhibit changes in its transcriptomic and proteomic profile [4-7]. Therefore, a more complete description of cell-biomaterial interaction must incorporate both macroscopic and molecular analyses.

Several studies have begun to investigate cell-biomaterial interactions at the molecular level by analyzing changes in intracellular processes such as gene transcription and protein expression. Klapperich and Bertozzi compared the gene expression profile of human fibroblasts (HF) deposited on tissue culture polystyrene to that of HF deposited on three-dimensional collagen-glycosaminoglycan meshes (CGM) and found that over 1000 genes were differentially expressed [7]. HF grown in CGM demonstrated upregulated transcripts for pro-angiogenic factors, chemokines/cytokines, adhesion molecules, and extracellular matrix remodeling genes. As indicated by the authors, upregulation of transcripts related to hypoxia and angiogenesis indicates that careful attention must be given to the pore size of designed materials in order to maintain physiological oxygen levels for cells. Xu and coworkers detected differential expression in 21 proteins when osteoblasts were deposited on bioceramic materials composed of hydroxyapatite (HA)

and hydroxyapatite reinforced with carbon nanotubes (HA-CNT) [6]. Interestingly, even though they noted distinct cellular morphologies of spread cells on HA compared to HA-CNT, they detected similar trends in the ratios of expressed proteins related to cell adhesion (with the exception of vimentin) when compared to a control surface of polystyrene.

Many groups have used both transcriptomic and proteomic techniques to investigate how the surface chemistry of polymeric materials induces an inflammatory response, which ultimately dictates the biocompatibility of implanted materials [8, 9]. These reports have demonstrated notable variability in the production of chemokines, cytokines, and matrix proteins produced by macrophages in response to different polymeric materials. The degree of macrophage activation in response to materials was also found to vary when cells were co-cultured with an increasing density of lymphocytes, indicating that there exists a complex interaction between macrophages and lymphocytes at the biomaterial interface that may need to be addressed in order to improve a material's suitability for clinical use [9]. In another approach, proteomic techniques have been employed to investigate the composition of adsorbed serum proteins on titanium, a metal commonly utilized to generate devices for hip and knee replacements [10, 11].

To foster the development of biomaterials that elicit desired cellular responses, an extensive study of cell-biomaterial interactions must be performed both at the macroscopic and the molecular level. Phenotypic measurements such as the extent of cell spreading and adhesion provide the first indication of a material's biological performance, and combined with further studies evaluating changes in gene and protein

expression, enable a global analysis of cellular response to biomaterials to be attained. This approach allows phenotypic behaviors to be correlated with the expression of multiple proteins and interrogates the extent to which mRNA transcript levels predict protein translation. Moreover, this approach expands the repertoire of *in vitro* testing methods for evaluating material scaffolds for medical applications, and information from these studies can be applied in the design of future materials.

A combined approach that encompasses phenotypic measurements, mRNA microarray analysis, and proteomics has been initiated in this study to further characterize cellular response to aECM proteins. These previously described proteins contain three repeating monomers that each consists of a cell-binding domain derived from fibronectin adjacent to an elastin-like polypeptide (Figure 4-1) [12]. A negative control protein was generated by swapping the position of one amino acid within the cell-binding domain. A phenylalanine residue included in the elastin backbone allows for the replacement of this residue with the photosensitive noncanonical amino acid, *para*-azidophenylalanine (pN_3Phe), when expressed in a bacterial host containing a mutant phenylalanyl-tRNA synthetase with relaxed substrate specificity [12]. Incorporation of pN_3Phe renders proteins intrinsically photoreactive, enabling the degree of crosslinking within protein films to be adjusted by varying the extent of pN_3Phe incorporation or altering the irradiation dosage at 365 nm [13]. The ability to independently modulate the biochemical (cell binding domain type and density) and mechanical (extent of crosslinking) properties of these materials offers a novel method in which to explore the effects of multiple factors on cellular response.

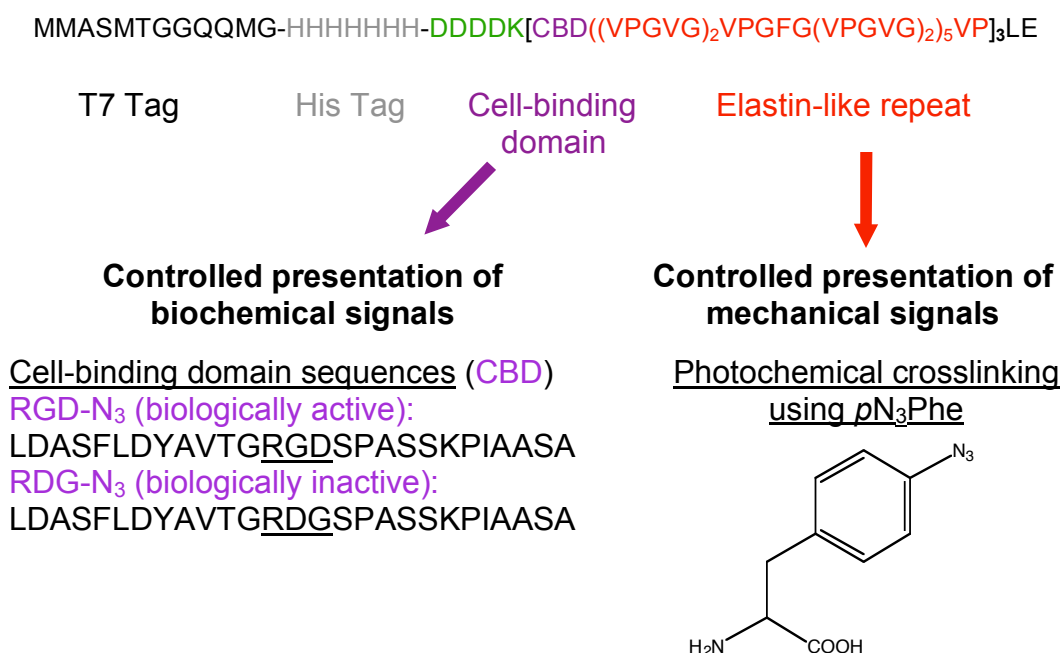


Figure 4-1. aECM protein sequences. Each protein contains a T7 tag, a heptahistidine (His) tag, a cell-binding domain (CBD, purple), and an elastin-like repeat (red). Controlled presentation of biochemical cues can be achieved by mixing the biologically active protein containing the RGD binding domain with the biologically inactive RDG domain. Controlled presentation of mechanical signals is accomplished through the incorporation of *p*N₃Phe into the elastin subunit, which permits photochemical crosslinking of proteins into films with varying mechanical properties.

In this study, phenotypic measurements were obtained by quantifying cell area after 2 hr of spreading on each artificial protein (RGD-N₃ and RDG-N₃) as well as surfaces composed of adsorbed fibronectin (FN) and bovine serum albumin (BSA). Affymetrix Genechips were used to examine gene expression from cells deposited on aECM proteins (RGD-N₃, RDG-N₃) compared to FN, and the proteomic technique BONCAT was employed to identify newly synthesized proteins produced during spreading on aECM proteins compared to FN (Figure 4-2) [14, 15]. BONCAT permits the enrichment of newly synthesized proteins through the incorporation of a methionine (Met) surrogate, azidohomoalanine (Aha, Figure 4-3), into proteins during a pulse.

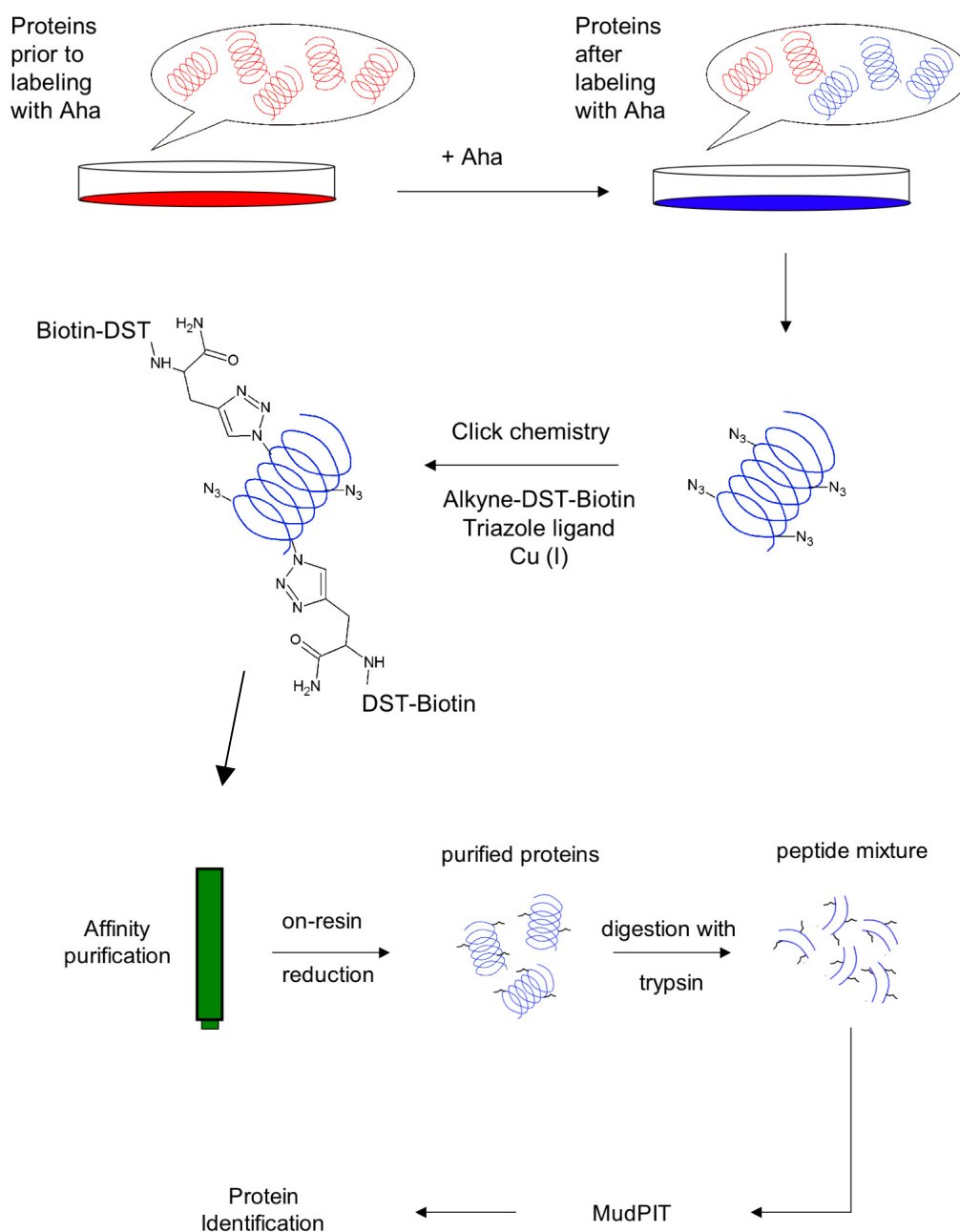


Figure 4-2. Schematic of BONCAT methodology [14]. Prior to labeling with Aha, cells express proteins containing all twenty canonical amino acids (red). After labeling with Aha, all newly synthesized proteins contain Aha (blue), making them distinguishable from preexisting proteins. Cells are lysed and the proteins are coupled to an alkyne disulfide biotin tag (alkyne-DST-Biotin) using click chemistry. Labeled proteins are enriched through affinity chromatography. Proteins are removed from the affinity resin by the addition of β -mercaptoethanol. Reduced proteins are digested with trypsin, and the resulting peptides are analyzed by multi-dimensional protein identification technology (MudPIT) [16]. The observed spectra are then correlated to protein sequences using search engines.

Nascent proteins made during the pulse will contain Aha, making these proteins chemically distinct from preexisting proteins. These proteins are then chemoselectively labeled with an affinity tag using [3+2] copper-catalyzed cycloaddition (“click chemistry”) and resin purified [15]. More specifically, the affinity tag and purification protocol used in this study were recently developed by Jennifer Hodas [19]. Identification of the purified proteins is achieved using multidimensional protein identification technology (MudPIT) and database searching [15, 16]. The combination of these three characterization methods provides a more integrated analysis of cell-aECM protein interaction during early time points of cell spreading.

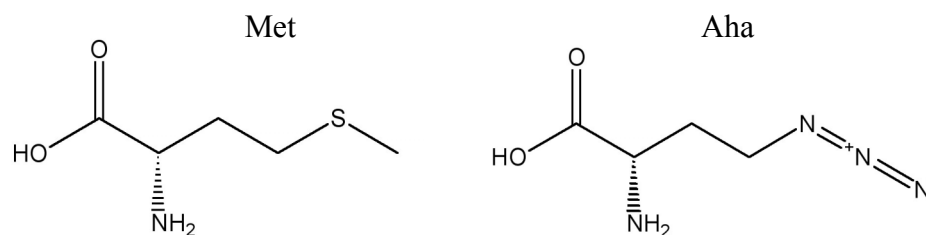


Figure 4-3. Chemical structures of methionine (Met) and azidohomoalanine (Aha).

4.3 Materials and Methods

4.3.1 Cell culture

Rat-1 fibroblasts (ATCC, Manassas, VA) were maintained in a 37°C, 5% CO₂ humidified incubator. The cells were grown in Dulbecco’s Modified Eagle Media (DMEM, Invitrogen, Carlsbad, CA) supplemented with 10% fetal bovine serum (Invitrogen) and penicillin/streptomycin (Invitrogen). The media was replaced every 2 d and cells were passaged enzymatically by treatment with 0.05% trypsin with EDTA (Invitrogen).

4.3.2 *Cell synchronization through contact inhibition*

In order to synchronize cells in G0/G1, cells were maintained at confluence for 2 d in DMEM. The extent of cell synchronization, as determined by DNA content, was examined using fluorescence-activated cell sorting (FACS) according to an established protocol [17]. Following incubation at confluence for 2 d, cells were detached using trypsin and transferred to a 15 mL conical tube for centrifugation (1200 rpm, 5 min, 25°C). The supernatant was discarded and 1 mL of chilled 70% ethanol was added dropwise while gently vortexing the cell pellet. Once the cell pellet was fully resuspended, the cell suspension was placed at 4°C for 30 min. The cells were collected by centrifugation (2000 rpm, 5 min, 25°C) and the supernatant was discarded. The cells were resuspended in 1 mL of phosphate buffered saline (PBS) and centrifuged (2000 rpm, 5 min, 25°C). This process was repeated twice. The cells were resuspended in 1 mL of PBS containing 100 µL of 100 µg/mL ribonuclease and left to incubate overnight at room temperature. Following incubation, 400 µL of propidium iodide (50 µg/mL in PBS, Invitrogen) was added to the cell suspension for 15 min. The cell suspension was then passed through a 40 µm filter into a polystyrene round-bottom tube (12 x 75 mm) and analyzed by FACS.

4.3.3 *aECM protein expression and purification*

RGD-N₃ and RDG-N₃ proteins were purified as outlined in Chapter 2.

4.3.4 *Cell spreading experiments*

Cell spreading experiments were performed on adsorbed protein films. Solutions of RGD-N₃ and RDG-N₃ proteins were prepared by dissolving 1 mg of each protein in 1 mL of distilled water. In order to increase protein dissolution, solutions were placed at 4°C overnight. The protein solutions were then sterile filtered (0.2 µm) and transferred to different wells within a 6-well plate and left to adsorb overnight at 4°C. Wells were also prepared containing 1 mL of a 10 µg/mL solution of FN and 1 mL of a 2 mg/mL solution of BSA and incubated overnight at 4°C. Three wells containing each protein solution were prepared per experiment. All wells were rinsed twice with PBS, blocked with 2 mg/mL of BSA for 30 minutes at room temperature, and rinsed three times with PBS. Serum-free DMEM lacking methionine (SFM –Met) was prepared according to a previously described protocol [18] and added to the wells. The medium was then supplemented with either Met or Aha (a gift from Dr. Janek Szychowski) to a final concentration of 2 mM.

Synchronized Rat-1 fibroblasts were incubated for 30 min in SFM –Met to deplete intracellular methionine stores. Following detachment with trypsin, cells were treated with 1 mL of SFM –Met containing 2.3 mg/mL soybean trypsin inhibitor (Sigma, St. Louis, MO). The cells were pelleted via centrifugation and resuspended in 3 mL of SFM –Met. Cells were added at a density of 1.6×10^5 cells/well.

For quantification of spread area, images were obtained 2 hr post-seeding using a Nikon Eclipse TE 300 microscope coupled to a Sony CCD color video camera. Images were captured using MetaMorph® imaging software (Molecular Devices, Sunnyvale, CA), and cell areas were manually traced using ImageJ version 1.37v (National Institutes

of Health, Bethesda, MD). For each substrate, at least 200 cells were examined in 3 independent experiments.

4.3.5 *Microarray analysis*

For mRNA microarray analysis, cell spreading was performed using 100 mm diameter Petri dishes coated using identical protein concentrations and blocking procedures as described above. In order to compensate for the increased surface area of the dish, 5 mL of each protein solution was used and the cell density was increased to $\sim 1.2 \times 10^6$ cells/plate. Synchronized cells were passaged as described above, and cell spreading was conducted in the presence of 2 mM Aha in SFM –Met. Following cell spreading experiments, each plate was rinsed twice with PBS. Isolation of mRNA was performed using the RNeasy Mini kit from Qiagen (Valencia, CA). The protocol outlined in the provided manual for the purification of RNA from animal cells using spin technology was applied. mRNA concentration was determined by measuring the absorbance at 260 nm (A_{260}) in a spectrophotometer. An absorbance measurement was also obtained at 280 nm (A_{280}) to assess sample purity, as the ratio of the reading at 260 nm and 280 nm provides an estimate of the purity of mRNA with respect to other contaminants (e.g., proteins) that absorb in the UV spectrum. Samples with an A_{260}/A_{280} ratio between 1.8–2.1 were considered “clean” [7]. Only purified samples with an A_{260}/A_{280} ratio ≥ 2 were submitted for microarray analysis to the Millard and Muriel Jacobs Genetics and Genomics Laboratory at Caltech. Affymetrix GeneChip Rat Genome 230 2.0 arrays (Rat230_2, Affymetrix, Inc., Santa Clara, CA) were used in all experiments. Each GeneChip Rat Genome 230 2.0 array contains 31,042 probe sets, and

each probe set contains eleven pairs of oligonucleotide probes to measure the transcription level of each sequence presented on the array. The data (rat genes and expressed sequence tags) was analyzed using the Rat Genome Database (RGD, <http://rgd.mcw.edu/>), Rosetta Resolver® version 7.2 (Rosetta Inpharmatics, Inc., Seattle, WA), and Microsoft Excel. The ratio-builder function in Resolver® was used to perform ratio experiments, and transcripts with intensity ratios (either $\text{intensity}^{\text{RGD/RDG}}/\text{intensity}^{\text{FN}}$ or $\text{intensity}^{\text{RGD}}/\text{intensity}^{\text{RDG}}$) having a P value ≤ 0.01 with a ≥ 2.0 -fold change were considered differentially expressed.

4.3.6 *Cell lysis and protein extraction for proteomic analysis*

Preliminary proteomic analysis was performed using FN-coated plates only. Cell spreading was performed using 100 mm diameter Petri dishes coated with FN and blocked with BSA as described above. SFM –Met was added to the plates and supplemented with either 2 mM Met or Aha. Synchronized cells were passaged as described above and deposited at a density of $\sim 1.2 \times 10^6$ cells/plate. Following cell spreading experiments, each plate was rinsed twice with PBS. The cells were lysed directly on the plate according to a communicated protocol [19] by the addition of 250 μL of 1% (w/v) SDS in PBS-PI (PBS, pH = 7.6, supplemented with EDTA-free complete protease inhibitor cocktail (PI), Roche Applied Science, Indianapolis, IN). The cell lysates were treated with 1 μL of benzonase (> 500 U, Sigma), transferred to a microcentrifuge tube, and vortexed for 30–60 seconds. In order to achieve complete cell lysis and protein denaturation, the samples were sonicated in a bath sonicator for 10 min and boiled at 96–100°C for 10 min. The samples were cooled to room temperature and

adjusted to 0.1% SDS by the addition of 2.25 mL of PBS-PI. Moreover, 20 μ L of 20% Triton X-100 was added to each sample. The samples were then centrifuged (2000g, 5 min, 4°C) and the supernatants were transferred to new tubes.

Cell lysates were labeled with an alkyne-disulfide-biotin tag (DST) using click chemistry [19]. Following a protocol described by Jennifer Hodas [19], each sample (5 mL) was incubated with the following reagents at 4°C overnight with constant agitation: 5 μ L of 200 mM triazole ligand in dimethyl sulfoxide, 2.5 μ L of 50 mM DST, and 50 μ L of 10 mg/mL CuBr. The reacted lysates were centrifuged (2000g, 5 min, 4°C) and the supernatants were transferred to new tubes. Excess unreacted DST was removed by subjecting the samples to gel filtration using PD-10 columns (GE Healthcare, Waukesha, WI). Each column was equilibrated with 25 mL of 0.05% SDS in PBS (pH = 7.6), and the protein fractions were eluted in 3.5 mL of 0.05% SDS in PBS (pH = 7.6). The desalted samples were boiled at 96–100°C for 10 min and cooled to room temperature before performing the affinity purification procedure.

4.3.7 *Affinity purification*

NeutrAvidin resin (Pierce, Rockford, IL) was used to separate DST-labeled proteins from unlabeled proteins following desalting [19]. The resin was first washed with PBS (pH = 7.6) at room temperature with constant agitation for 5 min. The resin was then collected by centrifugation (2000g, 5 min, 4°C) and the supernatant was removed. This washing procedure was repeated twice. Before adding the desalted samples to the washed resin, the samples were adjusted to 1% (v/v) NP-40 (Nonidet P40, Roche) and 0.05% SDS in PBS-PI. The samples were incubated with resin for 24 hours at

room temperature with constant agitation. The resin was collected by centrifugation (2000g, 5 min, 4°C) and the supernatants were removed. The resin was washed twice for 5 minutes at room temperature with 1% NP-40, then washed twice with PBS (pH = 7.6), and finally washed with freshly made 50 mM ammonium bicarbonate. Between each washing step the samples were centrifuged (2000g, 5 min, 4°C) and the supernatants were discarded. The resin was transferred to a microcentrifuge tube using 1 mL of 50 mM ammonium bicarbonate and centrifuged (2000g, 5 min, 4°C). The supernatants were discarded and the resin was treated with 500 µL of 2% β-mercaptoethanol in 50 mM ammonium bicarbonate for 1 hour at room temperature with constant agitation. The samples were centrifuged (2000g, 5 min, 4°C) and the supernatants containing the reduced proteins were saved. A second reduction step was performed for 30 min under identical conditions and the reduced eluates were combined. This combined sample was transferred to an empty chromatography spin-column (Bio-Rad Laboratories, Hercules, CA) and centrifuged (4000g, 2 min, 4°C) to remove any remaining resin from the solution.

4.3.8 Sample preparation for tandem mass spectrometry analysis

The eluate volume was reduced to ~ 100–200 µL by vacuum centrifugation. The samples were further concentrated via acetone precipitation. Proteins were precipitated by the addition of chilled acetone and the samples stored at -20°C overnight before centrifugation (14000g, 10 min, 4°C). The supernatants were discarded and the pellets were dried at room temperature for 1 hr. The pellets were resuspended in 40 µL of 8 M urea in 100 mM Tris-HCl (pH = 8.5). Each sample was further reduced by incubation

with 0.5 μL of 500 mM tris(2-carboxyethyl)phosphine (TCEP) for 20 min at room temperature with constant agitation. Cysteine residues were alkylated by the addition of 0.9 μL of 500 mM iodoacetamide. Proteolysis was initiated by incubating the samples with Endoproteinase Lys-C (1 μL of 0.1 $\mu\text{g}/\mu\text{L}$, Roche) for 4 hours at 37°C with constant agitation. Following digestion, the samples were diluted to 2 M urea by adding 120 μL of 100 mM Tris-HCl (pH = 8.5). The samples were treated with 1.6 μL of 100 mM CaCl_2 and further digested with 1.5 μL of 0.5 $\mu\text{g}/\mu\text{L}$ trypsin (Promega, Madison, WI) at 37°C for 16 hr with constant agitation. The digestion was quenched by the addition of 10 μL of 90% (v/v) formic acid.

Salts and detergents were removed by subjecting the samples to high performance liquid chromatography (HPLC). More specifically, peptides were desalted using the Alliance-HT HPLC (Waters Corporation, Milford, MA) equipped with a C8 peptide MacroTrap column (Microm Bioresources, Auburn, USA; 3 \times 8 mm; 200 mg capacity). A 40-min desalting step was performed for each sample. The desalting step was initiated with a 10-min wash step with 0.2% formic acid in water (Buffer A). A gradient was then started with Buffer A and gradually increased to achieve 90% of Buffer B (Buffer B = 0.2% formic acid in acetonitrile) within 23 min at a flow rate 250 $\mu\text{L}/\text{min}$. The gradient was stopped and the column was flushed with 100% of Buffer A for 7 min. A blank (water) run was performed between each sample. Fractions containing the eluted peptides were analyzed by MudPIT [16] at the Proteomic Exploration Laboratory at Caltech.

4.3.9 *Analysis of tandem mass spectrometry data*

The obtained tandem mass spectra were searched against the International Protein Index (IPI: Rat database version 3.47) using search engines Sorcerer (SageN Research Products, San Jose, CA) and MASCOT (Matrix Science, homepage: <http://www.matrixscience.com>) with a parent ion tolerance of 20 ppm. Alkylation of cysteine residues with iodoacetamide was specified as a fixed modification, while oxidation of methionine and acetylation of lysine and the N-terminus were specified as variable modifications. Variable methionine modifications related to the incorporation of Aha (loss of 4.986324 amu compared to Met) and DST labeling (+195.075623 amu) were also included. Protein identifications were viewed using Scaffold (version 01_07_00, Proteome Software, Inc., Portland, OR), and identifications were accepted if established with greater than 80% probability for peptides and greater than 99% probability for proteins (containing a minimum of 2 uniquely identified peptides). Probabilities were assigned using Peptide and Protein Prophet algorithms [20].

Gene-annotation enrichment analysis and pathway analysis were performed by importing the list of identified proteins in the form of a rat gene ID list into DAVID (Database for Annotation, Visualization, and Integrated Discovery, National Institute of Allergy and Infectious Disease, <http://david.abcc.ncifcrf.gov/home.jsp>). A modified Fisher exact *P* value of 0.05 was used in all tests.

4.4 Results and Discussion

4.4.1 *Cell synchronization through contact inhibition*

Synchronizing cells using contact inhibition relies on the natural cessation of cell division and migration as a result of physical contact with other cells or colonies [21]. This method of synchronization has been widely studied and shown to synchronize several types of fibroblasts [22, 23]. In this study, cell cycle synchronization in the G0/G1 stage was achieved by maintaining Rat-1 cells at confluence for 2 d in 100 mm diameter Petri dishes. The efficiency of synchronization in G0/G1 was evaluated by propidium iodide staining of cellular DNA and FACS analysis. Figure 4-4 shows FACS data obtained from examination of the DNA content of both unsynchronized (70% confluent) and synchronized (2 d at confluence) cultures. Unsynchronized cells (Figure 4-4 (A)) show three distinct cell populations (M1, M2, M3) that correspond to different stages of the cell cycle (G0/G1, S, G2/M). Maintaining cells at confluence for 2 d results in an increase in the percentage of cells in G0/G1, from 54% to 86%, and a corresponding decrease in the percentage of cells in S and G2/M (Figure 4-4 (B)). Allowing cells to remain at confluence for a third day only increased synchronization in G0/G1 by 1% (data not shown); however, this increase was accompanied by an increase in the number of apoptotic cells observed by FACS. Thus, prior to experiments, cells were kept at confluence for 2 d to achieve sufficient synchronization without inducing undesired apoptosis. Performing subsequent analyses on synchronized cells ensures that transcriptional and proteomic changes reflect differences in cell-material interactions and not changes in the cell cycle.

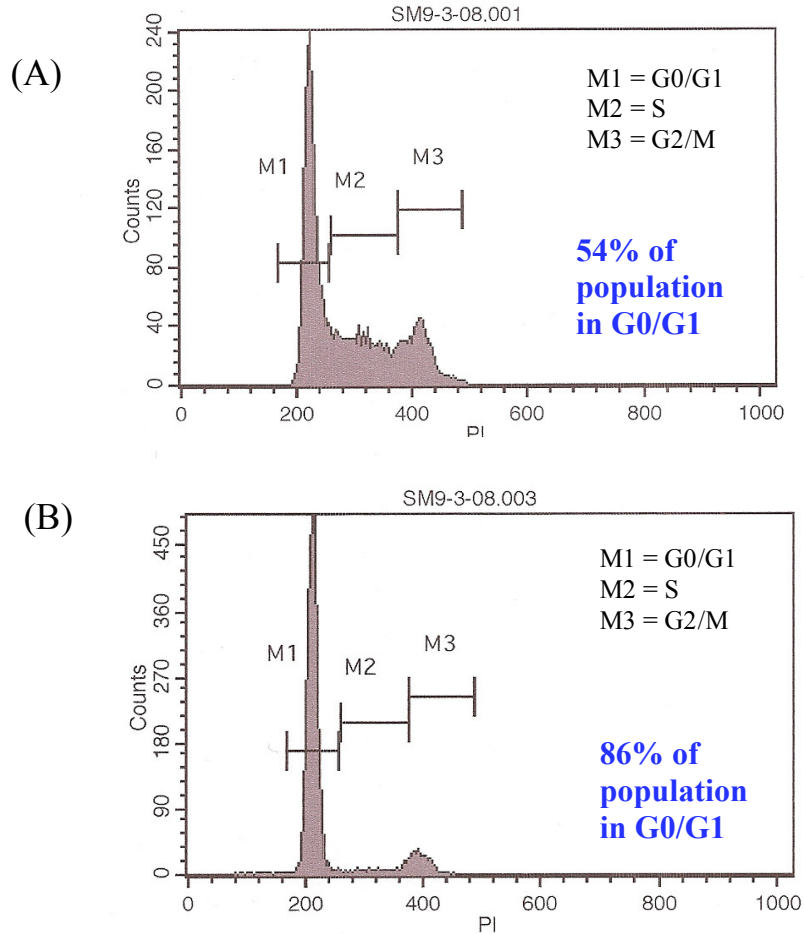


Figure 4-4. FACS analysis of Rat-1 fibroblasts before (A) and after (B) cell synchronization by contact inhibition. The cell population in (A) was ~ 70% confluent before FACS analysis, and the cell population in (B) was maintained at confluence for 2 d before FACS analysis. An increase in the percentage of cells in G0/G1 (54% to 86%) was observed as result of maintaining cells at confluence for 2 d.

4.4.2 Cell spreading results

To examine the sequence-specific nature of Rat-1 fibroblast spreading on aECM proteins in the presence of 2 mM Aha, a series of cell spreading experiments was performed on adsorbed protein films. Rat-1 cells attained a greater average spread area and exhibited well-spread morphologies on RGD-N₃ films after 2 hr of spreading compared to the RDG-N₃ films (Figures 4-5 and 4-6). Cell areas achieved on the RGD-

N₃ samples resemble those results obtained for FN, whereas the cell areas measured on the RDG-N₃ samples matched areas measured on the negative control of BSA (Figure 4-6). The observation that Rat-1 cells spread on RGD-N₃ films and not on RDG-N₃ films indicates that cells recognize the RGD cell-binding domain specifically. These results are in accordance with previous experiments performed in the presence of Met at longer time points ($t = 4$ hr) [12], demonstrating that Aha does not affect cell spreading.

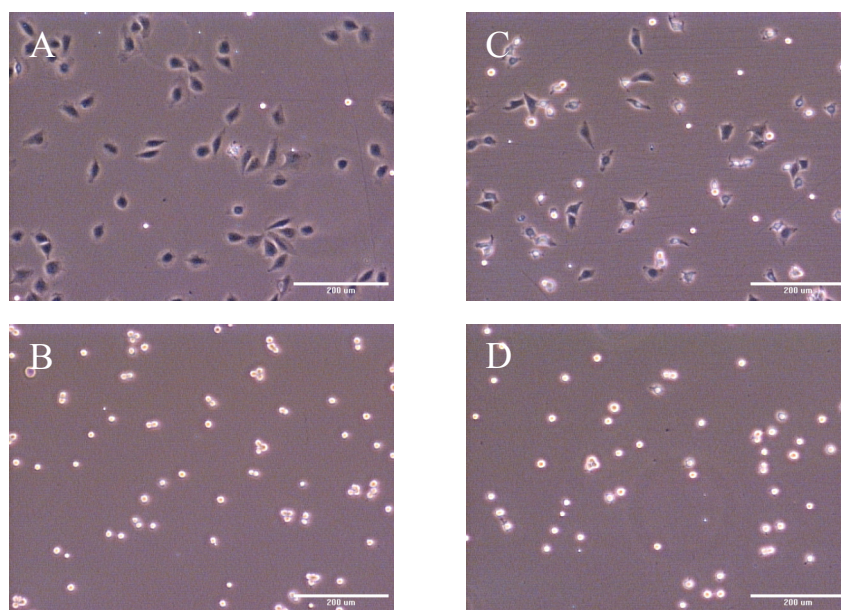


Figure 4-5. Images of cells captured after 2 hours of spreading. (A) FN, (B) BSA, (C) RGD-N₃, and (D) RDG-N₃. Scale bars represent 200 μm.

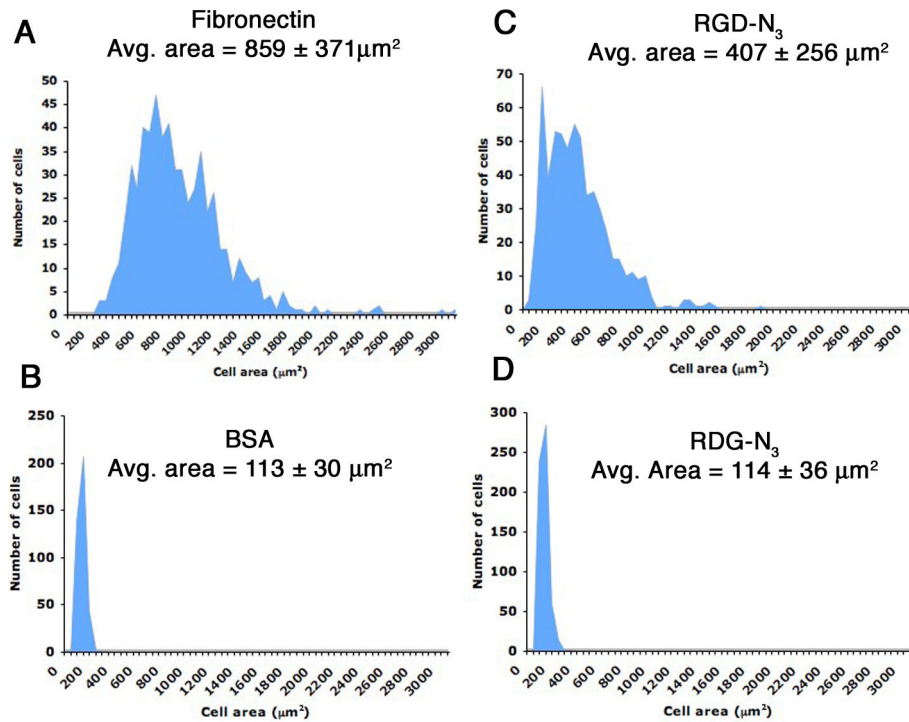


Figure 4-6. Rat-1 cell spread areas on (A) FN, (B) BSA, (C) RGD- N_3 , and (D) RDG- N_3 . The observation that Rat-1 cells spread well on RGD- N_3 films and not on RDG- N_3 films indicates that cells recognize the RGD cell-binding domain specifically in the presence of Aha.

4.4.3 mRNA microarray results

We have begun to compare the global transcriptional profile of Rat-1 fibroblast cells deposited on RGD- N_3 and RDG- N_3 proteins compared to FN using mRNA microarrays. Following cell spreading, mRNA was successfully extracted from cells and $\geq 2 \mu\text{g}$ of purified mRNA was obtained for each material investigated. All mRNA samples were processed and hybridized to Affymetrix GeneChips at the Muriel and Milliard Jacobs Center for Genes and Genomic Research at Caltech. One microarray chip per protein type was analyzed. The data collected from the microarray experiments was uploaded to the Resolver server at Caltech and analyzed. All data analysis was performed

utilizing built-in features of the Rosetta Resolver® Gene Expression Data Analysis System.

Ratio experiments were conducted using the Rosetta Resolver® Ratio Builder function to compare the expression levels of mRNA transcripts from cells deposited on different proteins. Two ratio experiments were performing using FN as a baseline with RGD-N₃ and RDG-N₃ as experimental samples (FN versus RGD, and FN versus RDG), and one ratio experiment was conducted with RDG-N₃ set as the baseline and RGD-N₃ as the experimental sample (RDG versus RGD). The data sets were then sorted using Excel to identify differentially expressed transcripts with ≥ 2.0 -fold change and a calculated *P* value ≤ 0.01 .

The extent to which aECM proteins elicit biological responses similar to that of the natural protein FN during early time points of cell spreading was examined by comparing the expression level of mRNA transcripts related to the process of cell-matrix adhesion. Table 4-1 shows a comparison of the fold changes between different genes for a selected number of differentially expressed transcripts and for other transcripts known to mediate cell spreading and focal adhesion formation [24]. These preliminary results show that many of the transcripts that encode for proteins involved in focal adhesion formation were not differentially expressed under these conditions.

Adhesion-related transcripts that were found to be differentially expressed on both RGD-N₃ and RDG-N₃ compared to FN include myosin regulatory light chain, α -actinin, and tropomyosin. A possible explanation for the observed downregulation in these transcripts detected on the RGD-N₃ surface compared to FN could involve the kinetics of the cellular spreading on RGD-N₃ proteins. Previous experiments using RGD-N₃ proteins

demonstrate that cells achieve a higher average spread area at longer time points ($516 \mu\text{m}^2$ versus $407 \mu\text{m}^2$) [12], suggesting that cells on RGD- N_3 in this experiment may exist in an early phase of spreading compared to FN samples. This early phase of spreading may only induce the production of a smaller number of transcripts that are needed to manufacture intracellular proteins to facilitate spreading, which correlates with the observation that cells attain a lower average spread area compared to FN at this time point. Moreover, it is important to note that cell areas were acquired following 2 hr of spreading while mRNA was extracted from cells after only 1 hr of spreading. The difference in cell spread areas between these surfaces at an earlier time point are likely to be greater than reported at 2 hr, which may also explain the differential expression of these genes. The downregulation of these transcripts on the RDG- N_3 surface compared to FN is expected, as the biologically inactive RDG domain does not promote spreading at any time point [12].

Ubiquitin D, a protein involved in mediating proteolysis, was found to be upregulated on both RGD- N_3 and RDG- N_3 samples compared to FN, suggesting that cells deposited on aECM proteins may be undergoing a higher level of protein degradation than cells deposited on FN [25]. Moreover, a downregulation in the transcription of the anti-apoptotic factor Bcl2-like 2 on RDG- N_3 samples implies that seeding cells on this surface may result in increased cell death [26]. Since anchorage-dependent cells like fibroblasts require contact with an underlying substrate for survival [27], the inability of cells to spread on RDG- N_3 samples complements the suppression of anti-apoptotic signals detected by microarray analysis. Both technical and biological replicates of these experiments are needed to validate the identification of differentially

expressed genes and to further investigate the role of other differentially expressed transcripts in cell-biomaterial interactions.

Table 4-1. Selected list of differentially expressed mRNA transcripts from ratio experiments with FN, RGD-N₃, and RDG-N₃ samples. All upregulated transcripts are shown in red, all downregulated transcripts are shown in blue, and dashed lines show transcripts that were not differentially expressed.

Protein product of mRNA transcript	FN vs. RGD	FN vs. RDG	RDG vs. RGD
actin	---	---	---
α -actinin	↓ 3 fold	↓ 3.9 fold	---
Bcl2-like 2	---	↓ 4.7 fold	---
collagen	---	---	---
fibroblast growth factor receptor 2	---	---	↑ 7.9 fold
fibronectin	---	---	---
filamin	---	---	---
focal adhesion kinase	---	---	---
heparin-binding EGF-like growth factor	↓ 2.7 fold	↓ 4.2 fold	---
lamin	---	---	---
laminin	---	---	---
myosin	---	---	---
myosin regulatory light chain	↓ 2.4 fold	↓ 4.1 fold	---
paxillin	---	---	---
profilin	---	---	---
Rho family GTPase 3	---	↓ 2.2 fold	---
Rho guanine nucleotide exchange factor	---	---	↑ 3.4 fold
talin	---	---	---
tropomyosin	↓ 3.3 fold	↓ 5.5 fold	---
ubiquitin D	↑ 3.3 fold	↑ 3.8 fold	---
vinculin	---	---	---

4.4.4 BONCAT results

Preliminary experiments investigating the proteomic profile of spreading Rat-1 fibroblasts on FN-coated surfaces have been performed. Rat-1 fibroblasts were deposited on adsorbed FN films and allowed to spread for 2 hr in the presence of 2 mM Aha or 2 mM Met. Cells were lysed in order to collect cellular proteins, and the extracted proteins were labeled with an affinity tag using click chemistry. Labeled proteins were affinity purified using NeutrAvidin resin and recollected for identification by performing an on-

resin reduction with β -mercapoethanol. Purified proteins obtained from the reduction step were analyzed by MudPIT [16].

Both MASCOT and Sorcerer search engines were used to identify proteins from obtained mass spectra. In order to be classified as newly synthesized using the incubation step with Aha, proteins were identified by a minimum of 2 unique peptides and had a greater than 99% protein identification probability. Although previous reports have required that peptides contain an Aha-derived modification to be considered newly translated, we have not included this restraint in our study as the only proteins identified in the Met sample, with the exception of a single ribosomal protein (ribosomal protein S27a), were derived from contaminants (e.g. trypsin, human keratins, and BSA). Therefore, all proteins identified in the Aha sample were considered newly synthesized during cell spreading experiments.

In the 2-hr interval of cell spreading examined, a total of 88 unique proteins were identified in the Aha sample. In particular, proteins shown to be important in mediating adhesion between cells and the extracellular matrix, such as vinculin, talin, filamin, vimentin, and α -actinin, were identified (Table 4-2) [24]. Examples of other proteins identified include actin, β -tubulin, and isoforms of myosin light and heavy chains. Proteins involved in translation and cell proliferation were also identified, such as ribosomal proteins (40S ribosomal proteins S6 and S8, and 60S ribosomal protein L7a) and isomerases (protein disulfide-isomerase A3 and peptidyl-prolyl cis-trans isomerase A), respectively [6]. In accordance with preliminary microarray results, α -actinin, myosin regulatory light chain 2, and tropomyosin were detected as proteins synthesized during the Aha pulse.

Table 4-2. List of identified newly synthesized proteins shown to play a role in cell-ECM interactions, focal adhesion formation, and cytoskeletal reorganization [24].

Identified newly synthesized proteins important in cell-ECM interactions and cytoskeletal reorganization		
	actin, cytoplasmic 2	
	α -actinin-1	
	collagen, type 1, α 1	
	collagen, α -2(I) chain	
	cofilin-1	
	filamin-A	
	isoform I of fibronectin	
	laminin β -1	
	myosin-9	
	myosin-10	
	myosin regulatory light chain 2-B	
	profilin-1	
	talin	
	tropomyosin α -4 chain	
	isoform of tubulin β -3 chain	
	isoform of tubulin β -5 chain	
	vimentin	
	vinculin	

Gene ontology analysis of identified proteins in the Aha sample was performed using DAVID. The gene IDs for the identified proteins were determined using the RGD and imported as a gene list. The DAVID program sorted the list into bins according to Panther annotation terms [28]. Figure 4-7 shows an example of an analysis conducted using the identified proteins and sorted with Panther annotation terms restricted to “molecular function”. The analysis from DAVID showed that a significant number of identified proteins are involved in the regulation of the actin cytoskeleton. This result correlates with phenotypic observations demonstrating that cells are well spread on FN, as spreading and extension of the cell membrane involves the reorganization of the actin cytoskeleton and the formation of new sites of actin polymerization [29]. A majority of identified proteins were binned into the category of nucleic acid binding, a result that corresponds to observations made from previous dye-labeling experiments illustrating

that newly synthesized proteins are highly concentrated near the nucleus and in the nucleoli [18]. Overall, these preliminary results also highlight the diversity in molecular function of proteins identified using BONCAT that provide a more integrated characterization of cell-biomaterial interactions.



















Term	RT	Genes	Count	%	P-Value
MF00261:Actin binding cytoskeletal protein	RT		18	21.4	1.5E-9
MF00091:Cytoskeletal protein	RT		15	17.9	7.5E-7
MF00077:Chaperone	RT		8	9.5	3.5E-6
MF00262:Non-motor actin binding protein	RT		15	17.9	1.5E-3
MF00250:Serine protease inhibitor	RT		11	13.1	2.7E-3
MF00236:Exoribonuclease	RT		5	6.0	3.0E-3
MF00230:Actin binding motor protein	RT		8	9.5	3.2E-3
MF00210:Hsp 90 family chaperone	RT		3	3.6	5.2E-3
MF00219:Annexin	RT		4	4.8	7.2E-3
MF00209:Hsp 70 family chaperone	RT		3	3.6	1.0E-2
MF00087:Transfer/carrier protein	RT		6	7.1	1.5E-2
MF00169:Other isomerase	RT		4	4.8	1.6E-2
MF00254:Actin and actin related protein	RT		6	7.1	1.7E-2
MF00188>Select calcium binding protein	RT		5	6.0	2.0E-2
MF00166:Isomerase	RT		4	4.8	2.2E-2
MF00075:Ribosomal protein	RT		9	10.7	2.6E-2
MF00042:Nucleic acid binding	RT		28	33.3	2.9E-2
MF00099:Small GTPase	RT		10	11.9	4.0E-2

Figure 4-7. Gene ontology analysis of newly synthesized proteins in Aha-treated samples using DAVID. Of the 88 candidate proteins submitted, 84 were assigned DAVID IDs, and 69 were included in the chart. Several proteins are listed in multiple bins. Each molecular function (MF) annotation term is listed, followed by a link for related terms (RT). The number and percentage of genes included in the annotation binning is listed along with the calculated *P* value for each term.

Pathway analysis was also performed using DAVID to determine whether certain cellular pathways were considered enriched within the provided gene list as compared to random chance. Figure 4-8 shows the KEGG (Kyoto Encyclopedia for Genes and Genomes, <http://www.genome.jp/kegg/>) pathways that were detected with a modified Fisher exact P value ≤ 0.05 . This analysis further supports the observation that cellular processes including focal adhesion formation, regulation of the actin cytoskeleton, as well as extracellular matrix (ECM)-receptor interactions are likely occurring within the cell during spreading on FN. In addition to processes related to cell-ECM interactions, metabolic processes were also considered enriched including glycolysis/gluconeogenesis, pyruvate metabolism, and carbon fixation.










Category	Term	RT	Genes	Count	%	P-Value
KEGG_PATHWAY	Glycolysis / Gluconeogenesis	RT		6	7.1	1.5E-4
KEGG_PATHWAY	Focal adhesion	RT		9	10.7	8.2E-4
KEGG_PATHWAY	Cell Communication	RT		7	8.3	2.1E-3
KEGG_PATHWAY	Antigen processing and presentation	RT		5	6.0	1.8E-2
KEGG_PATHWAY	Carbon fixation	RT		3	3.6	2.0E-2
KEGG_PATHWAY	Regulation of actin cytoskeleton	RT		7	8.3	2.4E-2
KEGG_PATHWAY	ECM-receptor interaction	RT		4	4.8	4.2E-2
KEGG_PATHWAY	Ribosome	RT		4	4.8	4.5E-2
KEGG_PATHWAY	Pyruvate metabolism	RT		3	3.6	4.5E-2

Figure 4-8. Pathway analysis of the imported list from Aha-treated samples using DAVID. The associated KEGG pathway is listed as a term along with a link for related terms (RT). The number and percentage of genes included in the annotation binning is listed along with the calculated P value for each pathway. Of the 84 proteins assigned DAVID IDs, 29 were included in the pathway analysis. Several proteins are listed in multiple pathways.

4.5 Conclusions and Future Work

Preliminary experiments have been conducted to correlate the phenotypic behavior of cells deposited on aECM proteins and FN at early time points of cell

spreading with intracellular changes in gene transcription and protein translation. Cell spreading experiments were performed to provide a quantitative assessment of cell morphology on different surfaces, and changes in mRNA transcript levels were analyzed using microarray technology. The identification of newly synthesized proteins produced during cell-biomaterial interaction was accomplished by employing the proteomic technique, BONCAT. These experiments provide valuable information regarding cell-biomaterial interaction that can be used in the design of future aECM proteins.

Cell spreading experiments demonstrated that cells attained different degrees of spreading on aECM proteins and FN. Cells appeared well-spread on FN and attained the highest average spread area on these surfaces. Cells also appeared spread on RGD-N₃, though they attained a slightly lower average spread area at this time point compared to FN. In contrast, cells did not spread and remained round with a low average spread area on RDG-N₃ samples. These differences in morphological behavior were reflected in the transcription levels of three mRNA transcripts: α -actinin, myosin regulatory light chain 2, and tropomyosin. Differences in the expression levels of other mRNA transcripts that encode for proteins involved in cell-ECM interactions were not detected at this time point. Future studies with microarrays will use both biological and technical replicates at a time point matching that for the cell spreading and BONCAT experiments to validate these conclusions and to examine the role of other differentially expressed mRNA transcripts in mediating cell spreading on aECM proteins.

BONCAT experiments were initiated using FN samples, and 88 unique proteins were identified as newly synthesized during the Aha pulse. Proteins involved in focal adhesion formation and the regulation of the actin cytoskeletal were found to be newly

synthesized, as were other proteins involved in metabolic processes such as glycolysis and gluconeogenesis. Future BONCAT experiments will compare the proteomic profiles of cells deposited on aECM proteins with varying biological and mechanical properties.

4.6 References

1. Maskarinec, S.A., and D.A. Tirrell, *Protein engineering approaches to biomaterials design*. Current Opinion in Biotechnology, 2005. **16**(4): 422-426.
2. Lutolf, M.P., and J.A. Hubbell, *Synthetic biomaterials as instructive extracellular microenvironments for morphogenesis in tissue engineering*. Nature Biotechnology, 2005. **23**(1): 47-55.
3. Heilshorn, S.C., J.C. Liu, and D.A. Tirrell, *Cell-binding domain context affects cell behavior on engineered proteins*. Biomacromolecules, 2005. **6**(1): 318-323.
4. Allen, L.T., et al., *Interaction of soft condensed materials with living cells: Phenotype/transcriptome correlations for the hydrophobic effect*. Proceedings of the National Academy of Sciences of the United States of America, 2003. **100**(11): 6331-6336.
5. Gallagher, W.M., et al., *Molecular basis of cell-biomaterial interaction: Insights gained from transcriptomic and proteomic studies*. Biomaterials, 2006. **27**(35): 5871-5882.
6. Xu, J.L., et al., *Comparative proteomics profile of osteoblasts cultured on dissimilar hydroxyapatite biomaterials: An iTRAQ-coupled 2-D LC-MS/MS analysis*. Proteomics, 2008. **8**(20): 4249-4258.
7. Klapperich, C.M., and C.R. Bertozzi, *Global gene expression of cells attached to a tissue engineering scaffold*. Biomaterials, 2004. **25**(25): 5631-5641.
8. Jones, J.A., et al., *Proteomic analysis and quantification of cytokines and chemokines from biomaterial surface-adherent macrophages and foreign body*

- giant cells*. Journal of Biomedical Materials Research Part A, 2007. **83A**: 585-596.
9. Chang, D.T., et al., *Lymphocyte/macrophage interactions: Biomaterial surface-dependent cytokine, chemokine, and matrix protein production*. Journal of Biomedical Materials Research Part A, 2008. **87A**(3): 676-687.
 10. Derhami, K., et al., *Proteomic analysis of human skin fibroblasts grown on titanium: Novel approach to study molecular biocompatibility*. Journal of Biomedical Materials Research, 2001. **56**(2): 234-244.
 11. Williams, D., *The golden anniversary of titanium biomaterials*. Medical Device Technology, 2001. **12**(7): 8-11.
 12. Carrico, I.S., et al., *Lithographic patterning of photoreactive cell-adhesive proteins*. Journal of the American Chemical Society, 2007. **129**(16): 4874-4875.
 13. Nowatzki, P.J., et al., *Mechanically tunable thin films of photosensitive artificial proteins: Preparation and characterization by nanoindentation*. Macromolecules, 2008. **41**(5): 1839-1845.
 14. Dieterich, D.C., et al., *Selective identification of newly synthesized proteins in mammalian cells using bioorthogonal noncanonical amino acid tagging (BONCAT)*. Proceedings of the National Academy of Sciences of the United States of America, 2006. **103**(25): 9482-9487.
 15. Dieterich, D.C., et al., *Labeling, detection and identification of newly synthesized proteomes with bioorthogonal non-canonical amino-acid tagging*. Nature Protocols, 2007. **2**: 532-540.

16. Delahunty, C.M. and J.R. Yates, *MudPIT: multidimensional protein identification technology*. Biotechniques, 2007. **43**: 563-569.
17. Diamond, R., and S. DeMaggio, eds., *In Living Color*. Protocols in Flow Cytometry and Cell Sorting, 2000, New York: Springer Lab Manuals.
18. Beatty, K.E., et al., *Fluorescence visualization of newly synthesized proteins in mammalian cells*. Angewandte Chemie-International Edition, 2006. **45**(44): 7364-7367.
19. Hodas, J.L., *Personal communication*, 2009.
20. Nesvizhskii, A.I., et al., *A statistical model for identifying proteins by tandem mass spectrometry*. Analytical Chemistry, 2003. **75**(17): 4646-4658.
21. Jackman, J., and P.M. O'Connor, *Methods for synchronizing cells at specific stages of the cell cycle*. Current Protocols in Cell Biology, 2001. 8.3.
22. Holley, R.W., and J.A. Kiernan, *Contact Inhibition of Cell Division in 3T3 Cells*. Proceedings of the National Academy of Sciences of the United States of America, 1968. **60**(1): 300-304.
23. Sun, X.Z., et al., *Cell-cycle synchronization of fibroblasts derived from transgenic cloned cattle ear skin: effects of serum starvation, roscovitine and contact inhibition*. Zygote, 2008. **16**(2): 111-116.
24. Zamir, E. and B. Geiger, *Molecular complexity and dynamics of cell-matrix adhesions*. Journal of Cell Science, 2001. **114**(20): 3583-3590.
25. Bates, E.F.M., et al., *Identification and analysis of a novel member of the ubiquitin family expressed in dendritic cells and mature B cells*. European Journal of Immunology, 1997. **27**(10): 2471-2477.

26. Rat Genes, RGD ID 620717, Rat Genome Database Web Site. February 2009, *Medical College of Wisconsin, Milwaukee, Wisconsin*: <http://rgd.mcw.edu/>.
27. Kato, G. and S. Maeda, *High-level expression of human c-Src can cause a spherical morphology without loss of anchorage-dependent growth of NIH 3T3 cells*. Federation of European Biochemical Societies Letters, 1997. **411**(2-3): 317-321.
28. Thomas, P.D., et al., *PANTHER: A library of protein families and subfamilies indexed by function*. Genome Research, 2003. **13**(9): 2129-2141.
29. McLeod, S.J., et al., *The Rap GTPases regulate integrin-mediated adhesion, cell spreading, actin polymerization, and Pyk2 tyrosine phosphorylation in B lymphocytes*. Journal of Biological Chemistry, 2004. **279**(13): 12009-12019.

5 Depth Perception: Quantifying Cellular Traction Forces in Three Dimensions

The work presented here is taken from:

*Maskarinec, S.A., *Franck C., Tirrell, D.A., and G. Ravichandran. *Depth Perception: Quantifying Cellular Traction Forces in Three Dimensions*, submitted for publication.

*Signifies equal contributions

5.1 Abstract

Cells engage in mechanical force exchange with their extracellular environment through tension generated by the cytoskeleton. A new method, combining laser scanning confocal microscopy (LSCM) and digital volume correlation (DVC), enables tracking and quantification of cell-mediated deformation of the extracellular matrix in all three spatial dimensions. Time-lapse confocal imaging of migrating 3T3 fibroblasts on fibronectin (FN)-modified polyacrylamide gels of varying thickness reveals significant in-plane (x , y) and normal (z) displacements, and illustrates the extent to which cells, even in nominally two-dimensional environments, explore their surroundings in all three dimensions. The magnitudes of the measured displacements are independent of the elastic moduli of the gels. Analysis of the normal displacement profiles suggests that normal forces play important roles even in two-dimensional cell migration.

5.2 Introduction

The measurement of cellular traction forces has been of increasing interest since the discovery that the mechanical properties of the cellular microenvironment can direct many important cellular processes including spreading, migration, and differentiation [1-4]. It is now widely accepted that mechanical properties must be considered along with chemical signals if we are to understand how cells integrate environmental cues to modulate their behavior [5-8]. The correlation between cell-induced deformations in materials and biochemical signaling and regulation, particularly focal adhesion formation and clustering, has been investigated through the use of a variety of techniques including surface wrinkling, displacement-tracking using traction force microscopy (TFM), and bending of pillar arrays [9-15]. These methods have yielded substantial insight into cellular behavior, but are inherently restricted to two-dimensional (2-D) analysis and interpretation of cell-matrix interactions. Furthermore, these approaches calculate stresses by comparing images before and after cell detachment [10], thus providing only snapshots of cell behavior rather than dynamic analyses of the processes by which cells explore their microenvironments.

In this report, we demonstrate the capability to dynamically track and quantify cellular traction forces in three dimensions (3-D). Mechanical interactions between 3T3 fibroblasts and FN-modified polyacrylamide gels are quantified dynamically by computing the displacement and traction fields generated by motile cells. Use of a recently developed digital volume correlation (DVC) method [16] allows three-dimensional displacements and traction fields to be determined directly from volumetric confocal image stacks, and obviates the need for complex inverse formulations [10]. The

method has a temporal resolution that permits confocal imaging over time scales relevant for the migration of anchorage-dependent cells such as endothelial cells and fibroblasts [17].

The 3-D character of this approach relies on the use of laser scanning confocal microscopy (LSCM), which has the distinct advantage over conventional microscopic imaging in that it provides positional information along the z-axis, i.e, in the direction normal to the plane of the sample [18]. A schematic of the experimental setup is shown in Figure 5-1 (A). The range of gel thicknesses investigated was between 20–100 μm , and the height contribution of the covalently attached FN layer measured by confocal scanning was less than 1 μm . Samples were produced with two different crosslink densities to achieve physiologically relevant values of the elastic modulus (E , 0.82 (\pm 0.23) kPa and 9.64 (\pm 1.12) kPa) [19]. Red fluorescent microspheres (0.5 μm in diameter) were embedded during gel formation to enable tracking of cell-generated deformations by DVC. Simultaneous visualization of the red fluorescent markers and the cell was accomplished by allocating separate lasers and filters along with the use of a 3T3 fibroblast cell line transfected with a vector encoding a green fluorescent protein (GFP)-actin fusion construct. Cells were deposited on the surfaces of the FN-modified samples and incubated overnight to ensure attachment before imaging. Isolated cells were imaged every 35 minutes for up to 24 hours within a typical field of view of 150 x 150 x 150 μm^3 . Figure 5-1 (B) shows a cross-sectional view of a typical confocal stack. Imaging of isolated cells ensures that neighboring cells do not contribute to the measured displacements.

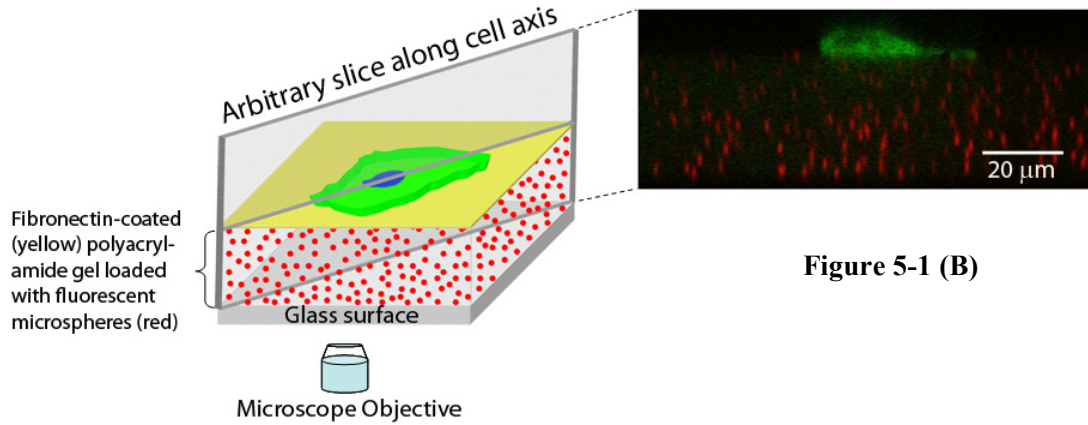


Figure 5-1 (A)

Figure 5-1. (A) Schematic of a representative gel sample with microscope objective. 3-D confocal image stacks are acquired every 35 minutes through an inverted microscope that captures the emission from both the fluorescent microspheres (red) and GFP-transfected cells (green). The 35-minute time interval was chosen for investigating fibroblast migration patterns given measured migration speeds of $\sim 8 \mu\text{m}/\text{hour}$, as well as to minimize phototoxicity to cells. (B) Cross-sectional view of a typical confocal image stack. Cells migrate on the surface of the FN-modified polyacrylamide gel, and the corresponding displacements in the underlying gel are monitored. The red fluorescent microspheres are visible within the gel.

As the cell explores the substrate and probes its resistance to deformation, displacements are determined by comparing successive stacks. Most importantly, the DVC method can map such displacements in all three dimensions by comparing uniquely defined cubic subsets within confocal stacks that are obtained sequentially [16]. This technique can detect both translational and rotational changes, and is valid for large deformations. The technique is sensitive to displacement changes greater than or equal to

0.12 μm with a spatial resolution of approximately 2 μm , and can reach finer (submicron) spatial resolution at a greater computational cost.

5.3 Materials and Methods

5.3.1 Preparation of activated coverslips

Glass coverslips (Gold-Seal coverslip No 0, Electron Microscopy Sciences, Hatfield, PA) were chemically modified to allow covalent attachment of polyacrylamide films using previously established protocols with some modifications [10, 20]. Briefly, coverslips were rinsed with ethanol before being placed in a dish containing a solution of 0.5% (v/v) 3-aminopropyltrimethoxysilane (Gelest, Inc., Morrisville, PA) in ethanol for 5 minutes. The coverslips were removed from the dish and rinsed with a stream of ethanol before being immediately placed treated-side up in a solution of 0.1% (v/v) glutaraldehyde (Polysciences, Inc., Warrington, PA) in water for 30 minutes. Activated coverslips were rinsed with a stream of deionized water and left to dry for several hours at 60°C. Treated coverslips were covered and stored for up to one week after preparation.

5.3.2 Preparation of polyacrylamide films

Thin films of polyacrylamide were generated and fused to functionalized coverslips using a protocol adopted from previous reports with some modifications [10, 20]. Solutions of acrylamide (40% w/v, Bio-Rad, Hercules, CA) and N, N-methylene-bis-acrylamide (BIS, 2.5% w/v, Bio-Rad, Hercules, CA) were mixed with distilled water to obtain the following concentrations used for tested samples: 1) 10% acrylamide and 0.015% BIS, and 2) 10% acrylamide and 0.0075% BIS. Adjusting the concentration of

BIS in the formulation was used to create substrates with varying mechanical properties. To these solutions, red fluorescent microparticles (0.5 μm , carboxylate-modified, Molecular Probes, Carlsbad, CA) were vortexed for 10 seconds and subsequently added in a volume ratio of 9:100. Crosslinking was initiated through the addition of ammonium persulfate (Sigma-Aldrich, St. Louis, MO) and N, N, N',N'-tetramethyl-ethylenediamine (Invitrogen, Carlsbad, CA). The samples were vortexed for 10 seconds, and 5–7 microliters of the acrylamide solution was pipetted on the surface of a precleaned microscope slide (No. 1, 75 mm x 25 mm, Corning, Corning, NY). To generate thicker films, 20–40 microliters of the solution was used. The activated surface of the coverslip was then placed on top of the acrylamide droplet, causing the solution to flatten under the weight of the coverslip. The entire assembly was left undisturbed for 5 minutes, and then placed in a Petri dish (100 mm diameter, VWR, West Chester, PA) containing distilled water for 10–30 minutes. The bonded sample was then peeled from the microscope slide using forceps and thoroughly rinsed with several volume changes of water.

5.3.3 *Functionalization of polyacrylamide films with fibronectin*

In order to promote cell attachment to polyacrylamide films, a saturating density of fibronectin was conjugated to the gel surface using the heterobifunctional crosslinker, sulfo-SANPAH (Pierce Chemicals, Rockford, IL). Adopting procedures outlined previously [10, 20], polyacrylamide gel samples were briefly dried in air to rid the surface of excess water before 200 μl of sulfo-SANPAH in water (1.0 mg/ml) was applied. The surface of the sample was then exposed to unfiltered UV light from a high-pressure mercury lamp (Oriel Q 100W at 5 A, > 10 min warm up time) at a distance of 10

inches for 7.5 minutes. The darkened sulfo-SANPAH solution was removed from the surface of the gel and replaced with another 200 μ l aliquot and irradiated for another 7.5 minutes for a total of 15 minutes of UV exposure. The samples were then rinsed vigorously with water for 5 minutes, and adhered to the bottom of 60 mm Petri dishes (Becton Dickinson, Franklin Lakes, NJ) by applying a thin layer of vacuum grease (Dow Corning, Midland, MI) around the perimeter of the unmodified side of the coverslip. The samples were rinsed twice with phosphate buffered saline (PBS, pH 7.4), covered with a solution of fibronectin (FN, 0.2 mg/ml, Millipore, Billerica, MA) and left undisturbed overnight at 4°C. Following overnight incubation, the substrates were rinsed three times with PBS.

5.3.4 *Characterization of FN-modified films*

Comparison of the relative amounts of covalently attached FN on polyacrylamide (PA) samples made with varying percentages of crosslinker was conducted using a commercially available bicinchoninic acid (BCA) assay kit (Sigma-Aldrich, St. Louis, MO). In this assay, the relative protein concentration is quantified by measuring the absorbance at 562 nm using a plate reader and comparing the measured values to a standard curve generated using known amounts of FN (Tecan Sapphire, Tecan Group Ltd., Männedorf, Switzerland). A set of FN-modified samples (lacking embedded microspheres) was prepared as described above and placed in a 6-well plate (Becton Dickinson, Franklin Lakes, NJ). Negative controls consisting of unmodified samples made with similar crosslinker percentages (% BIS) were also prepared. All samples were

then treated for 1 hour at 60°C followed by an absorbance reading. These experiments were repeated three times in triplicate for each % BIS.

5.3.5 *Film thickness measurements*

The thickness of the sample was determined by calculating the distance from the bottom of the glass surface to the disappearance of bead fluorescence at the top of the sample using a confocal microscope. The sample thicknesses were controlled by adjusting the total volume of the acrylamide mixture used to make the samples.

5.3.6 *Mechanical characterization of thin films*

The mechanical properties of the substrates were determined by performing both unconfined and confined compression testing on cylindrical polyacrylamide specimens using a custom-built compression setup ([16], Figure 5-2). The typical sample dimensions were 8 mm in diameter and 4 mm in height. The displacements during each compression increment were controlled using a digital micrometer with a resolution of 1 μm . The resulting nominal force was measured using a 10 g load cell (A.L. Design, Buffalo, NY). For each volume fraction of BIS crosslinker used, 6–8 samples were tested in both confined and unconfined uniaxial compression.

For unconfined tests, gel samples were cast in a circular washer secured to the bottom of a 60 mm diameter plastic Petri dish. Following polymerization (~ 2–5 minutes), the washer was removed from the dish and the sample was hydrated and left covered at room temperature overnight to ensure adequate swelling. Prior to compression, the alignment of the setup with the sample was inspected to ensure pure

compression along the nominal loading axis. The samples were compressed between the top platen of the compression setup and the bottom of the Petri dish with a nominal strain increment of 1–2%. Nominal strain increments are defined by the ratio of the displacement increment resulting from the compression to the original sample height. Force values were obtained continuously during each 5-minute increment in order to detect any time-dependent relaxation of the material during the compression. The total applied nominal compressive strain was ~ 13 –15%. After complete loading, the sample was successively unloaded using the same strain increments to record the entire loading-unloading cycle.

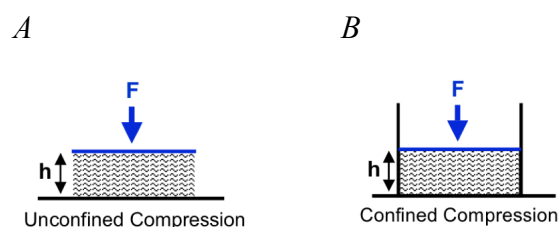


Figure 5-2. Detailed schematic of the compression tests: (A) Unconfined compression tests, (B) Confined compression tests.

5.3.7 Cell culture

Prior to depositing cells, FN-modified gel samples were equilibrated in growth media at 37°C for 15 minutes. Swiss 3T3 fibroblasts transfected with a GFP-actin vector (a gift from Professor Scott Fraser, California Institute of Technology) were cultured in Dulbecco's Modified Eagle Medium (DMEM) supplemented with 10% fetal bovine serum, 50 ug/ml streptomycin, and 50 U/ml penicillin (Invitrogen, Carlsbad, CA). For all experiments, cells were first treated with Mitotracker Deep Red (Molecular Probes, Carlsbad, CA) for 45 minutes before passaging with trypsin-EDTA (0.05%, Invitrogen,

Carlsbad, CA). Mitotracker dyes accumulate in actively respiring mitochondria providing a second method for tracking cells and determining cell viability. Cells were plated at density of $\sim 40,000$ cells/coverslip, and incubated on samples for 8–12 hours before imaging.

5.3.8 *Confocal microscopy and time-lapse imaging*

3-D image stacks were acquired using a Nikon C-1 confocal system mounted on a TE-2000-U inverted optical microscope. A 40x CFI planar fluor air objective with a numerical aperture of 0.6 was used in all experiments. Three laser lines were used to image the cells and the fluorescent microparticles: Argon (488 nm) laser for the GFP-actin, a green HeNe (543 nm) for the microparticles in the polyacrylamide gels, and a red HeNe (633 nm) for the Mitotracker Deep Red for mitochondrial labeling. Confocal stacks were acquired every 35 minutes for several hours at a resolution of $512 \times 512 \times H$ ($X \times Y \times Z$) pixels³, where H ranges from 120–250 pixels. Typical imaging areas were between $150\text{--}200 \mu\text{m}^2$; images with a larger field of view were captured before and after experiments to ensure that measured displacements were not the result of contributions from neighboring cells. Physiological conditions were maintained during all times by housing the entire confocal microscope inside a custom-built temperature controlled chamber. The temperature was controlled using a feedback controlled heater, Air-Therm ATX Air Heater Controller (World Precision Instruments, Sarasota, FL), and an arterial blood gas mixture (5% CO₂, 20% O₂, 75% N₂) was injected into the chamber in order to maintain appropriate culturing conditions.

5.3.9 Calculation of displacements, strains, stresses, and forces

The full-field 3-D displacements are determined using LSCM and DVC as previously described [16]. In brief, a digital volume cross-correlation algorithm is used to determine the 3-D cell-induced displacement fields from confocal volume stacks during each time increment. Once the entire displacement field is determined, the strain tensor of the material substrate is computed using a displacement-gradient technique [16]. The material stress tensor $\boldsymbol{\sigma}$ is then determined through the materials' constitutive relations, which were determined from the above characterization tests describing the material as a linearly elastic, isotropic, incompressible material. Hence, $\boldsymbol{\sigma}$ is calculated as $\boldsymbol{\sigma} = 2\mu\boldsymbol{\epsilon}$, where $\boldsymbol{\epsilon}$ is the computed strain tensor, and μ is the shear modulus and is related to Young's modulus by $E = \mu / (1 + \nu)$, with $\nu = 0.5$.

Traction forces are calculated along the top surface plane, directly beneath the cell using the known Cauchy relationship: $\mathbf{T} = \boldsymbol{\sigma}\mathbf{n}$, where \mathbf{T} is the 3-D surface traction vector, $\boldsymbol{\sigma}$ is the material stress tensor, and \mathbf{n} is the surface normal.

In order to establish the maximum resolution of the DVC-LSCM technique for the presented results here, several sets of confocal images of FN-modified polyacrylamide substrate samples were obtained under zero-load conditions at physiological conditions as described above. The computed uncertainties in the displacement measurements were found to be close to the previously published uncertainties [16], establishing subpixel or submicron resolution.

5.3.10 *Traction force inhibition using blebbistatin*

Time-lapse imaging of fibroblasts treated with the myosin-II-specific blocker, blebbistatin (Sigma-Aldrich, St. Louis, MO), were performed to establish that measured displacement were indeed cell-mediated and not the result of thermal fluctuations within the polyacrylamide sample. Blebbistatin is commonly used in traction force measurements to inhibit actinomyosin contraction in non-muscle cells [21, 22]. Confocal stacks of individual cells were captured 1–2 hours before treatment with 12.5 μM blebbistatin in dimethyl sulfoxide, and up to 4 hours post-treatment. Identical experiments were performed without cells and in the presence of blebbistatin.

5.4 **Results and Discussion**

5.4.1 *Characterization of FN-modified films*

The protein content for both sets of samples were similar ($91.6 \pm 52.4 \mu\text{g}$ for 0.015% BIS, and $82.7 \pm 48.7 \mu\text{g}$ for 0.0075% BIS), and lie within the standard deviation calculated from the tested samples. These results confirm that the prepared samples display similar amounts of FN on the surface, and that changes in cell behavior result from differences in mechanical properties and not some difference in the chemical composition of the surfaces.

5.4.2 *Mechanical Testing*

Figure 5-3 shows the raw data for an incremental loading cycle highlighting negligible time-dependent behavior of the polyacrylamide samples, and Figure 5-4 shows the loading-unloading stress strain curve for a typical sample. The Young's modulus for

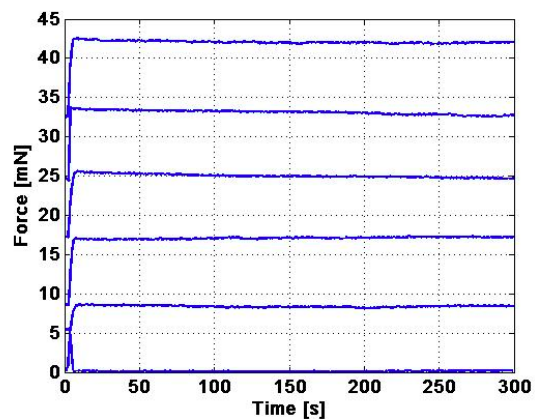


Figure 5-3. Incremental loading tests using polyacrylamide samples highlighting the negligible time-dependent relaxation behavior of the material. Force values were obtained continuously during 5-minute increments.

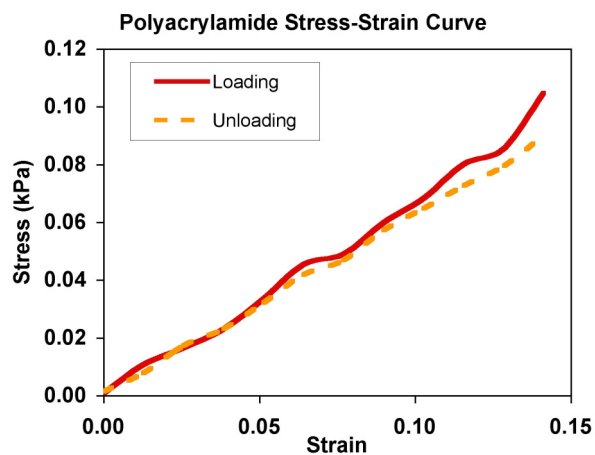


Figure 5-4. Representative stress-strain curves of loading and unloading cycles on cylindrical hydrated polyacrylamide samples demonstrating a linear elastic material response with negligible hysteresis.

the polyacrylamide samples was calculated from each stress-strain curve using the relationship:

$$E = \frac{\sigma}{\varepsilon} = \frac{F/A}{\Delta h/h}$$

where σ and ε denote the uniaxial stress and strain, and can be expressed as the applied force per sample contact area, and change in sample height over its original height.

Table 5-1 summarizes the unconfined compression test results for two different crosslinker volume fractions.

Table 5-1. Mechanical characterization results for polyacrylamide substrates from unconfined uniaxial compression experiments.

Crosslinker Volume Fraction	Young's Modulus (kPa)
0.015% BIS	9.64 ± 1.12
0.0075% BIS	0.82 ± 0.23

In order to determine Poisson's ratio for each polyacrylamide gel, cylindrical specimens were cast and polymerized in a confined Teflon sleeve 15 mm in diameter and about 8 mm in height. Samples were hydrated following the same protocol as described above. The samples were compressed following the same loading-unloading protocol as for the unconfined test. Using the determined Young's modulus value of the unconfined test case and observing that the further compression beyond an initial compression strain of $\sim 0.25\%$ was not possible (due to the Poisson effect), Poisson's ratio was determined to be ~ 0.48 – 0.5 according to the following equation:

$$\bar{E} = \frac{\sigma}{\varepsilon} = \frac{1-\nu}{(1+\nu)(1-2\nu)} E$$

where \bar{E} denotes the measured confined compression modulus, ν is the Poisson's ratio, and E is the Young's modulus as determined from unconfined compression test. From this set of experiments, Poisson's ratio was taken to be 0.5, and the material behavior is described as a linearly elastic, isotropic, and incompressible for all traction force calculations.

5.4.3 *Analysis of cellular traction forces in 3D: in-plane and normal components*

Detection of both normal and in-plane displacements allows a more complete analysis of cellular forces than does consideration of only in-plane (2-D) displacements [10]. Figure 5-5 shows the extent of cell-induced deformation as a function of depth within each substrate, and shows clearly that the z-axis displacement can be comparable to, or greater than, the in-plane displacement. In the images in Figure 5-5 (A), a slice along the long axis of the cell is shown, and the cell has been rendered in 3-D and superimposed to correlate its position with the observed displacements. The colored displacement contours show that larger displacements are concentrated near the top surface of the gel, and that these displacements decay from the top surface through the depth. Comparing the displacement patterns on gels of varying thicknesses, we find that displacements are more localized near the cell body on thinner samples (20 μm), and decay more gradually in thicker samples (80 μm). The decay profiles of individual displacement components as well as the total displacements for substrates of varying thicknesses are displayed as line plots in Figure 5-5 (B). All plots were generated by selecting one position along the thickness cross section of the sample near the leading edge of the migrating cell. This position corresponds to the region of maximum

deformation at a given time point. Displacement decays are also notable in the x-y displacements as a function of distance from the cell, and in some cases, drop off more steeply than the z-component. The total displacement profile at a given time point and slice location can be dominated by either in-plane or normal displacements, demonstrating how force-mediated deformations fluctuate during cell movement. Analysis of the ratios of the magnitudes of the individual components of the 3D displacement vector to the magnitude of the vector itself showed similar values for all three components ($\bar{x} = 0.58 \pm 0.29$, $\bar{y} = 0.43 \pm 0.23$, $\bar{z} = 0.50 \pm 0.32$, for $N = 38$ samples), further demonstrating the importance of measuring displacements in all three dimensions.

It is worth noting that deformation of the substrate can be detected at substantial depths below the top surface of each sample, and that this effect can be especially important for thin gels. For example, the fact that measurable displacements extend throughout more than half the thickness of the 20 μm sample, illustrates the importance of considering film thickness in designing experiments to monitor cellular response. In particular, if the substrate thickness is comparable to the extent of the deformation field, a cell seeded on a soft substrate that is bonded to a substantially stiffer support (e.g., glass), may be able to sense the mechanical constraint of the underlying plate. For the samples shown in Figure 5-5, the maximum extent of deformation as a fraction of the sample thickness decreased from 67% to 23% as the gel thickness increased from 20 to 80 μm .

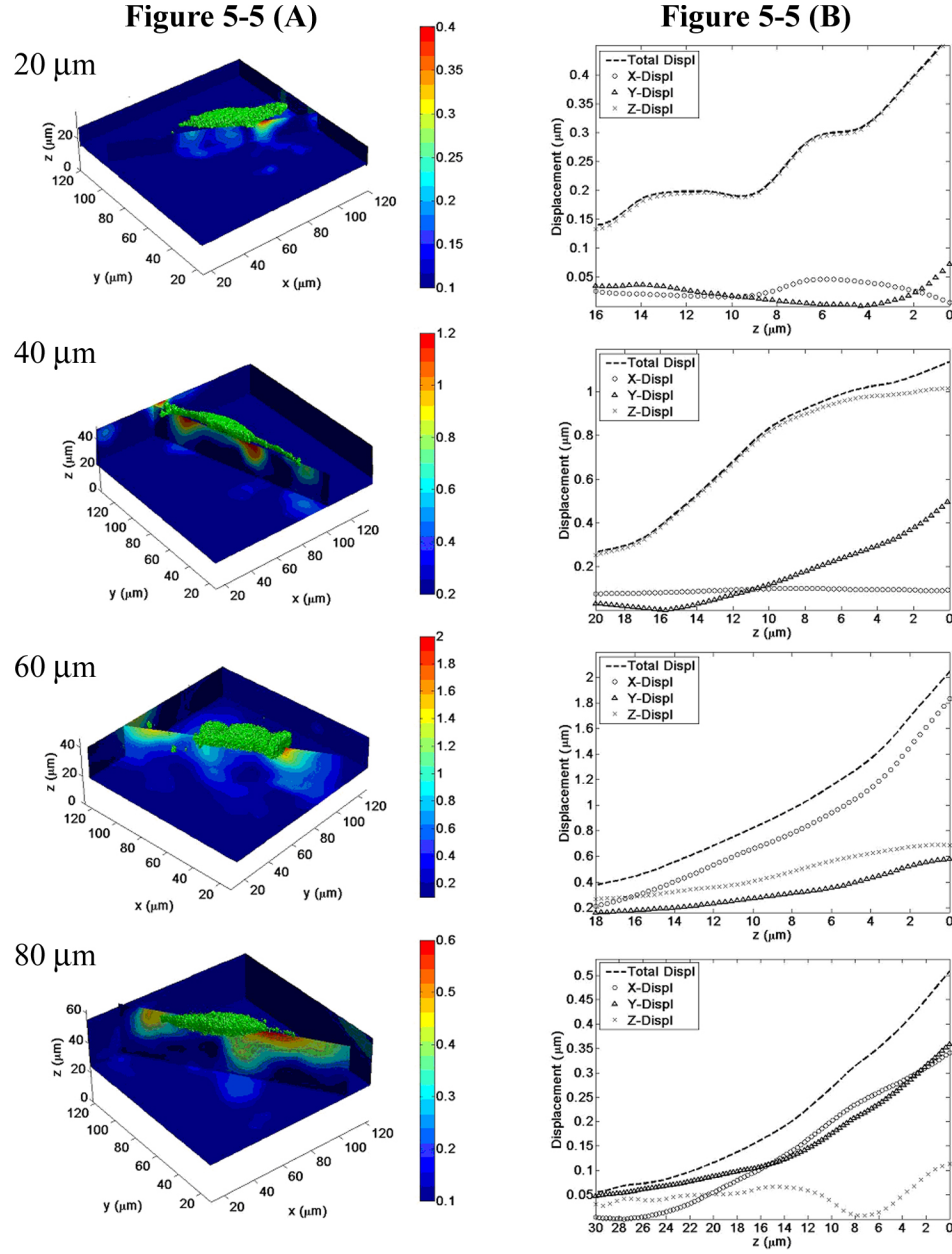


Figure 5-5. Displacement contour slices along the long axis of the cell and corresponding line plots as a function of depth for samples of varying heights. (A) Slices of displacement contours underneath migrating cells show significant deformation in the normal direction that decays along the thickness of the sample. Displacement contours are shown for four samples of increasing thickness, $\sim 20, 40, 60, 80 \mu\text{m}$. The color bar represents the magnitude of the total 3-D displacement vectors (μm), and the cell has been superimposed on the top surface of the sample. The two edges in the image are included to show that there are negligible displacements detected from neighboring cells (contours are dark blue). (B) Corresponding line plots of the total and individual displacement components taken near the leading edges of cells. The x-axis of the plot represents the z -position inside the gel with the origin of the x-axis representing the top surface of the gel.

5.4.4 *Analysis of cellular traction forces in 3D: time evolution of force components*

Comparing series of confocal stacks affords insight into the time evolution of the displacement and traction profiles produced during cell migration. A planar slice through the top surface of the sample shows how the pattern of displacements changes as a cell moves along the substrate surface (Figure 5-6). The set of images in Figure 5-6 (A) represents 3-D data collapsed into 2-D images, and four successive images of this type are displayed for a 140-minute time course of cell migration. The middle panel of parallel images (Figure 5-6 (B)) shows the total displacements (3-D) of the surface plane as colored contours, while the vectors indicate only in-plane (2-D) displacements. These displacements are then transformed into traction forces in the last panel of complementary images (Figure 5-6 (C)) using the experimentally determined displacement field and material properties.

A polarized cell extending processes in the form of a leading edge generates localized, contractile stresses that change as it propels itself forward (Figure 5-6 (C), 35 min to 70 min). Corresponding retraction forces are observed near the rear of the cell, and corroborate the observation that when cells migrate on substrates of intermediate and high adhesiveness, a portion of their trailing edge can be fractured, leaving behind adhesion receptors (e.g., integrins) on the surface [23, 24]. A similar range of displacement values observed on samples of varying mechanical properties suggests that under typical culturing conditions, cells maintain relatively constant levels of displacement (independent of modulus) within the range of material properties considered here. In accordance with previous studies, the calculated forces on more rigid

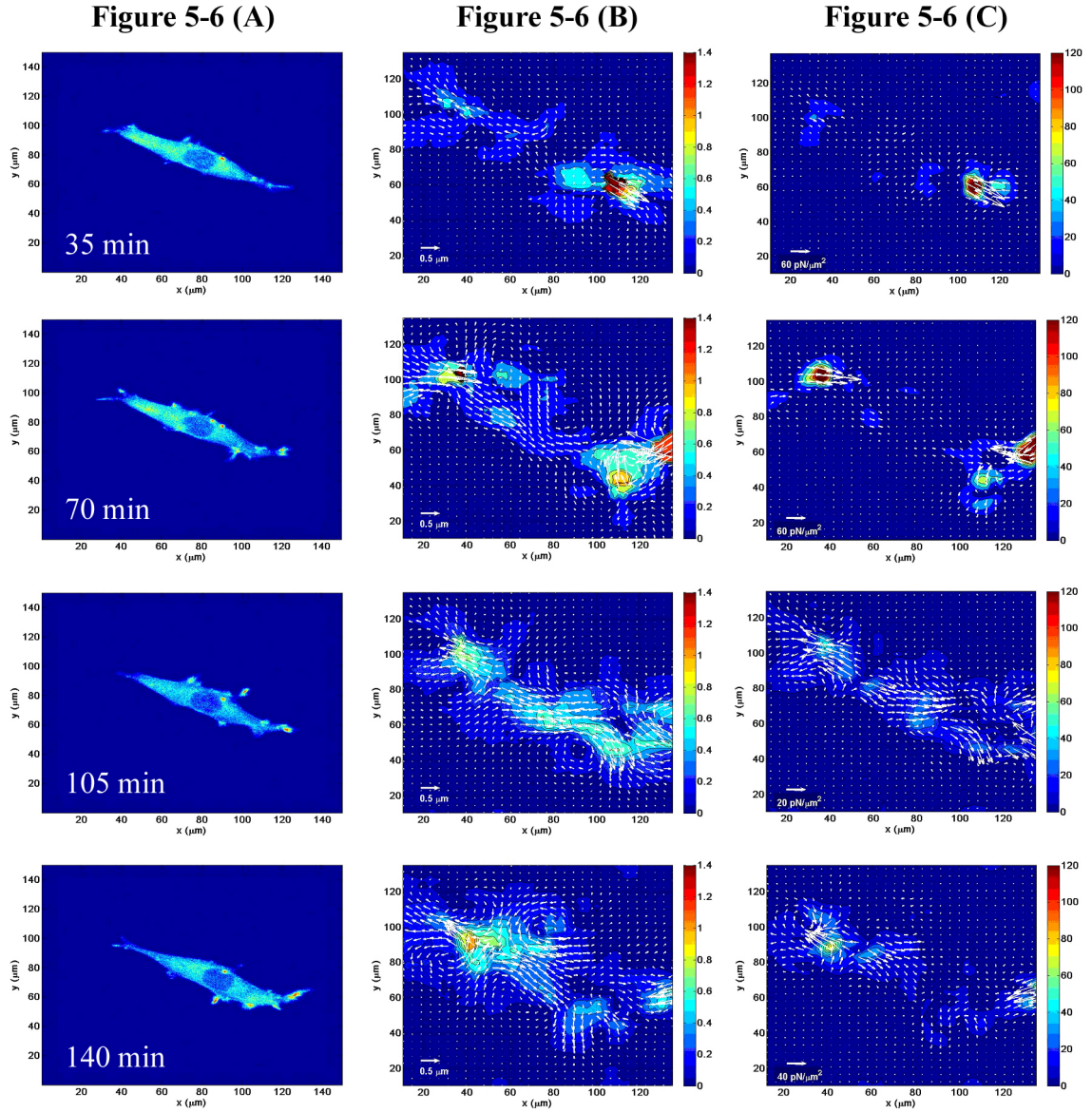


Figure 5-6. Time evolution of displacement and traction force contours during cell migration for a single cell. (A) A series of four successive confocal images recorded during time-lapse imaging experiment. The images shown were captured every 35 minutes for a total of 140 minutes. (B) Consecutive displacement contours and vectors resulting from the motile cell shown in Figure 5-6 (A). The color bar represents the magnitude of the 3-D displacement vectors, and the arrows represent the in-plane displacement vectors. (C) Complementary traction force results calculated directly from displacements in Figure 5-6 (B). The scale bar represents 3-D traction forces in $\text{pN}/\mu\text{m}^2$, and the arrows represent the in-plane forces.

samples are greater than those on softer ones [25]. Additionally, the regions with the highest traction forces are also the regions with the largest measured displacements. It is important to note that the magnitudes of the forces determined here lie within the range reported for fibroblasts [10, 15], and that these measurements only present the distribution of cellular forces that occur during movement and thus cannot be directly compared to a total detachment force.

At certain time points (e.g., see Figure 5-6 (C): 105–140 min) significant displacements are measurable beneath the cell body near the nucleus, suggesting that a large portion of the cell's contact area participates in force exchange with the substrate. Examination of the contribution of each force component during cell migration showed notable in-plane forces on the ventral surface of the cell that likely indicate frictional forces. Further experiments will be needed to define more clearly the origins of these displacements.

5.4.5 *Analysis of cellular traction forces in 3D: “push-pull” phenomena*

In many instances, a cell can be seen pulling the matrix from behind while simultaneously pushing a different region of the matrix forward near its leading edge. This new, “push-pull,” aspect of cell migration was detected in the normal displacement profiles of monitored cells (Figure 5-7 (A)). 3-D displacement vectors superimposed on displacement contour plots show how this behavior can be seen as the cell deforms the material relative to the surface (Figure 5-7 (B)). The local “pulling” force calculated underneath the rear portion of the cell shown in Figure 5-7 (B) (region I, area ca. $7 \mu\text{m}^2$) is approximately 14 nN, and the total force in the entire region (Figure 5-7 (B), region II,

area ca. $16 \mu\text{m}^2$) reaches almost 70 nN. Closer inspection of this particular profile at a later time reveals a wave-like pattern in the material (Figure 5-7 (C) and (D)), indicating a coupling of normal and in-plane displacements.

A potential macroscopic analog of this type of 3-D push-pull movement is the rapid surface attachment and detachment of a single seta on a gecko's toe. The toes of these lizards have attracted interest because they can support significant adhesion (normal) and frictional forces (in-plane) that allow the gecko to scale almost any vertical surface [26]. During toe attachment or approach to a surface, individual spatula pads that comprise a seta adhere to the substrate in a near-parallel manner (rolling), followed by gripping of the gecko's toes. In order for the toes to be detached to allow forward movement, a lever-like action pulls the seta upward such that individual spatula pads are peeled from the surface from the rear inward [26]. This peeling mechanism gradually changes the pulling angles between the seta and the surface thereby decreasing the effective van der Waals interaction. Comparing this "rolling and gripping" mechanism of the gecko to the z-displacement patterns observed during cell migration, we find that, subsequent to leading edge extension, the cell must gradually detach its trailing edge in order to move forward. Similar to the lever-action of the gecko, the cell exerts an upward force resulting in an upward displacement to detach the rear.

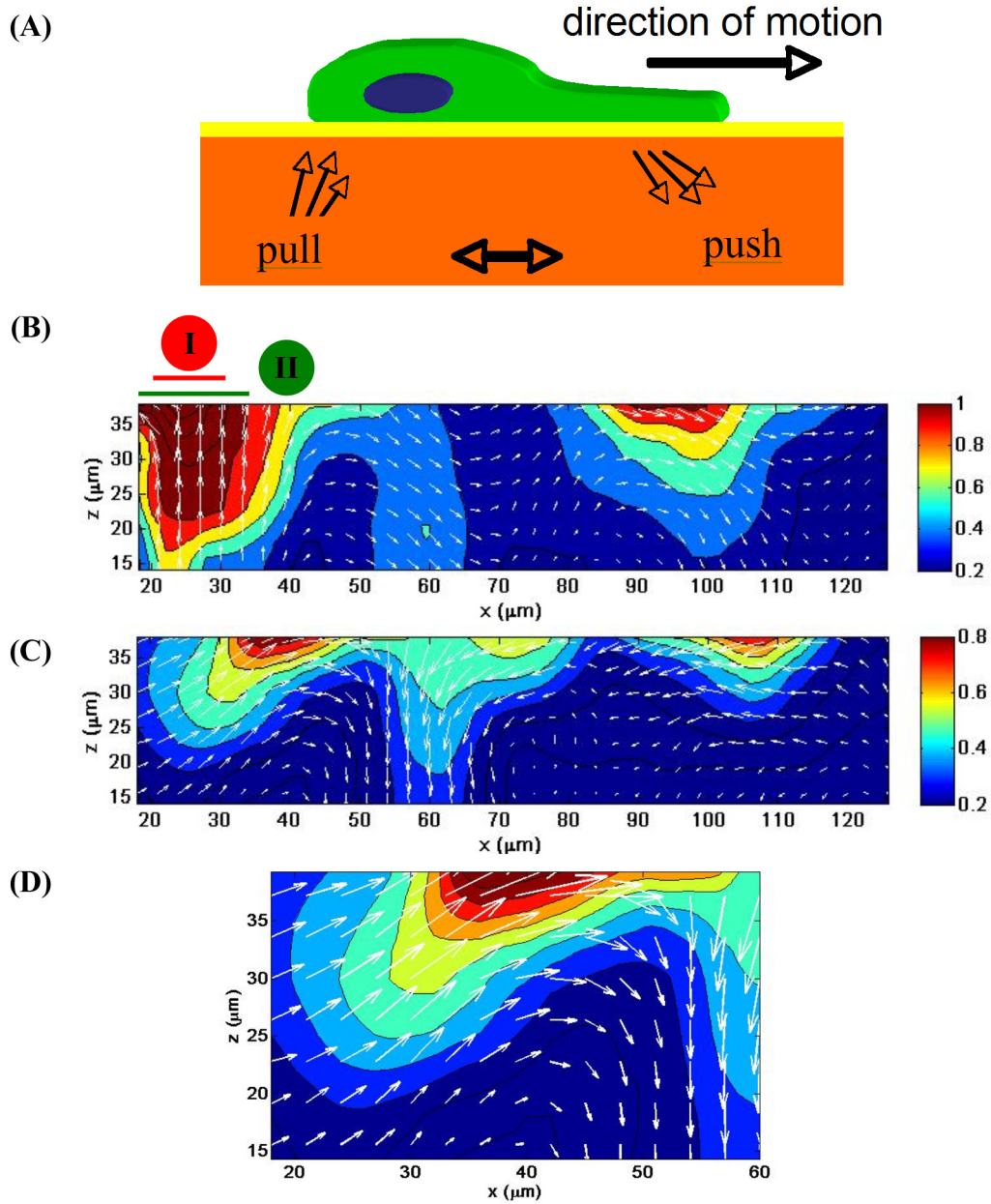
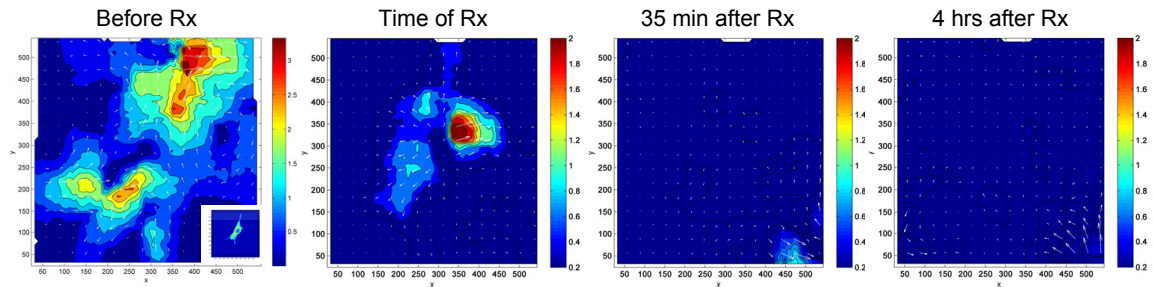


Figure 5-7. 3-D “push-pull” phenomenon observed in the z-plane displacement profiles of tracked cells. (A) Schematic of a cell simultaneously pushing and pulling the underlying material during migration corresponding to a “rolling and gripping” mechanism. (B) The displacement profile in the z-plane illustrates the push-pull hypothesis at $t = 35$ minutes. A strong pull upwards near the rear of the cell coordinates with the forward motion of the cell and the pushing of the material near the front of the cell. (C) At $t = 70$ minutes, the change in the displacement pattern shows the dynamic nature of the 3-D “push-pull” mechanism, and a magnified view (D) shows a complex pattern that incorporates both normal and in-plane displacements. The color bar represents the magnitude of the total 3-D displacement vectors, and the arrows represent the displacement vectors in the x-z plane.

5.4.6 Traction force inhibition with blebbistatin

Confirmation of the cellular origins of the measured displacements was accomplished by replicating time-lapse experiments followed by treatment with blebbistatin. Addition of this myosin-II-specific blocker [27] resulted in a gradual inhibition of cell-generated displacements, showing that the localized matrix deformations observed were caused by contraction of actin bundles by myosin-II activity (Figure 5-8).

(A)



(B)

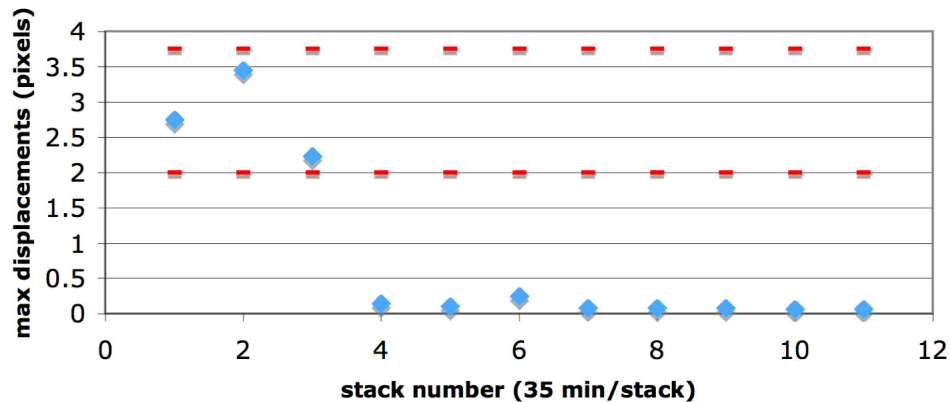


Figure 5-8. Traction force inhibition using blebbistatin: (A) Superimposed planar images of cells and displacement contours before and after treatment (Rx) with blebbistatin; (B) Plot of average maximum displacements measured before and after blebbistatin treatment. Confocal stacks were obtained every 35 minutes.

5.5 Conclusions

This report introduces a new method to track and quantify cellular traction forces in 3-D by using LSCM and DVC. This novel combination of techniques allows dynamic interrogation of the complex process of cell migration and yields further insight into the interactions of cells with their extracellular environments. The approach can be used for local force-mapping of focal adhesions and analysis of the interplay of competing force-fields generated by neighboring cells and sheets of cells. Furthermore, the technique can be extended to elucidate changes in traction forces due to malignant transformation, force profiles of encapsulated cells, and the effect of soluble factors on force production.

5.6 References

1. Discher, D.E., P. Janmey, and Y.L. Wang, *Tissue cells feel and respond to the stiffness of their substrate*. Science, 2005. **310**(5751): 1139-1143.
2. Engler, A.J., et al., *Matrix elasticity directs stem cell lineage specification*. Cell, 2006. **126**(4): 677-689.
3. Zaari, N., et al., *Photopolymerization in microfluidic gradient generators: Microscale control of substrate compliance to manipulate cell response*. Advanced Materials, 2004. **16**(23-24): 2133-2137.
4. Pelham, R.J., and Y.L. Wang, *Cell locomotion and focal adhesions are regulated by substrate flexibility*. Proceedings of the National Academy of Sciences of the United States of America, 1997. **94**(25): 13661-13665.
5. Ingber, D.E., *Mechanobiology and diseases of mechanotransduction*. Annals of Medicine, 2003. **35**(8): 564-577.

6. von Wichert, G., and M.P. Sheetz, *Mechanisms of disease: The biophysical interpretation of the ECM affects physiological and pathophysiological cellular behavior*. Zeitschrift Fur Gastroenterologie, 2005. **43**(12): 1329-1336.
7. Koo, L.Y., et al., *Co-regulation of cell adhesion by nanoscale RGD organization and mechanical stimulus*. Journal of Cell Science, 2002. **115**(7): 1423-1433.
8. Maskarinec, S.A., and D.A. Tirrell, *Protein engineering approaches to biomaterials design*. Current Opinion in Biotechnology, 2005. **16**(4): 422-426.
9. Wang, J.H.C., and J.S. Lin, *Cell traction force and measurement methods*. Biomechanics and Modeling in Mechanobiology, 2007. **6**: 361-371.
10. Dembo, M., and Y.L. Wang, *Stresses at the cell-to-substrate interface during locomotion of fibroblasts*. Biophysical Journal, 1999. **76**(4): 2307-2316.
11. Roy, P., et al., *Microscope-based techniques to study cell adhesion and migration*. Nature Cell Biology, 2002. **4**(4): E91-E96.
12. Tan, J.L., et al., *Cells lying on a bed of microneedles: An approach to isolate mechanical force*. Proceedings of the National Academy of Sciences of the United States of America, 2003. **100**(4): 1484-1489.
13. Galbraith, C.G., K.M. Yamada, and M.P. Sheetz, *The relationship between force and focal complex development*. Journal of Cell Biology, 2002. **159**(4): 695-705.
14. Harris, A.K., P. Wild, and D. Stopak, *Silicone-Rubber Substrata – New Wrinkle in the Study of Cell Locomotion*. Science, 1980. **208**(4440): 177-179.
15. Balaban, N.Q., et al., *Force and focal adhesion assembly: a close relationship studied using elastic micropatterned substrates*. Nature Cell Biology, 2001. **3**(5): 466-472.

16. Franck, C., et al., *Three-dimensional full-field measurements of large deformations in soft materials using confocal microscopy and digital volume correlation*. Experimental Mechanics, 2007. **47**(3): 427-438.
17. Lombardi, M.L., et al., *Traction force microscopy in Dictyostelium reveals distinct roles for myosin II motor and actin-crosslinking activity in polarized cell movement*. Journal of Cell Science, 2007. **120**(9): 1624-1634.
18. Stephens, D.J., and V.J. Allan, *Light microscopy techniques for live cell Imaging*. Science, 2003. **300**(5616): 82-86.
19. Levental, I., P.C. Georges, and P.A. Janmey, *Soft biological materials and their impact on cell function*. Soft Matter, 2007. **3**(3): 299-306.
20. Sabass, B., et al., *High resolution traction force microscopy based on experimental and computational advances*. Biophysical Journal, 2008. **94**: 207-220.
21. Beningo, K.A., et al., *Traction forces of fibroblasts are regulated by the Rho-dependent kinase but not by the myosin light chain kinase*. Archives of Biochemistry and Biophysics, 2006. **456**(2): 224-231.
22. Bhadriraju, K., et al., *Activation of ROCK by RhoA is regulated by cell adhesion, shape, and cytoskeletal tension*. Experimental Cell Research, 2007. **313**: 3616-3623.
23. Palecek, S.P., et al., *Physical and biochemical regulation of integrin release during rear detachment of migrating cells*. Journal of Cell Science, 1998. **111**: 929-940.

24. Cox, E.A., and A. Huttenlocher, *Regulation of integrin-mediated adhesion during cell migration*. Microscopy Research and Technique, 1998. **43**(5): 412-419.
25. Vogel, V., and M. Sheetz, *Local force and geometry sensing regulate cell functions*. Nature Reviews Molecular Cell Biology, 2006. **7**(4): 265-275.
26. Tian, Y., et al., *Adhesion and friction in gecko toe attachment and detachment*. Proceedings of the National Academy of Sciences of the United States of America, 2006. **103**(51): 19320-19325.
27. Kovacs, M., et al., *Mechanism of blebbistatin inhibition of myosin II*. Journal of Biological Chemistry, 2004. **279**(34): 35557-35563.

6 Conclusion

6.1 Summary

A set of photoreactive artificial extracellular matrix (aECM) proteins was engineered to serve as novel biomaterials for the investigation of cell-material interactions. These proteins consist of a cell-binding domain from fibronectin to promote cell attachment and elastin-like repeats for elastomeric behavior. A phenylalanine residue introduced into the elastin backbone enables the incorporation of the photoreactive non-canonical amino acid, *para*-azidophenylalanine (pN_3Phe), into proteins when expressed in a bacterial host containing a mutant phenylalanyl-tRNA synthetase [1]. Photocrosslinking of proteins into films was achieved by irradiation at 365 nm, and the mechanical properties of the protein films could be tuned by altering the irradiation dosage or the incorporation level of pN_3Phe in the proteins.

Rat-1 fibroblast cells recognize specifically the RGD cell-binding domain within the protein when deposited on adsorbed and photocrosslinked protein films. Photolithographic techniques were used to generate protein patterns to serve as a template for cell adhesion, and the resulting cell patterns were stable for several hours. An initial examination of the transcriptomic profiles of Rat-1 fibroblasts deposited on aECM proteins compared to fibronectin was achieved using mRNA microarrays. Preliminary BONCAT (bio-orthogonal noncanonical amino acid tagging) results demonstrate that proteins involved in focal adhesion formation are newly synthesized in cells when seeded on fibronectin [2, 3].

A new method for the quantification and tracking of cell-mediated displacements of the extracellular matrix was achieved through the use of time-lapse laser scanning confocal microscopy and digital volume correlation [4]. It was observed that cells explore

their extracellular microenvironment by generating displacements in all three spatial dimensions. The measured displacements were found to be independent of the elastic modulus (range: 1–10 kPa) of the underlying material. However, the direction and magnitude of the displacement components fluctuated significantly during cell migration, illustrating the dynamic nature in which the cell investigates its surroundings. Analysis of the displacement profile of migrating cells also showed that cells simultaneously “push” and “pull” the underlying matrix during locomotion.

6.2 Future Directions

The modular nature of these aECM proteins offers a facile method for the construction of novel biomaterials with customized cell-binding domains for specific biomedical applications. Currently, other aECM variants have been investigated as artificial corneal onlays [5] and for promoting neurorestoration in the brain [6]. Future approaches may include directing stem cell differentiation by incorporating epitopes from growth factors or other extracellular matrix molecules as well as targeting skin regeneration by promoting keratinocyte proliferation. Microfabrication techniques such as microstamping and microfluidics can be employed to create patterns of various aECM proteins to promote the formation of organized heterotypic cell populations and hierarchical tissue-like structures.

The characterization of cellular response to aECM proteins as described in Chapter 4 can be extended to examine the effect of how modifying the cell binding domain density (mixtures of RGD and RDG) and mechanical properties of protein films alters mRNA transcript levels and protein expression. Future work may also investigate

transcription levels and newly synthesized proteins after longer incubation periods. This analysis can be expanded to include a variety of cell types in order to test whether differences between human and murine cell lines can be detected, an important consideration in translating these materials from animal studies into the clinic. BONCAT can also be used to investigate more complex biological processes such as host-pathogen interactions as well as stem cell differentiation.

Three-dimensional traction force microscopy can be used to correlate force generation with many cellular processes including malignant transformation and cell clustering. Another application of this technology would include monitoring the changes in force generation during leukocyte extravasation [7]. During this process, cells must adhere to a surface and then migrate into a three-dimensional interstitial space. This could be modeled *in vitro* by creating a gradient of soluble factors within a three-dimensional matrix composed of collagen or fibrin. Such an experiment would offer unprecedented insights into cellular behavior by enabling dynamic tracking of the pattern of cellular force generation from two dimensions into three dimensions. This method can also be used to quantify individual nascent and maturing focal adhesions during cell spreading.

6.3 References

1. Kast, P., and H. Hennecke, *Amino-Acid Substrate-Specificity of Escherichia-Coli Phenylalanyl-Transfer RNA-Synthetase Altered by Distinct Mutations*. Journal of Molecular Biology, 1991. **222**(1): 99-124.
2. Dieterich, D.C., et al., *Selective identification of newly synthesized proteins in mammalian cells using bioorthogonal noncanonical amino acid tagging*

- (*BONCAT*). Proceedings of the National Academy of Sciences of the United States of America, 2006. **103**(25): 9482-9487.
3. Dieterich, D.C., et al., *Labeling, detection and identification of newly synthesized proteomes with bioorthogonal non-canonical amino-acid tagging*. Nature Protocols, 2007. **2**: 532-540.
 4. Franck, C., et al., *Three-dimensional full-field measurements of large deformations in soft materials using confocal microscopy and digital volume correlation*. Experimental Mechanics, 2007. **47**(3): 427-438.
 5. Nowatzki, P.J., *Characterization of crosslinked artificial protein films*, PhD Thesis, 2006, California Institute of Technology.
 6. Liu, C.Y., M.L.J. Apuzzo, and D.A. Tirrell, *Engineering of the extracellular matrix: Working toward neural stem cell programming and neurorestoration - Concept and progress report*. Neurosurgery, 2003. **52**(5): 1154-1165.
 7. Ebnet, K., and D. Vestweber, *Molecular mechanisms that control leukocyte extravasation: the selectins and the chemokines*. Histochemistry and Cell Biology, 1999. **112**(1): 1-23.

Appendix A

Reproduced with permission from:

Nowatzki, P.J., Franck, C., Maskarinec, S.A., Ravichandran, G., and D.A. Tirrell.

Mechanically Tunable Thin Films of Photosensitive Artificial Proteins: Preparation and Characterization by Nanoindentation. Macromolecules, 2008. **41(5)**: 1839-1845.

Copyright 2008 American Chemical Society

Abstract

Thin films of controlled elastic modulus were made by photocrosslinking artificial extracellular matrix (aECM) proteins containing the photosensitive amino acid *para*-azidophenylalanine (pN_3Phe). The elastic moduli of the films were calculated from nanoindentation data collected by atomic force microscopy (AFM) using a thin-film Hertz model. The modulus was shown to be tunable in the range 0.3–1.0 MPa either by controlling the irradiation time or by varying the level of pN_3Phe in the protein. Tensile measurements on bulk films of the same proteins and finite-element simulation of the indentation process agreed with the thin-film modulus measurements from AFM. Substrates characterized by spatial variation in elastic modulus were created by local control of the irradiation time.

A.1 Introduction

Cellular interactions with the surrounding matrix play defining roles in biological processes ranging from normal tissue function to morphogenesis, immunity, wound healing, and tumor metastasis. The realization that substrate mechanical properties strongly influence cell behavior is comparatively recent and has stimulated considerable interest [1]. Substrate stiffness has been shown to affect cell adhesion [2, 3], morphology [2, 4, 5], traction forces and migration rate [2, 6, 7], growth [8], and differentiation [3, 9-11].

Cell culture substrates with adjustable mechanical properties have become essential tools for the study of cell-matrix interactions. The stiffness-dependent cell behavior reported to date has been examined most frequently on synthetic gels such as polyacrylamide [2, 6, 12]. Because biological and mechanical signals are often interdependent [1, 13], some investigators have chosen substrates (e.g., collagen-coated gels) that mimic more closely the natural extracellular matrix [3, 8]. Additional advantages accrue from varying mechanical properties on a single substrate, in that many sets of culture conditions can be probed at once, reducing the experimental variability that arises from lot-to-lot variation in the behavior of cultured cells. Moreover, films of spatially varying elastic modulus allow the examination of cell behavior at mechanical interfaces [6], and elastic modulus gradients allow the study of mechanotaxis or durotaxis [7, 14, 15].

Here we describe the use of photosensitive artificial proteins to make substrates on which the interrelated effects of elastic modulus and extracellular matrix biology can be studied directly. These proteins are intended for use as implantable biomaterials, and

are designed to mimic key features of the extracellular matrix [16-19]. The design (Figure A-1) includes cell-binding domains periodically spaced between elastin-like repeating elements. The CS5 cell-binding domain, derived from human fibronectin, enables attachment of cells that express the $\alpha_4\beta_1$ integrin adhesion receptor [20]. The origin of the elasticity of the protein is the repeating pentapeptide VPGVG (Val-Pro-Gly-Val-Gly), derived from mammalian elastin and shown by Urry and others to confer mechanical properties appropriate for soft tissue engineering and regenerative medicine [21].

MMASMTGGQQMGRKTHHHHHHMG{LDGEEIQIGHIPREDVDYHLYPG
 [(VPGVG)₂(VPGFG)(VPGVG)₂]₅LP}₃LE

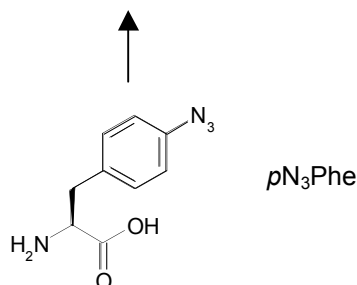


Figure A-1. Amino acid sequence of the artificial extracellular matrix protein examined in this work. The cell-binding sequence CS5 is underlined. Proteins containing the photosensitive amino acid para-azidophenylalanine are designated aE-*pN₃Phe*.

The phenylalanine (Phe) sites encoded within the elastin-like domains of the protein serve as sites for incorporation of the non-canonical amino acid *para*-azidophenylalanine (*pN₃Phe*, Figure A-1). Incorporation of *pN₃Phe* into recombinant proteins is accomplished by using a bacterial expression host that harbors a mutant phenylalanyl-tRNA synthetase (PheRS) with an enlarged binding pocket [22, 23]. Upon photolysis, *pN₃Phe* generates a reactive nitrene intermediate that yields non-specific

crosslinks to surrounding protein molecules. Varying the concentration of pN_3Phe in the expression medium controls the extent of incorporation of the photosensitive amino acid into the protein, and ultimately determines the crosslink density and elastic modulus of the irradiated protein film. We recently reported photochemical patterning of similar proteins (and adherent cells) on solid substrates [24]. Here we describe detailed mechanical characterization of thin photocrosslinked protein films and demonstrate the preparation of step-gradients of mechanical properties within a single film.

Mechanical properties of thin, substrate-bound films are typically measured by nanoindentation, and atomic force microscopy (AFM)-based nanoindentation in particular offers significant advantages in spatial and force resolution over conventional nanoindenters. The method is especially attractive for analyzing soft samples and materials whose elastic modulus varies over short length scales [25-27]. Here AFM nanoindentation with a microspherical tip (600 nm diameter) was used to obtain accurate measurements of the elastic moduli of thin photocrosslinked protein films [11, 28, 29]. The use of a spherical tip is important, in that it allows a spherical indentation model to be correctly applied; the classical Hertz spherical model is known to cause distortions when used to analyze AFM data collected with conventional sharp, pyramidal or conical tips [30]. A film-height dependent physical model [31] accounts for the mechanical coupling of the film to its underlying substrate, another known source of distortion in AFM nanoindentation [32, 33]. Bulk tensile tests of the same materials confirm the validity of the nanoindentation analysis.

Finite element simulations of the indentations were also performed to verify the modulus calculations and to explore the possibility of determining a more sophisticated

mechanical material model from the AFM data. While the linear elasticity model [31] accurately characterizes the Young's (elastic) moduli of the films described herein, the finite element analysis is appropriate for characterization of thinner films undergoing large deformations due to higher-strain indentation or certain tip geometries.

A.2 Materials and Methods

A.2.1 Protein aE-*pN₃Phe*

The amino acid sequence of the photosensitive artificial extracellular protein, aE-*pN₃Phe*, is shown in Figure A-1. aE-*pN₃Phe* is made biosynthetically in a Phe-auxotrophic strain of *Escherichia coli* outfitted with a plasmid bearing genes coding for both the protein and the Ala294Gly mutant of the *E. coli* phenylalanyl-tRNA synthetase (PheRS) [34]. Use of the mutant synthetase allows incorporation of *pN₃Phe* (Bachem) into recombinant proteins in place of Phe [23]. Because the relative amounts of Phe and *pN₃Phe* in the protein can be controlled by varying the concentrations of the amino acids in the expression medium, the designation aE-*pN₃Phe* refers to a family of artificial proteins rather than to a single protein.

The expression and purification of aE-*pN₃Phe* were performed as described previously [24]. To deplete Phe from the expression medium, cells were centrifuged and resuspended in minimal medium lacking Phe and containing *pN₃Phe* 10 minutes after expression was induced. This procedure allows enough time for functional copies of PheRS to be synthesized before Phe is depleted.

The extent of replacement of Phe by *pN₃Phe* was measured by 600 MHz ¹H NMR spectroscopy (Varian) at a protein concentration of 15 mg/mL in DMSO-d₆ (Cambridge Isotope Laboratories) [24]. Phe replacement levels of 28%, 31%, 48%, and 66% were

achieved by using 125, 188, 250, and 250 mg/L, respectively, of pN_3Phe in the culture medium; the corresponding proteins are designated aE-28%- pN_3Phe , etc.

A.2.2 AFM - instrument

Images and force curves were collected on a Park Scientific Instruments AutoProbe M5 atomic force microscope, with accompanying ProScan v1.51b software. Pyramidal-tipped triangular silicon nitride cantilevers with nominal spring constant 0.58 N/m were used for imaging (Veeco DNP-S). A silicon nitride cantilever of the same shape, with an attached 600 nm diameter SiO_2 particle tip (Novascan, Ames, IA), was used to indent samples for collecting force curves. The spring constant of the cantilever was calculated to be 0.37 N/m by indenting against reference cantilevers with predetermined spring constants of 1.00 N/m and 0.125 N/m (Veeco CLFC). Here, $k_{test}/k_{ref} = (\delta_{tot} - \delta_{test})/(\delta_{test} \cos\theta)$, where k_{test} and k_{ref} are the spring constants of the test and reference cantilevers, δ_{tot} and δ_{test} are slopes of the force-distance curves when the test cantilever is indented against a rigid surface and against the free end of a reference cantilever, respectively, and θ is the angle between the cantilevers (15°). A glass slide was glued to the back of the cantilever mount so that the cantilever and sample could be submerged in water.

A.2.3 Bulk protein films

aE- pN_3Phe (4 mg) was dissolved in dimethylsulfoxide (40 μ L, Mallinckrodt). The solution was spread to cover an area ca. 1.5 cm \times 1 cm on a poly(methyl methacrylate) surface, and the solvent was evaporated at 50°C overnight. The resulting films were ca. 20 μ m thick (dry). After photocrosslinking (*vide infra*), uniaxial tension tests were

performed at 22°C on an Instron 5542 Materials Testing System outfitted with a 0.5 N load cell and modified to contain the sample in a water bath. The nominal strain rate was 0.1 per minute [35]; at this rate viscoelastic effects are negligible.

A.2.4 Thin protein films

All film-making procedures were performed in a cold room (4°C), below the lower critical solution temperature (LCST) [21] of the protein in water. Protein (10 mg) was dissolved in water (100 µL), and the solution was centrifuged (5 min, 16,500g) to remove any aggregates or particles. Protein solution (10 µL) was pipetted onto and spread to cover an unmodified 12 mm glass slide (Hecht-Assistent, Sondheim, Germany). Films were spin-coated (Specialty Coating Systems, Inc. P6204, Indianapolis, IN) at 7,000 rpm for 30 seconds and dried overnight at 4°C. Typical film thickness was ca. 160 nm (dry).

A.2.5 Irradiation of films

Dry protein films were exposed to unfiltered UV light from a high-pressure mercury arc lamp (Oriel Q, 100 watt @ 5 amps, > 20 min warm-up time; measured intensity in irradiation plane = 1.5 mW/mm²). The time required to achieve complete conversion, ca. 300 sec, was determined empirically. Zones of differential crosslinking were prepared on the same substrate by placing an opaque shutter over portions of the film during irradiation. Specifically, a step-gradient of irradiation times (0, 12, 20, 30, 50, 80, 120, 180, and 300 sec) was made across a 12 mm slide by manually repositioning the shutter between exposures.

Slides were agitated in excess water at 4°C to remove any soluble protein. Un-irradiated protein, or protein irradiated for 12 sec or less, was completely removed during this rinsing process as evidenced by AFM imaging. No delamination of irradiated films from their glass substrates was observed.

A.2.6 AFM – film thickness

The tip of a pair of fine forceps was dragged lightly across the surface of the protein film, tearing away the protein along the scratch and revealing the underlying glass substrate. The edge of this scratch was imaged by AFM both dry and under water; the thickness of the film is apparent from the scan (see Figure A-2). The surface revealed by the scratch was confirmed to be glass, based on its smoothness and linear force profile when indented. The protein film thickness was calculated by averaging the height measurements at many ($n \geq 16$) points on the film, using the revealed glass surface as a baseline.

A.2.7 AFM – indentation force curves

The films and cantilever assembly were submerged in water under ambient conditions. The 600-nm SiO₂ microsphere tip was placed above a spot where the film thickness had been measured (identified visually from the optical microscope image using reference markers on the film) to ensure that the thickness at the point of indentation was known. Force curves were collected; the instrument records z (piezo) displacement, and force, which is the product of measured tip deflection and cantilever spring constant.

The indentation range was set to (-150 nm, +1350 nm) relative to the contact point, effectively limiting the force to ca. 20-30 nN and the strain magnitude to less than 20%. The indent-retract cycle time was 1 sec (tip speed 3 $\mu\text{m}/\text{sec}$). Viscoelastic effects did not appear to be a significant factor at this strain rate (ca. 4 sec^{-1}), as evidenced by the statistical superimposability of force curves collected using 1 sec and 10 sec cycles (strain rate ca. 0.4 sec^{-1}) (Figure A-4).

To assess the uniformity of the films, force curves were evaluated repeatedly at the same spot and at nearby spots spaced 10-20 μm apart. For uniformly irradiated $p\text{N}_3\text{Phe}$ films this procedure was repeated at three distant ($> 1 \text{ mm}$ apart) spots of known height.

A.2.8 Calculation of Young's (elastic) modulus

The Dimitriadis model for indentation of linearly-elastic soft material films of finite height with a spherical indenter was applied to the loading force data [31]. For a support-bonded film with Poisson's ratio of $\nu = 0.5$ (incompressible, a reasonable estimate for both for rubbery networks and biological materials):

$$F = \frac{16E}{9} R^{1/2} \delta^{3/2} [1 + 1.133\chi + 1.283\chi^2 + 0.769\chi^3 + 0.0975\chi^4] \quad (1)$$

The first term of this series is the classical Hertz indentation model, giving the force F as a function of (Young's) elastic modulus E and indentation depth δ using a rigid sphere of radius R . The additional terms correct for the finite height of the film, where χ is given by [31]:

$$\chi = \sqrt{R\delta} / h \quad (2)$$

where h is the thickness of the film. As the film gets thinner, or as the indentation depth increases, the indenting sphere (AFM tip) experiences a higher force than it would for an

infinitely-thick film of the same material, owing to mechanical effects of film confinement to the stiff underlying substrate. The film indentation δ was calculated by subtracting the tip displacement from the total (z) displacement.

The contact point of each force-distance curve, where the indentation and force were set to zero in the analysis, was determined by visual inspection. While this can be difficult in some experiments [31], it is straightforward for the force curves collected here, because we observe a distinct snap-in when the tip touches the surface (see Figure A-3 for examples). The apparent elastic modulus was calculated by evaluating equations (1) and (2) at each recorded force-indentation point between 15 nm and 10% film thickness indentation and averaging over the range. Below 15 nm, the scatter in the data is magnified in the calculations and distortions are common; the 10% maximum indentation constrains the data to the near-linear response range [31]. In this strain range, the finite-height correction factor was as large as 1.78 ($\chi = 0.395$) for the films analyzed here.

A.2.9 Finite element simulation

Simulations of the nanoindentation process were conducted by using the commercial finite element software, *ABAQUS* (ABAQUS, Inc., Providence, RI). The geometries of the indenter and the film were discretized by using 2D axisymmetric elements (*CAX4R*) and the known protein film height and indenting spherical tip geometry ($R = 300$ nm). From tensile data collected for bulk samples of aE-*pN*₃Phe, material model parameters for each material were calculated and entered into the simulation. Various hyperelastic material models describing the large strain material

behavior (e.g., Neo-Hookean, Mooney-Rivlin, etc.) were evaluated. The Yeoh model [36] was found to best describe the material response of aE- pN_3 Phe as determined through numerous uniaxial tension and compression tests. The output of force versus film indentation was compared to the AFM data collected experimentally.

A.3 Results and Discussion

A.3.1 Protein production and purification

aE- pN_3 Phe proteins were expressed in a phenylalanine-auxotrophic *E. coli* expression host using a medium shift procedure which allowed controlled replacement of phenylalanine by pN_3 Phe. Cells were grown for several hours in media containing all 20 natural amino acids, washed and transferred to minimal media containing 19 amino acids and lacking phenylalanine. Production of the mutant PheRS during the initial growth period provides the cellular machinery needed for insertion of pN_3 Phe into recombinant proteins. Target proteins were collected from harvested cells and separated from contaminant proteins through a series of temperature-shift centrifugation cycles [24], and protein purity was monitored by denaturing gel electrophoresis. Titrating the amount of pN_3 Phe in the expression medium generated artificial proteins containing controlled levels of incorporation of the photosensitive amino acid (Table A-1).

Table A-1. Expression conditions and protein yields

protein	pN_3 Phe added to medium (mg/L)	% replacement of Phe by pN_3 Phe	protein yield (mg protein/liter of culture)
aE-66%- pN_3 Phe	250	66%	66
aE-48%- pN_3 Phe	250	48%	35
aE-31%- pN_3 Phe	188	31%	76
aE-28%- pN_3 Phe	125	28%	66

A.3.2 Thin films

Spin-coated thin films of aE- pN_3 Phe proteins appeared smooth (RMS roughness = 1.3 nm, versus 0.9 nm for the revealed glass) when imaged by AFM (Figure A-2). Film thickness was uniform over the surface of each 12 mm diameter glass substrate, varying no more than $\pm 11\%$ from the average. Local thickness was much more uniform, with $< 2\%$ variation in a 30 μm scan. The protein films had average hydrated thicknesses between 206 and 368 nm, except for two films ca. 1500 nm thick, which were made by using a higher concentration of aE-66%- pN_3 Phe (Table A-2). The average ratio of wet-to-dry film thickness was 1.80, corresponding to a polymer volume fraction of 0.56 in the hydrated films. We observed little variation in the polymer volume fraction under the conditions used here.

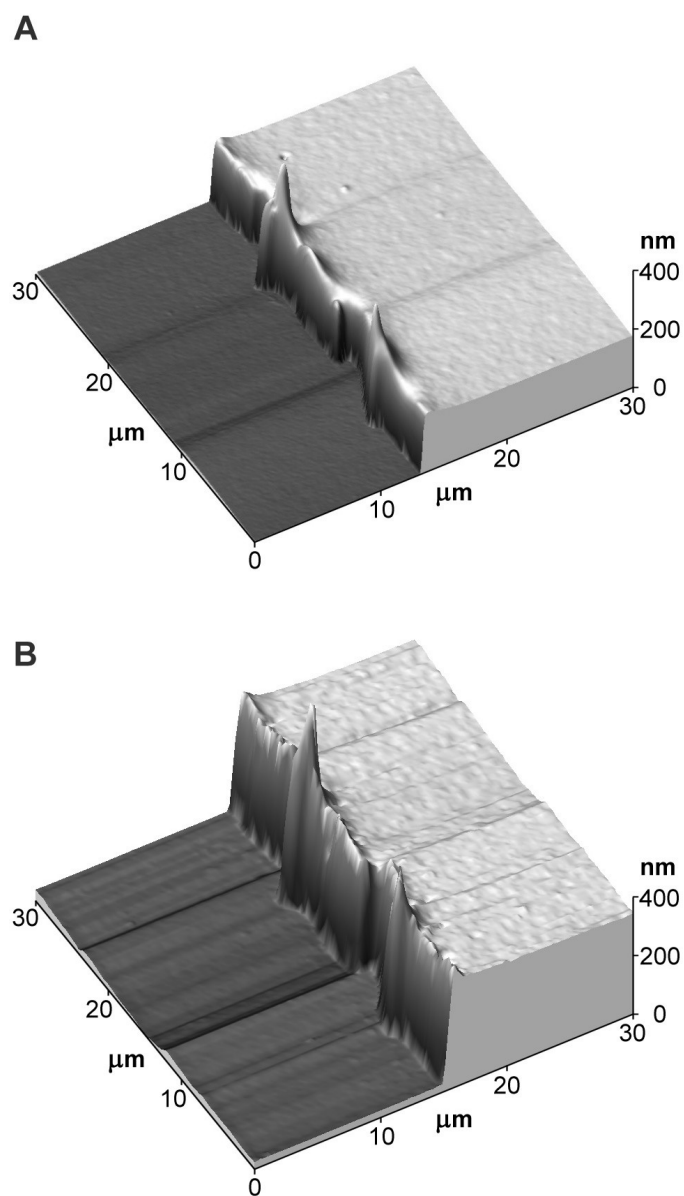


Figure A-2. AFM topography scans of cut edges of an aE-48%-*p*N₃Phe film, dry (A) and in water (B). The spikes at the edge are artifacts of the scratching procedure.

Table A-2. (A) Physical properties of bulk aE-*p*N₃Phe films tested in uniaxial tension (n=2). (B) Physical properties of thin aE-*p*N₃Phe films tested by AFM (n≥6 spots, n≥24 total indents).

A Bulk films		average elastic modulus, E (MPa)	molecular weight between crosslinks, M_c	pN ₃ Phe crosslinking reaction efficiency
protein	thickness (μm)			
aE-66%- <i>p</i> N ₃ Phe	20	1.01 ± 0.07	4300 ± 200	$50 \pm 3\%$
aE-48%- <i>p</i> N ₃ Phe	21	0.52 ± 0.04	7000 ± 400	$42 \pm 2\%$
aE-31%- <i>p</i> N ₃ Phe	19	0.20 ± 0.04	$11,900 \pm 1000$	$39 \pm 3\%$
aE-28%- <i>p</i> N ₃ Phe	20	0.14 ± 0.02	$13,800 \pm 600$	$37 \pm 2\%$

B Films tested by AFM		average elastic modulus, E (MPa)	molecular weight between crosslinks, M_c	pN ₃ Phe crosslinking reaction efficiency
protein	average hydrated thickness of each tested film (nm)			
aE-66%- <i>p</i> N ₃ Phe	312, 322, 328, 1682, 1466	0.91 ± 0.16	4900 ± 700	$45 \pm 7\%$
aE-48%- <i>p</i> N ₃ Phe	293, 368	0.44 ± 0.04	7800 ± 400	$38 \pm 2\%$
aE-31%- <i>p</i> N ₃ Phe	223, 252	0.30 ± 0.02	9800 ± 400	$47 \pm 2\%$
aE-28%- <i>p</i> N ₃ Phe	206, 206	0.29 ± 0.03	$10,000 \pm 500$	$51 \pm 3\%$

A.3.3 AFM force curves

Representative loading force-displacement curves are shown in Figure A-3, and exhibit the parabolic shape typical of indentation of soft materials. Since the assembly is submerged in water, the attractive force between the tip and the surface is screened; nevertheless, a distinct snap-in event appears in each force curve, and allows a contact point to be confidently assigned. In cases where snap-in appeared to occur over a few nanometers, the contact point was assigned to the middle of the snap-in rather than the bottom (at minimum force); this procedure was found to give the best reproducibility

between repeated indentations at the same spot. Adhesion forces between the indenter and sample appeared to be negligible during indentation loading, and finite element simulations confirmed this interpretation.

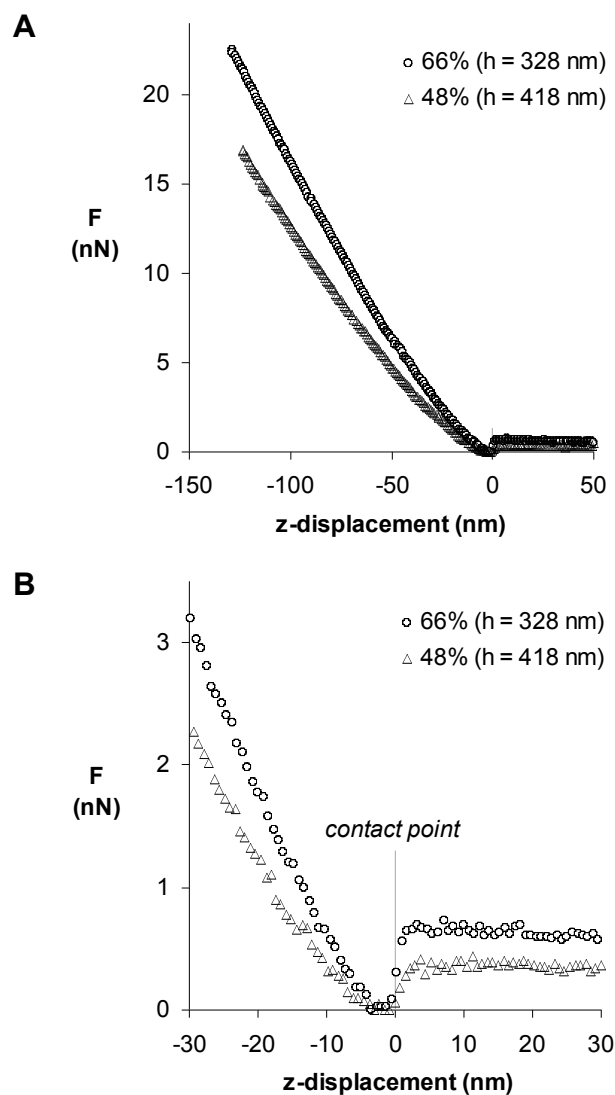


Figure A-3. Representative loading indentation profiles for thin films of aE-66%- pN_3 Phe and aE-48%- pN_3 Phe, showing force versus indentation depth (z -displacement). (A) shows the entire profiles; (B) is magnified to show the contact point assignment.

When the strain rate was reduced by a factor of 10 (from a 1 sec indentation cycle, strain rate ca. 4 sec^{-1}), the resulting force curves appeared indistinguishable from the originals, indicating that viscoelastic effects did not significantly influence the results (Figure A-4) in the range of loading rates considered here (0.4 to 4 sec^{-1}). Faster indentation cycles allow increased throughput and minimize the deleterious effects of sensor drift.

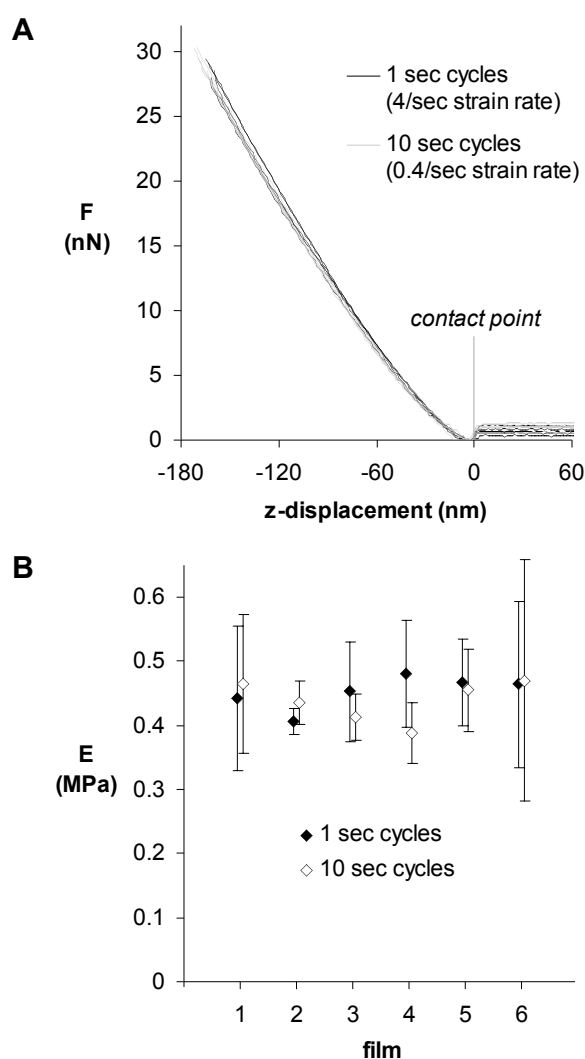


Figure A-4. (A) Superimposed force profiles for multiple indentations of a single aE-48%-pN₃Phe film for 1 sec and 10 sec indent cycles. (B) Calculated Young's modulus for 1 sec and 10 sec indentation cycles on five different aE-48%-pN₃Phe films.

Repeated indentations (up to 100) of the same spot did not cause any change in the force-displacement curves, likely because the hydrated protein films are highly elastic (albeit nonlinear) and the indentation depth was controlled. When surfaces on which the indentations had been performed were subsequently imaged by AFM, no evidence of indentation was seen on either hydrated or dry films. These results suggest that the collection of force curves did not permanently deform or otherwise alter the mechanical properties of the samples.

A.3.4 Analysis of AFM force curves

Once a force curve is collected, all variables except E in Eqs. (1) and (2) are known, so each point on the force-distance curve can be used to calculate an elastic modulus for the material. If the model describes the system correctly, the calculated modulus should be the same at each indentation depth. The Hertz and Dimitriadis [31] models were evaluated using this criterion for a representative data set (Figure A-5). Because the films were less than a micron in thickness and the indentation depth represented a significant portion of the film height, the Hertz model for infinite-height film was inappropriate for elastic modulus calculation. The effective elastic properties of the protein films were significantly influenced by the underlying glass substrate, as has been observed previously for soft thin films [31, 32]. Because it accounts for finite sample thickness and coupling to a rigid substrate, the Dimitriadis model is able to extract the true elastic modulus of the protein film, thus yielding much more consistent predictions of thin film modulus for each force curve in the indentation depth range of 15 nm to 10% (or more) of the film thickness.

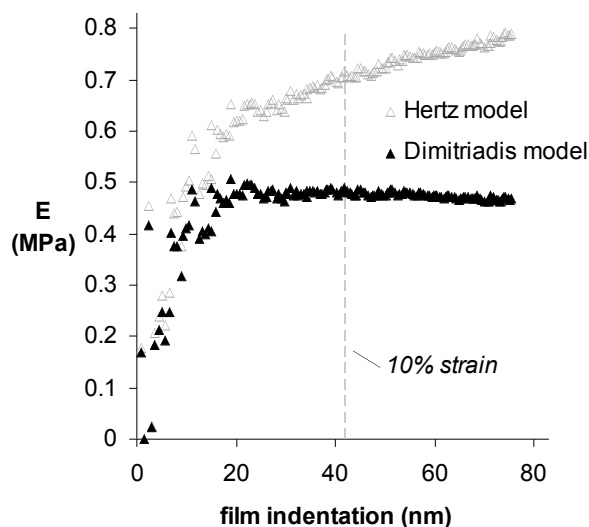


Figure A-5. The elastic modulus (E) calculated at each point in the AFM indentation using Hertz and Dimitriadis models (Eq. 1) is shown for an aE-48%- pN_3 Phe film.

A single value of Young's modulus (E) was assigned to each surface by averaging the model-predicted moduli from 15 nm to 10% strain; the standard deviation in E over this range averaged 3.4% and was <10% for all curves, indicating that the Dimitriadis model gives uniform predictions of E . In general, the model-calculated value of E is sensitive to the placement of the contact point [31], but since contact is observed directly and the sub-15 nm data (recorded forces < 1 nN) are excluded, the fits are robust. Illustrations of the fit of the Dimitriadis model to the experimental AFM data are shown in Figure A-6.

The standard deviation in E from repeated indentation of the same spot ($n=3-4$ indentations, 51 spots) averaged 5.1%. We observed no tendency of the film to change in modulus with repeated indentation. The standard deviation in E between different spots on the same film ($n=3-4$ spots, ≥ 10 μm apart, 13 films) averaged 7.2%, nearly as small as the same-spot variance, indicating that E was uniform over the films. The uniformity of

modulus is important for the application of these films as probes of mechanosensitive cell behavior.

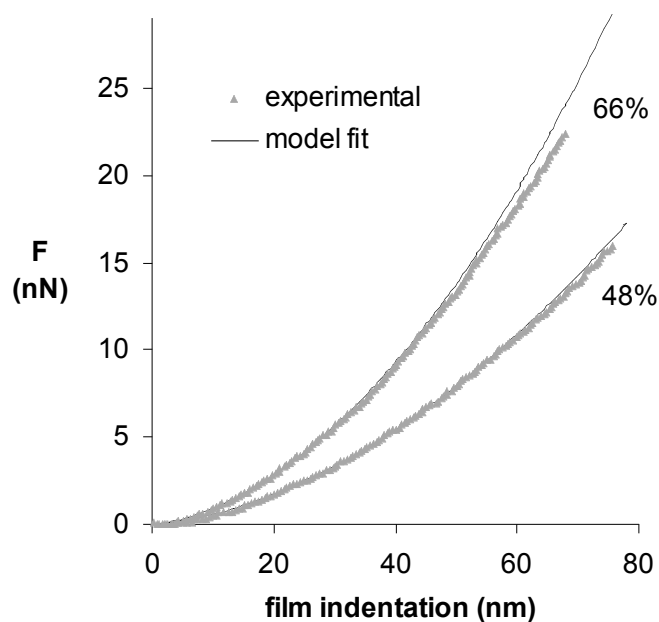


Figure A-6. Experimental AFM indentation data compared to Dimitriadis model (Eq. (1)) fits for thin films of aE-66%-*pN*₃Phe and aE-48%-*pN*₃Phe.

In principle, raw AFM data could be used to estimate film thickness, by iterating the height parameter in Eq. (2) to minimize the variation in predicted modulus over the selected strain range, since over- or underestimated thickness will result in less consistent modulus predictions. For this technique to be applied, the linear model would need to completely describe the material mechanics in the analyzed strain range. However, experimental error makes it likely that decreases in film thickness could be mistaken for increases in elastic modulus, or vice-versa. The determination of modulus is more accurate when the film thickness is known, as it is here.

A.3.5 Finite element simulation of indentation

All bulk tensile data were well-described by a Yeoh hyperelastic model [36]. When the Yeoh parameters calculated from the tensile data (*vide infra*; see Figure A-8) were used to model indentation using a finite element simulation, the predicted force-displacement curves were very similar to those obtained experimentally; representative data are presented in Figure A-7. Because of the experimental error in measuring quantities such as the bulk film thickness or AFM cantilever spring constant, some differences in scalar magnitude between these two plots can be expected, although their shapes should be similar, as observed. The similarity between experimental AFM indentation data and simulations of the indentation using only bulk tensile properties is encouraging since it implies that the physical properties of thin and bulk films are similar, and it confirms the validity of the finite element analysis technique.

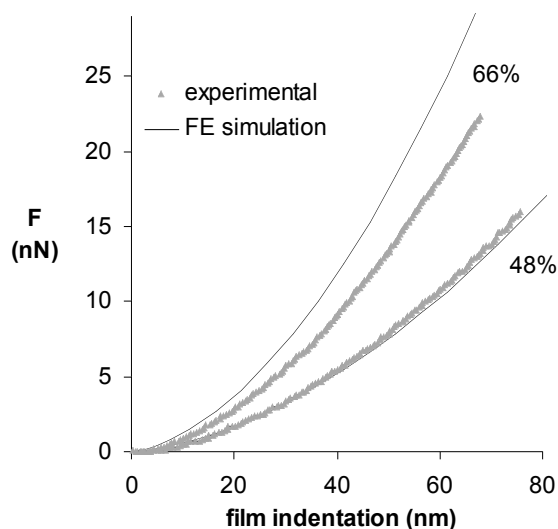


Figure A-7. Superposition of experimental AFM data and finite element simulations of indentation based on bulk tensile data for thin films of aE-66%-*p*N₃Phe and aE-48%-*p*N₃Phe.

The samples investigated here are thick relative to the indentation depth and are highly elastic, so the deviations from linearity are small, as can be seen by comparing the linear model fit with experimental AFM data in Figure A-6. However, the simulation approach should be applicable to thinner films (e.g., <100 nm) and to non-linear strain data as well, where a limited amount of data can be collected in the linear deformation range. While the Dimitriadis model is restricted to spherical tips, the simulation can be easily changed to describe conical or pyramidal tips, the type more commonly used because of their robustness and lower cost. These sharp tips have the additional advantage of being usable for imaging as well as indentation.

In performing the inverse analysis of predicting the AFM response from the tensile data, we used the AFM data to calculate a modulus for the material using the simulation. Coefficients of the Yeoh model were iterated in the finite element simulation to minimize the difference between the simulated and experimental AFM data using the entire force curve (including indentation data past 10% of the film thickness). The moduli determined in this way were indistinguishable from those calculated with the Dimitriadis model. If high-strain data are collected, this technique can provide the complete strain energy function for the material being tested in addition to the elastic Young's modulus (E). While the finite element technique provides more flexibility, the simplicity of the Dimitriadis model is preferable when the geometry of the tip is known and when the linear elastic modulus is the only value required.

A.3.6 Modulus control by variable incorporation of *pN₃Phe* – bulk films

As described earlier, the extent of incorporation of *pN₃Phe* into aE-*pN₃Phe* proteins can be controlled by varying the concentration of the photosensitive amino acid in the expression medium. We examined the effects of variable incorporation of *pN₃Phe*, both for bulk samples tested in uniaxial tension and for thin-film samples analyzed by AFM nanoindentation.

The tensile behavior of the bulk samples (Figure A-8) is typical of rubbery materials; all aE-*pN₃Phe* films were extensible to 150% (or greater) strains. As expected, the modulus increases with the *pN₃Phe* content of the protein, a result of increased crosslink density after irradiation. If the materials are assumed to behave as ideal rubber networks, the shear modulus (G) can be related to the crosslink density through the expression $G=(\rho RT/M_c)(1-2M_c/M)$ [37], an approximation shown to be valid for similar elastin-like hydrogels [17, 35]. The shear modulus is equal to one-third of the elastic modulus for an incompressible material ($\nu=0.5$), a good approximation for rubbery hydrated protein films. The chain mass density ρ is found by multiplying the density of elastin [38] (1.32 g/cm^3) by the measured polymer volume fraction (0.56) in the films, M_c is the average molecular weight between crosslinks, and the term $(1-2M_c/M)$ represents the fraction of elastically active crosslinks, where M is the molecular weight of the protein (42,900). The values of M_c calculated for the films examined here are listed in Table A-1A.

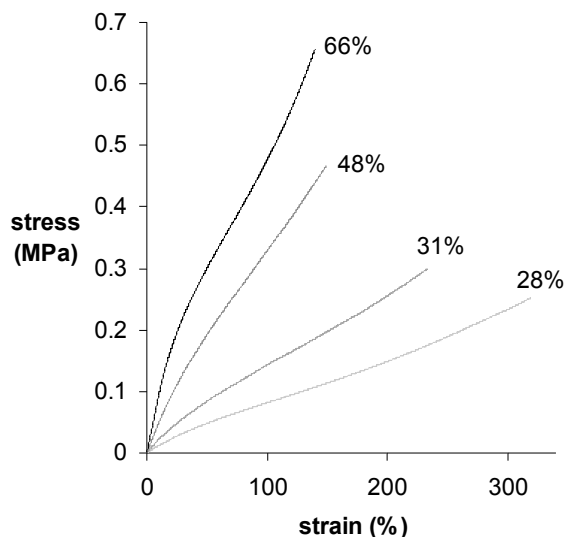


Figure A-8. Sample tensile data for bulk films containing varying amounts of pN_3Phe .

The efficiency of crosslinking can be calculated from M_c and the pN_3Phe content of the protein. For example, the value of M_c (4300) estimated for aE-66%- pN_3Phe corresponds to ca. 10 (42,900/4300) crosslinks per protein chain, assuming random crosslinking – a reasonable assumption given the periodic Phe spacing in the protein and the statistical nature of its replacement by pN_3Phe . Incorporation of the photosensitive amino acid at 66% of the 15 Phe sites yields an average of 9.9 pN_3Phe side chains per molecule; because each crosslinking event couples two molecules, the measured value of M_c indicates a reaction efficiency of ca. 50% (10/9.9/2). The crosslinking efficiency declines slightly as the pN_3Phe content of the film is reduced (Table A-2A).

A.3.7 Modulus control by variable incorporation of pN_3Phe – thin films

Figure A-9 compares the elastic moduli calculated from AFM data for thin films to those measured for bulk films in uniaxial tension. For aE-48%- pN_3Phe and aE-66%- pN_3Phe , the values match within experimental error, indicating that the mechanical

properties of the bulk films can be reproduced in films 200-400 nm thick, and supporting the validity of the Dimitriadis model for measuring Young's modulus. The bulk and thin films, although cast from different solvents, are both crosslinked in the dry state, and are thus expected to have similar structures and elastic moduli. For films of lower pN₃Phe content, AFM yields moduli slightly higher than those obtained from tensile measurements (Table A-2B).

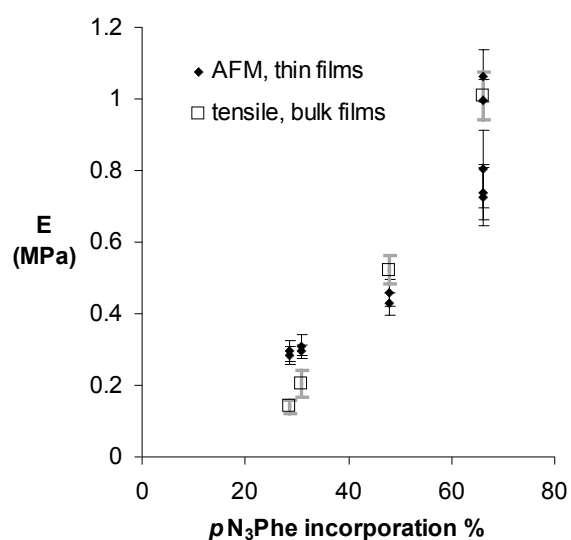


Figure A-9. Measured elastic moduli of thin films of aE-pN₃Phe versus fraction replacement of Phe by pN₃Phe. Results from AFM nanoindentation of thin films and tensile testing of bulk films are compared.

Engineering of the elastic moduli of thin protein films by controlling pN₃Phe content should prove useful in cell culture experiments designed to study mechanosensitive cell behavior. An especially attractive prospect is the use of microfluidic mixing [15, 39] to prepare protein substrates characterized by controlled gradients in elastic modulus.

A.3.8 Modulus control by variable irradiation

Elastic modulus gradients can also be prepared by variation in the radiation dose used for photocrosslinking. To demonstrate, we prepared a step-gradient by irradiating adjacent portions of an aE-66%- pN_3 Phe film for increasing lengths of time. The elastic moduli measured (by AFM) at different locations on the film are shown in Figure A-10; the modulus increases slightly more than two-fold as the irradiation time increases from 20 to 300 sec. The majority of the rise in elastic modulus occurs over the first minute of exposure, consistent with the photolysis behavior reported previously [24].

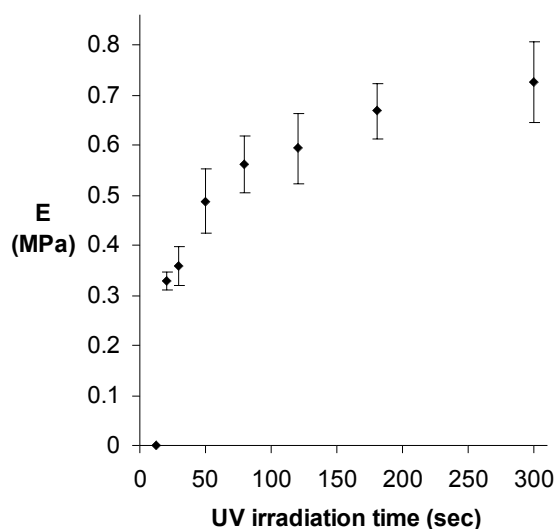


Figure A-10. Preparation of a step gradient in elastic modulus by variable irradiation of a single aE-66%- pN_3 Phe film. Error bars indicate standard deviation in modulus within each zone of the gradient.

When the gradient film was washed to remove soluble protein, the thicknesses of the 20 sec and 30 sec zones were ca. 35% and ca. 20%, respectively, less than the thickness of the zones irradiated for longer periods, indicating incomplete crosslinking. Taking into account the known film height (as in the Dimitriadis calculation of the

modulus) is essential for these gradient films, since variable film height would make the Hertz model inaccurate even as a comparative measure of the local elastic modulus.

Films that exhibit spatial variation in modulus on millimeter length scales offer unique advantages as substrates for the study of cell behavior. Large numbers of cells can be cultured on each zone of a step-gradient substrate, allowing average cell properties to be measured as a function of elastic modulus on a single substrate. This approach minimizes reagent use and substrate preparation, and avoids lot-to-lot variation in the behavior of cultured cells. Observation of cell behavior at interfaces between stiff and soft materials has also proven instructive [6]. Films with more complex patterns of mechanical properties can also be envisioned. Irradiation through a mask, used previously to pattern proteins on solid supports [24], could be easily adapted to the preparation of films with micropatterned moduli. Cell behavior on micropatterned materials has been the subject of a recent study [40].

While step gradients are easy to characterize with a limited number of indentations, films with smooth gradients of elastic modulus could also be made via the variable irradiation approach by moving an opaque shutter continuously across the film [41]. Gradients could be implemented over a variety of length scales. The spatial resolution of the modulus measurement is limited only by the 300 nm radius of the tip used for indentation, and is adequate for measurement of the variation in mechanical properties under a single spread cell. Even higher resolution might be achieved through use of conventional sharp (<20 nm) conical or pyramidal tips together with finite element analysis of the indentation process. Gradients extending over distances greater than the

ca. 100 μm lateral piezo range of conventional AFM instruments could be characterized by using translational reference points in the sample.

A.4 Conclusions

Incorporation of the photosensitive amino acid *para*-azidophenylalanine into artificial proteins enables the photochemical synthesis of thin protein films of controlled elastic modulus. A film height-dependent indentation model, validated by bulk tensile measurements and finite element simulation, allows the elastic modulus to be determined with confidence by nanoindentation. The thin films prepared in this work enable new approaches to the study of mechanosensitive cell behavior in the context of coincident biological signals.

A.5 Acknowledgment

We gratefully acknowledge support of this research by the Center for the Science and Engineering of Materials at Caltech (NSF DMR-0520565) and by NIH grant EB1971. We thank Marissa Mock for NMR characterization and Doron Shilo for help with AFM measurements.

A.6 References

1. Discher, D.E., P. Janmey, and Y.L. Wang, *Tissue cells feel and respond to the stiffness of their substrate*. Science, 2005. **310**(5751): 1139-1143.

2. Pelham, R.J., and Y.L. Wang, *Cell locomotion and focal adhesions are regulated by substrate flexibility*. Proceedings of the National Academy of Sciences of the United States of America, 1997. **94**(25): 13661-13665.
3. Cukierman, E., et al., *Taking cell-matrix adhesions to the third dimension*. Science, 2001. **294**(5547): 1708-1712.
4. Engler, A., et al., *Substrate compliance versus ligand density in cell on gel responses*. Biophysical Journal, 2004. **86**(1): 617-628.
5. Engler, A.J., et al., *Surface probe measurements of the elasticity of sectioned tissue, thin gels and polyelectrolyte multilayer films: Correlations between substrate stiffness and cell adhesion*. Surface Science, 2004. **570**(1-2): 142-154.
6. Lo, C.M., et al., *Cell movement is guided by the rigidity of the substrate*. Biophysical Journal, 2000. **79**(1): 144-152.
7. Gray, D.S., J. Tien, and C.S. Chen, *Repositioning of cells by mechanotaxis on surfaces with micropatterned Young's modulus*. Journal of Biomedical Materials Research Part A, 2003. **66A**(3): 605-614.
8. Wang, H.B., M. Dembo, and Y.L. Wang, *Substrate flexibility regulates growth and apoptosis of normal but not transformed cells*. American Journal of Physiology–Cell Physiology, 2000. **279**(5): C1345-C1350.
9. Engler, A.J., et al., *Myotubes differentiate optimally on substrates with tissue-like stiffness: pathological implications for soft or stiff microenvironments*. Journal of Cell Biology, 2004. **166**(6): 877-887.
10. Engler, A.J., et al., *Matrix elasticity directs stem cell lineage specification*. Cell, 2006. **126**(4): 677-689.

11. Engler, A.J., et al., *Microtissue elasticity: Measurements by atomic force microscopy and its influence on cell differentiation*. Cell Mechanics, 2007. **83**: 521-545.
12. Wang, Y.L., and R.J. Pelham, *Preparation of a flexible, porous polyacrylamide substrate for mechanical studies of cultured cells*. Molecular Motors and the Cytoskeleton, Pt B, 1998. **298**: 489-496.
13. Maskarinec, S.A., and D.A. Tirrell, *Protein engineering approaches to biomaterials design*. Current Opinion in Biotechnology, 2005. **16**(4): 422-426.
14. Wong, J.Y., et al., *Directed movement of vascular smooth muscle cells on gradient-compliant hydrogels*. Langmuir, 2003. **19**(5): 1908-1913.
15. Zaari, N., et al., *Photopolymerization in microfluidic gradient generators: Microscale control of substrate compliance to manipulate cell response*. Advanced Materials, 2004. **16**(23-24): 2133-2137.
16. Panitch, A., et al., *Design and biosynthesis of elastin-like artificial extracellular matrix proteins containing periodically spaced fibronectin CS5 domains*. Macromolecules, 1999. **32**(5): 1701-1703.
17. Welsh, E.R., and D.A. Tirrell, *Engineering the extracellular matrix: A novel approach to polymeric biomaterials. I. Control of the physical properties of artificial protein matrices designed to support adhesion of vascular endothelial cells*. Biomacromolecules, 2000. **1**(1): 23-30.
18. Di Zio, K., and D.A. Tirrell, *Mechanical properties of artificial protein matrices engineered for control of cell and tissue behavior*. Macromolecules, 2003. **36**(5): 1553-1558.

19. Liu, J.C., S.C. Heilshorn, and D.A. Tirrell, *Comparative cell response to artificial extracellular matrix proteins containing the RGD and CS5 cell-binding domains*. Biomacromolecules, 2004. **5**(2): 497-504.
20. Mould, A.P., et al., *The Cs5 Peptide Is a 2nd Site in the Iiics Region of Fibronectin Recognized by the Integrin Alpha-4-Beta-1-Inhibition of Alpha-4-Beta-1 Function by Rgd Peptide Homologs*. Journal of Biological Chemistry, 1991. **266**(6): 3579-3585.
21. Urry, D.W., *Physical chemistry of biological free energy transduction as demonstrated by elastic protein-based polymers*. Journal of Physical Chemistry B, 1997. **101**(51): 11007-11028.
22. Kast, P., and H. Hennecke, *Amino-Acid Substrate-Specificity of Escherichia-Coli Phenylalanyl-Transfer Rna-Synthetase Altered by Distinct Mutations*. Journal of Molecular Biology, 1991. **222**(1): 99-124.
23. Kirshenbaum, K., I.S. Carrico, and D.A. Tirrell, *Biosynthesis of proteins incorporating a versatile set of phenylalanine analogues*. Chembiochem, 2002. **3**(2-3): 235-237.
24. Carrico, I.S., et al., *Lithographic patterning of photoreactive cell-adhesive proteins*. Journal of the American Chemical Society, 2007. **129**(16): 4874-4875.
25. Vinckier, A. and G. Semenza, *Measuring elasticity of biological materials by atomic force microscopy*. Federation of European Biochemical Societies Letters, 1998. **430**(1-2): 12-16.
26. Cappella, B. and G. Dietler, *Force-distance curves by atomic force microscopy*. Surface Science Reports, 1999. **34**(1-3): 1-103.

27. Heinz, W.F., and J.H. Hoh, *Spatially resolved force spectroscopy of biological surfaces using the atomic force microscope*. Trends in Biotechnology, 1999. **17**(4): 143-150.
28. Mahaffy, R.E., et al., *Scanning probe-based frequency-dependent microrheology of polymer gels and biological cells*. Physical Review Letters, 2000. **85**(4): 880-883.
29. Richert, L., et al., *Elasticity of native and cross-linked polyelectrolyte multilayer films*. Biomacromolecules, 2004. **5**(5): 1908-1916.
30. Costa, K.D., and F.C.P. Yin, *Analysis of indentation: Implications for measuring mechanical properties with atomic force microscopy*. Journal of Biomechanical Engineering—Transactions of the ASME, 1999. **121**(5): 462-471.
31. Dimitriadis, E.K., et al., *Determination of elastic moduli of thin layers of soft material using the atomic force microscope*. Biophysical Journal, 2002. **82**(5): 2798-2810.
32. Domke, J., and M. Radmacher, *Measuring the elastic properties of thin polymer films with the atomic force microscope*. Langmuir, 1998. **14**(12): 3320-3325.
33. Akhremitchev, B.B., and G.C. Walker, *Finite sample thickness effects on elasticity determination using atomic force microscopy*. Langmuir, 1999. **15**(17): 5630-5634.
34. Sharma, N., PhD Thesis. 2001, Unniversity of Massachusetts Amherst.
35. Nowatzki, P.J., and D.A. Tirrell, *Physical properties of artificial extracellular matrix protein films prepared by isocyanate crosslinking*. Biomaterials, 2004. **25**(7-8): 1261-1267.

36. Yeoh, O.H., *Some Forms of the Strain-Energy Function for Rubber*. Rubber Chemistry and Technology, 1993. **66**(5): 754-771.
37. Flory, P.J., *Principles of Polymer Chemistry*, 1953, Ithaca, NY: Cornell University Press.
38. Lillie, M.A., and J.M. Gosline, *Unusual swelling of elastin*. Biopolymers, 2002. **64**(3): 115-126.
39. Jeon, N.L., et al., *Generation of solution and surface gradients using microfluidic systems*. Langmuir, 2000. **16**(22): 8311-8316.
40. Stevens, M.M., and J.H. George, *Exploring and engineering the cell surface interface*. Science, 2005. **310**(5751): 1135-1138.
41. Pucci, V., et al., *Monolithic columns with a gradient of functionalities prepared via photoinitiated grafting for separations using capillary electrochromatography*. Journal of Separation Science, 2004. **27**(10-11): 779-788.

Appendix B

With kind permission from Springer Science+Business Media:

Experimental Mechanics, Three-Dimensional Full-Field Measurements of Large
Deformations in Soft Materials using Confocal Microscopy and Digital Volume

Correlation, 47(3), 2007, p. 427-438, Franck, C., Hong, S., Maskarinec, S.A., Tirrell,
D.A., and G. Ravichandran, Figures 1–12.

Abstract

A three-dimensional (3-D) full-field measurement technique was developed for measuring large deformations in optically transparent soft materials. The technique utilizes a digital volume correlation (DVC) algorithm to track motions of subvolumes within 3-D images obtained using fluorescence confocal microscopy. In order to extend the strain measurement capability to the large deformation regime ($> 5\%$), a stretch-correlation algorithm was developed and implemented into the Fast Fourier Transform (FFT)-based DVC algorithm. The stretch-correlation algorithm uses a logarithmic coordinate transformation to convert the stretch-correlation problem into a translational correlation problem under the assumption of small rotation and shear. Estimates of the measurement precision are provided by stationary and translation tests. The proposed measurement technique was used to measure large deformations in a transparent agarose gel sample embedded with fluorescent particles under uniaxial compression. The technique was also employed to measure non-uniform deformation fields near a hard spherical inclusion under far-field uniaxial compression. Introduction of the stretch-correlation algorithm greatly improved the strain measurement accuracy by providing better precision especially under large deformation. Also, the deconvolution of confocal images improved the accuracy of the measurement in the direction of the optical axis. These results show that the proposed technique is well-suited for investigating cell-matrix mechanical interactions as well as for obtaining local constitutive properties of soft biological tissues in 3-D.

B.1 Introduction

The importance of mechanical signals in directing cellular behaviors such as adhesion, motility, differentiation and morphogenesis has become evident in recent years [1-4]. Yet there is minimal understanding regarding the intricate coupling of mechanical and biochemical signaling at the cellular level [5]. This knowledge gap is mainly due to the lack of experimental tools that can accurately measure forces and deformations at the cellular or sub-cellular level with sufficiently high sensitivities and wide applicable ranges. Previous investigations on the influence of mechanical stimuli predominantly focused on two-dimensional cell-substrate interactions that occur during cell spreading and migration [6, 7]. Although these reports have contributed much to the understanding of cell behavior in two-dimensional environments, it has been recently demonstrated that cells show distinct three-dimensional morphologies and interactions, as expected in vivo [8-10]. Thus, in order to characterize and understand cell-matrix interactions at the single cell and sub-cellular level, forces and motions in three-dimensions must be quantitatively measured and analyzed. Even though technical advances in microscopy have allowed for feature sizes as small as nanometers to be resolved [11], the nature of most of the previously presented measurements remains two-dimensional. Attempts to employ stereo-imaging techniques to capture three-dimensional deformation fields [12] have been successful, but these methods only provide surface information.

Motivated by the need for capturing mechanical responses of a motile cell in a three-dimensional extracellular matrix (ECM), a promising new technique that uses the three-dimensional imaging capability of confocal microscopy coupled with a digital volume correlation (DVC) algorithm was developed in this study. Analogous to the

digital image correlation (DIC) technique [13, 14] where in general two-dimensional displacement fields are measured, the DVC uses volume subsets to track the three-dimensional displacement fields within the matrix. One main advantage of the proposed algorithm over those reported previously [15-17] is that the method presented here takes into consideration the stretch deformation of each volume subset. Also, a deconvolution algorithm is used to minimize the blurring of the confocal images. These two improvements allow for a more accurate strain estimate, especially when local strains are large and subset deformation is significant. Another advantage over previous studies is that the results do not depend on the local sample feature size to achieve high correlation resolution, but rather can be tailored to the relevant length scale of interest. This is achieved by utilizing commercially available fluorescent markers rather than relying on the autofluorescence of the sample, which can limit the field of view. The method presented here allows the user to choose virtually any field of view provided the availability of the appropriate markers. Using this method, material properties of soft materials can be experimentally determined, especially where conventional characterization techniques fail due to the compliant nature of the material.

This paper is organized as follows. In Section B-2, a brief description of the laser scanning confocal microscope (LCSM) is presented. The details of the digital volume correlation methodology and algorithm developments are described in Section B-3. The experimental procedures are given in Section B-4 and the results are presented and discussed in Section B-5. Conclusions for the present study are summarized in Section B-6.

B.2 Laser Scanning Confocal Microscope (LSCM)

Confocal microscopy has emerged as a powerful imaging technique owing to the optical sectioning capability enabling construction of three-dimensional images. In conventional wide-field microscopy, light is collected from the entire sample volume, including the focal plane as well as all other planes, whereas, in confocal microscopy, light is generally collected from the focal plane only. This is achieved by using a pinhole in front of a photomultiplier tube (PMT) detector that blocks the incoming light from all other planes. As illustrated in Figure B-1, the solid line represents light reflected or emitted from the focal plane, while the dashed line represents light from the out-of-focus plane. The overall contrast and resolution of the image is significantly increased as compared to conventional wide-field microscopy where the image is blurred by out-of-plane light. Furthermore, the inherent optical sectioning of the specimen in confocal microscopy allows the assembly of three-dimensional image volumes by stacking together individually acquired planar slices. In a LSCM system, a laser with a single-diffraction limited spot size is used to sequentially scan a selected focal plane. Thus, the image is not formed using a CCD camera as in conventional microscopy, but rather the image is a result of the light's interaction with successive areas of the specimen, i.e. the image is recorded pixel by pixel analogous to a scanning electron microscope. The resulting image is generally superior in resolution to images recorded by conventional optical microscopy. A more detailed description of the confocal principle and the current applications of confocal microscopy are well documented and can be found elsewhere [18, 19].

In the present study, fluorescent markers were added to the transparent materials of interest and they served as image sources for constructing the 3-dimensional images and as markers for performing DVC described in the next section.

B.3 Digital Volume Correlation (DVC)

B.3.1 Principle of DVC

LSCM provides discretized volume images visualizing 3-dimensional structural patterns of fluorescent markers in a transparent sample. In this study, the combination of digital volume correlation (DVC) and confocal images is used to achieve 3-dimensional full-field deformation measurements as an extension of the vision-based surface deformation measurement techniques, well-known as digital image correlation (DIC). The basic principle of the DVC is schematically illustrated in Figure B-2. Two confocal volume images of an agarose gel with randomly dispersed fluorescent particles are obtained before and after mechanical loading. Then, the two images are subdivided into a set of subvolumes that are centered on the points of interest. Using each pair of corresponding subvolume images, the respective local displacement vector can be obtained from 3-dimensional volume correlation methods.

Consider two scalar signals $f(x)$ and $g(x)$ which represent a pair of intensity patterns in a sub-volume Ω before and after a continuous mapping, $\hat{y}(x): x \rightarrow y$, respectively. Assuming that the signal is locally invariant during the mapping, $f(x) = g(y(x))$, subvolume-wise correlation matching can be obtained by finding an optimal mapping that maximizes the cross-correlation functional defined as

$$m(\hat{y}) = \int f(x)g(y(x))d\Omega_x \quad (1)$$

The methodology is illustrated using a translational volume correlation, which is presented below. The continuous mapping is assumed to be a rigid translation, $y = x + c$, and the cross-correlation function is represented as a function of a displacement vector c as

$$m(c) = \int f(x)g(x+c)d\Omega_x \quad (2)$$

The cross-correlation function can be written using Fourier transforms as follows

$$m(c) = F^{-1}\left[F[f(x)]^* F[g(x)]\right] \quad (3)$$

where the Fourier transform of $f(x)$ is defined as

$$F[f(x)] = \int f(x)e^{-ik \cdot x} d\Omega_x \quad (4)$$

and $*$ denotes the complex conjugate. The discrete cross-correlation function can be computed efficiently by using the Fast Fourier Transform (FFT) algorithm. Then, the rigid translation vector \mathbf{c} can be estimated from the location of the cross-correlation peak with respect to the origin. Finding a voxel-resolution displacement vector \mathbf{c} from the discrete cross-correlation function is straightforward and provides half-voxel accuracy. Determining the displacement vector \mathbf{c} in sub-voxel accuracy generally requires fitting and interpolation of the correlation function near the peak. Various fitting models have been used in the past [20, 21], employing somewhat arbitrary assumptions that the cross-correlation function near the peak can be approximated by a Gaussian or a parabolic function. The sub-voxel accuracy of such peak-finding algorithms is determined by the choice of fitting function as well as the size of the fitting window. In this study, a three-dimensional quadratic polynomial fitting is used to accurately fit the correlation function near the peak and hence provide improved sub-pixel accuracy.

However, significant measurement error can be introduced from the decorrelation of the intensity patterns when the rotation or the stretch of the subvolume is large. Thus, applications of such simple correlation algorithms have been limited to small strain and small rotation problems due to the inherent limitation of the rigid-translation assumption. In general, the applicability of such algorithm is limited up to about 5% of strain or 0.05 radian of rotation angle [20]. In order to overcome this limitation and to obtain more accurate displacement measurements, a higher-order approximation of the deformation field within each subvolume is required for large deformation measurements in soft materials. In the following section, an extension of the FFT-based DVC to measure large deformation fields is presented.

B.3.2 Stretch correlation

Assuming uniform deformation of each subvolume, a general homogeneous deformation field can be written as

$$\hat{y}(x) = Fx + c \quad (5)$$

with a deformation gradient tensor $F = I + u\nabla$ and a displacement vector u . Therefore, any uniform deformation in 3-dimensions can be represented with a total of 12 parameters which consist of 3 displacement components and 9 displacement gradient components. Optimal programming in 3-dimensions for a total of 12 degrees of freedom (DOF) is computationally expensive in conventional correlation algorithms.

Alternatively, the general homogeneous deformation can be represented with a polar decomposition of the deformation gradient tensor as

$$\hat{y}(x) = RUx + c \quad (6)$$

where R is the orthogonal rotation tensor and U is the symmetric right-stretch tensor. Then, the general homogeneous deformation in 3-dimensions is represented with 6 stretch, 3 rotation and 3 translation components. Depending on the dominant mode of the deformation of interest, the correlation algorithm can be modified to include additional optimization parameters selectively. A digital volume correlation algorithm that includes three rotational degrees of freedom has been presented previously [17]. In this study, assuming small rotations and small shear stretch components, three normal stretch components are included as additional correlation parameters in the FFT-based DVC algorithm, as an extension of the stretch-correlation algorithm developed for large deformation measurements in two-dimensions [22].

Neglecting the small rotations, the mapping of a pure homogeneous deformation and a rigid translation is written as

$$\hat{y}(x) = Ux + c \quad (7)$$

When the loading axes are aligned with the global coordinate axes so that the shear stretch components are small, the invariant condition can be written as

$$f(x) \approx g(\bar{U}x + c) \quad (8)$$

where \bar{U} denotes the diagonal part of U . Then, the six optimization parameters for the stretch correlation in DVC algorithm are $\{c_1, c_2, c_3, U_{11}, U_{22}, U_{33}\}$.

In the case of a pure stretch problem without any translation, a simple coordinate transform into a logarithmic scale converts the stretch correlation problem into a simple translational correlation problem. However, when there is a non-zero translation, the coordinate transform cannot be directly performed in the spatial-domain to achieve the

stretch correlation. Therefore, an equivalent invariant condition of (8) in the Fourier-domain is considered to implement the stretch correlation in the Fourier-domain as

$$\|\bar{U}\|F(\bar{U}k) = e^{ik \cdot c}G(k) \quad (9)$$

where $F(k)$ and $G(k)$ represent Fourier transforms of $f(x)$ and $g(x)$, respectively. Then by using the Fourier power spectrums only and therefore dropping the phase term, a translation-invariant stretch-correlation problem can be achieved in the Fourier-domain. A stretch cross-correlation function to be maximized for determining the 3 axial stretch components neglecting the determinant of jacobian is shown as

$$m(\bar{U}) = \int |F(\bar{U}k)| |G(k)| d\Omega_k \quad (10)$$

The stretch correlation problem in the Fourier-domain can be transformed into a translational correlation problem in a log-frequency domain as

$$\tilde{m}(\eta) = \int |\tilde{F}(\xi + \eta)| |\tilde{G}(\xi)| d\Omega_\xi \quad (11)$$

where $\xi = \log_b k$ and $\eta = \log_b \bar{U}$. The translational correlation problem in the log-frequency domain can be easily solved using (3). Finally, the three axial stretch components can be obtained from the optimal vector η in the log-frequency domain as follows

$$U_{11} = b^{\eta_1}, U_{22} = b^{\eta_2}, U_{33} = b^{\eta_3} \quad (12)$$

The accuracy of the obtained stretch components depends strongly on the spectral content of the original signals. If the signals are already band-limited, special considerations, such as normalizing the power spectrums and employing the Hanning window, must be included to achieve robust stretch correlations. Also, in the numerical implementation of the stretch correlation algorithm, incorporating zero-padding of the signals before Fourier transforms can improve the overall accuracy of the stretch

correlation algorithm by providing ideal interpolations of the Fourier transforms at a cost of increased computational load.

In Figure B-3, the stretch-correlation procedures are illustrated using a one-dimensional example. Two reference and deformed signals representing 10% of uniform strain are shown in Figure B-3(a). The Fourier power spectrums of the two signals are shown in Figure B-3(b). Note that only half of the full frequency range is shown due to the inherent Fourier symmetry. In Figure B-3(c), the equivalent Fourier power spectrums are shown after the zero-padding as ideal interpolations of the power spectrums in Figure B-3(b). Figure B-3(d) shows the Fourier power spectrums along the logarithmic axis. After interpolating the power spectrums using a uniform interval in the log-frequency domain as shown in Figure B-3(e), the translational correlation as presented in (11) can be applied to find the 1-D stretch value. Extension of the 1-D stretch-correlation into 2-D or 3-D is straightforward as long as rotation and shear stretch are small.

In the implementation of 3-D stretch correlation, 2-D projections of the 3-D subvolume images were used to circumvent the geometrically increased computational load after the zero padding, as shown in Figure B-4. Essentially, the stretch correlations using the large zero-padding were conducted in a reduced dimension for computational efficiency. Three separate 2-D projections were conducted so that three sets of two stretch components can be obtained. From the six stretch values, three stretch components (U_{11} , U_{22} , U_{33}) were obtained by computing the average of the two corresponding stretch components.

Once the three axial stretch components are found, the translation vector \mathbf{c} can be determined more accurately by conducting the stretch-compensated translational correlation using

$$m(c) = \int \tilde{f}(x')g(x' + c)d\Omega_{x'} \quad (13)$$

where $f(x) = \tilde{f}(\bar{U}x)$ and $x' = \bar{U}x$. The stretch-compensated translational correlation requires the initial subvolume image $f(x)$ to be stretched to $\tilde{f}(x')$ according to the obtained three stretch values. Therefore the process involves sub-voxel interpolations of the initial subvolume image. Because the stretch part of the deformation is compensated, a more accurate translation vector \mathbf{c} can be obtained. The stretch correlation and the translational correlation were conducted iteratively to achieve converging results. For all experiments executing the stretch and translational correlation twice yielded sufficient convergence based on a mean difference criterion, where the mean and standard deviation of the difference of the before and after displacement matrices were compared (this is similar to least-square error estimate). Such an iteration process is equivalent to the iterative optimization of a correlation coefficient in conventional image correlation scheme conducted in the spatial domain.

Finally, the displacement gradients were computed by using a 3-dimensional least-square fitting of each displacement component in a 3x3x3 grid of neighboring data points. Although more sophisticated smoothing or filtering algorithm can be employed before or during the gradient calculation in order to obtain smoother strain fields, no such algorithm was used in this study to assess the performance and robustness of the proposed DVC algorithm. Once the displacement gradient fields are determined, either

infinitesimal or finite strain values can be computed from the displacement gradient fields.

B.3.3 DVC using confocal microscope images

The spatial resolution of a confocal microscope is determined by the 3-dimensional point spread function (PSF) which is an intensity distribution near the focal point corresponding to a volume image of a point light source under a diffraction-limited imaging system. The 3-dimensional PSF has an ellipsoidal shape elongated along the optical axis [23, 24]. Thus, the obtained confocal image is the convolution of actual intensity distributions using the PSF as a kernel. Consequently, the axial spatial resolution of confocal imaging is 3 to 10 times worse than the lateral spatial resolution depending on the refractive index of the medium and the numerical aperture of the objective lens.

In Figure B-6 (a), an isosurface plot of a typical confocal subvolume image (64x64x64 voxels) of a transparent agarose gel with randomly dispersed fluorescent spherical particles of 2 voxels diameter is shown. The spherical fluorescent particles appear as axially elongated ellipsoids. The blurring in the axial direction causes increased uncertainties in the DVC measurements of the axial direction components. The consequence of such blurring is particularly critical to the performance of the stretch correlation algorithm that uses the Fourier power spectrums. In this study, the noise-resistant Lucy-Richardson deconvolution algorithm [25] was used to deconvolve the raw confocal images using a sinc PSF in the axial direction prior to the stretch correlation. Figure B-6 (b) shows a subvolume image obtained after deconvolution of the raw image.

There are two additional confocal-imaging artifacts caused by the refractive index mismatch in the optical path. First, spherical aberration due to the refractive index mismatch causes asymmetric distortions of the 3-dimensional PSF as a function of the penetration depth. Such a distorted and depth-dependent PSF makes the deconvolution of the confocal images difficult and causes significant error in the DVC. Effects of such spherical aberration in confocal imaging have been extensively studied in the past [26, 27]. In practice, the spherical aberration can be minimized by adjusting the correction collar commonly equipped in commercial microscope objectives. In order to minimize the distortion of the PSF within the field of view, the correction collar needs to be adjusted appropriately prior to each test. The second form of confocal imaging artifact due to the refractive index mismatch is caused by the fact that the focal point does not follow the axial motion of the scanning stage [28, 29]. This causes an over- or under-estimation of the depths depending on the ratio of the refractive index mismatch. This apparent discrepancy between the axial and the lateral scanning resolutions can be calibrated by imaging large fluorescent microspheres embedded in a sample.

B.4 Experimental Procedures

Test specimens were prepared from a 1% (w/v) solution of agarose (J.T. Baker, NJ) in standard 0.5X TBE buffer (Tris/Borate/EDTA, pH 8.0). The agarose solution was heated until molten, and carboxylate-modified red fluorescent (580/605) polystyrene microspheres (Invitrogen, CA) of 1 μ m diameter were injected into the liquid agarose. The nominal volume fraction of fluorescent markers in the gel was 0.3%. The addition of the fluorescent microspheres seemed negligible to both the local or global mechanical

response of the agarose gel. The nominal volume fraction of fluorescent markers in the gel was 0.3%. The mixture was cast into a pre-chilled Teflon mold mounted onto a glass plate. Samples were left at room temperature for 5 minutes to solidify. This protocol yielded circular agarose specimens with typical dimensions of 6.4 mm diameter and 1.4 mm height. For spherical inclusion experiments, spherical polymethylmethacrylate (PMMA) beads (Sigma-Aldrich, MO) of 100 μm diameter were added to the mixture before casting.

In order to apply uniaxial compressive loading to the sample while imaging, a miniature loading-fixture was built and mounted directly on top of the microscope stage of an inverted optical microscope as shown in Figure B-7. The sample was kept immersed in the buffer solution to prevent swelling or shrinking during the test. The compressive loading was achieved by translating a micrometer head with a resolution of 1 μm . For all experiments the imposed strain increments were controlled by the micrometer and were calculated using the dimension of the specimen and the imposed loading (displacement) step. The resulting applied force was measured using a 10-gram load cell (A.L. Design, NY). Nominal stress-strain curves were compiled using this setup for each test. The LSCM used in this study was a confocal system (Nikon C-1) combined with an inverted optical microscope (Nikon TE-2000-U). A 40x CFI planar fluor air objective with a numerical aperture of 0.6 was used in all experiments.

B.5 Results and Discussions

B.5.1 Characterization of measurement precision

In order to verify the measurement precision of the DVC algorithm using confocal volume images, two tests were conducted under zero-strain condition. In the first test, two confocal volume images were repeatedly acquired from a stationary sample under zero load. The scanning resolution was $512 \times 512 \times 512$ voxels, and the scan spacing was $0.45 \mu\text{m}$ in all three directions. This resulted in a field of view of $230 \times 230 \times 230 \mu\text{m}^3$. In the second test, two confocal images were acquired before and after translating the unloaded sample using the x_3 -directional scanning stage of the confocal microscope. The two pairs of the confocal images were analyzed by using the DVC algorithm with a subvolume size of $64 \times 64 \times 64$ voxels. Displacements were measured at $15 \times 15 \times 15$ points (total 3375 points) in a uniform grid of 32 voxels spacing. Displacement gradients were then calculated by using the displacement data at $3 \times 3 \times 3$ neighboring grid points following linear least-square fitting of the displacement components. Although the quadratic (Lagrangian) or the logarithmic (true) strain measure can be used for large deformation analysis, the linear (engineering) strain measure was used to represent the deformations in this study. As a quantitative measure of the uncertainties in the DVC results, standard deviation values of three displacement components and three normal strain components were computed and summarized in Table B-1.

The absolute values of the uncertainties in the displacements and the strains are comparable to previously reported results [15, 16]. These measurement uncertainties are likely due to the noises in the confocal images caused by the PMT detector noise as well as the positional uncertainty of the laser scanning system. It is also noted that the axial

uncertainties of the displacement and strain components in the x_3 -direction are approximately 3 to 5 times higher than the corresponding lateral uncertainties in the x_1 - and x_2 -directions (in-plane). This result shows that the axially elongated three dimensional PSF causes a significantly degraded measurement precision in the x_3 -direction. These tests under zero-strain condition provide a simple way to assess baseline uncertainties of the measurements using the DVC algorithm.

B.5.2 Uniaxial compression test

In order to verify the 3-dimensional deformation measurement capability of the DVC using the LSCM, the agarose gel sample was compressed uniaxially with nominal strain increments of 2-3%. The total imposed nominal strain was approximately 10%. The obtained confocal images were analyzed using the DVC algorithm with a subvolume size of 64x64x64 voxels. Figure B-8 (a) shows a vector plot of the measured displacement field. Figure B-8 (b) shows a 3-dimensional contour plot of the vertical displacement components.

In order to assess the performance of the DVC algorithm with the stretch-correlation for large deformation measurements, accuracy and precision must be established systematically. The accuracy and the precision of a measurement technique are usually achieved by repeatedly measuring some traceable reference standard. Then, the accuracy and precision are typically quantified as the difference between the mean of the measured values and the true value, and as the standard deviation of the measured values, respectively.

Mean and standard deviation values of the measured strain fields are presented in Table B-2 to assess the effectiveness of the stretch-correlation algorithm. The mean values of the lateral strain components ϵ_{11} and ϵ_{22} are close to zero and smaller than their corresponding standard deviation values, i.e. the measurement precision, and are therefore negligible. The standard deviations of the no-stretch-correlated and stretch correlated lateral strain components are similar illustrating that the stretch-correlation does not improve the precision of the strain measurements for small strains. Comparing the no-stretch and stretch-corrected axial strain component ϵ_{33} , the difference of 0.09% between the two mean values is smaller than their corresponding standard deviation values, which shows that the stretch correlation does not improve the accuracy of the *average* strain measurement. However, the standard deviation in the stretch-correlation case is less than half of that in the no stretch-correlation case. This proves that the stretch correlation greatly improves the precision of the large-deformation measurement. Although precise measurements do not necessarily mean accurate measurements, it is often not possible to reliably achieve high accuracy in individual measurements without precision. This point is particularly important in the full-field measurement of non-uniform deformation fields.

Since it is not possible to know the true value of the compressive strain up to the level of accuracy and precision of the measurement technique under investigation, the absolute accuracy of the proposed DVC method cannot be assessed with the nominal strain value from the global measurement. However it is clear that overall measurement accuracy can be improved by providing better precision, since precision is a limit of accuracy. The results from the uniaxial compression test show that the proposed stretch-

correlation algorithm in conjunction with the deconvolution algorithm improved the overall accuracy of large deformation measurement with better precision.

The average axial compressive strain value was 9.3%, whereas the average lateral strain values were negligible. The result showed that the lateral expansion due to the Poisson effect was effectively constrained due to the disc-shaped geometry of the sample. To determine the material properties of the agarose sample correctly the uniaxial test results need to be interpreted as a constrained compression of a soft layer yielding expression (14), where the axial stress-strain ratio for constrained compression is defined as a constrained modulus and related to elastic properties as follows,

$$\frac{\sigma_{33}}{\varepsilon_{33}} = \frac{(1-\nu)E}{(1+\nu)(1-2\nu)}, (\varepsilon_{11} = \varepsilon_{22} = 0) \quad (14)$$

where E and ν denote Young's modulus and Poisson's ratio, respectively.

B.5.3 Spherical inclusion problem

In order to demonstrate the capability of the measurement technique using the DVC and the LSCM, a non-uniform 3-dimensional deformation field near a hard spherical inclusion was measured under far-field uniaxial compressive loading. Confocal images near a 100 μm -diameter PMMA bead embedded within the agarose gel sample were recorded during incremental compressive loading. The nominal strain increment was approximately 3%. The scanning resolution was 512x512x512 voxels, and the scan spacing was 0.45 μm in all three directions. The confocal scanning volume near the embedded PMMA bead is illustrated in Figure B-9. Figure B-11 shows a vertical slice of the confocal image along the meridian plane of the PMMA bead at the undeformed configuration. The superimposed uniform grid of 16-voxels spacing represents the

locations where displacements measurements were conducted. The confocal images were analyzed by using the proposed DVC algorithm with a subvolume size of $64 \times 64 \times 64$ voxels. The contour maps in Figure B-13 represent constant contours of the horizontal (u_1) and the vertical (u_3) displacement components on the meridian plane. As expected, the dominant mode of the deformation was a constrained uniaxial compression along the x_3 -direction. The local distortion of the displacement contours near the PMMA bead indicated that the proposed DVC algorithm effectively captured non-uniform deformation fields near the spherical inclusion.

The experimentally measured displacement fields in Figure B-13 were compared to the analytical solution of the equivalent linear-elasticity problem. Most analytical elasticity solutions of the inclusion problem assume the continuity of displacement at the interface. Considering the high water content in the agarose gel and the large deformations in the sample, the perfect bonding condition is inadequate to accurately represent the present experiment. Using the solution of the sliding inclusion problem under uniaxial loading [30], the analytical solution of the sliding inclusion problem under the laterally-constrained uniaxial compressive loading was constructed by the superposition of three mutually-orthogonal uniaxial compression solutions as shown in Figure B-9. The contour maps in Figure B-15 show the horizontal and the vertical displacement fields of the constructed analytical solution. Qualitative comparisons of the contour maps in Figure B-13 and Figure B-15 indicate that the proposed DVC algorithm was well-suited for the full-field measurements of non-uniform deformation fields in three dimensions. It can be observed that the resolution of the lateral displacement field is

superior to the resolution in the vertical displacement, which is due to the blurring effect caused by the PSF along the optical axis (vertical direction).

A contour map of ϵ_{33} strain components near the inclusion is shown in Figure B-16 (a). At the bottom of the inclusion, a region of high strain concentration of up to 25% strain was visualized. Figure B-16 (b) displays the line-profile of the ϵ_{33} strain component along the central axis in x_3 -direction. The local compressive strain reaches the far field applied strain level at approximately one radius length away from the center of the bead. The high strain gradient will decrease the accuracy of the stretch-correlation by violating the assumption of uniform stretch deformation. In such cases, iterative applications of the DVC using a smaller subvolume will increase the accuracy of the measurements since each subvolume will be subjected to a more uniform stretch.

B.6 Conclusions

A novel experimental technique for measuring 3-dimensional large-deformation fields in soft materials has been developed. The technique utilizes the 3-dimensional measurement capability of the DVC algorithm in conjunction with the 3-dimensional imaging capability of confocal microscopy. Introduction of the stretch-correlation algorithm and the deconvolution algorithm greatly improved the strain measurement accuracy by providing better precision especially under large deformation. Also, the large-deformation measurement capability of the proposed DVC algorithm was successfully demonstrated by measuring a uniform deformation field for the case of simple uniaxial compression and a non-uniform deformation field surrounding the hard spherical inclusion. This new technique should prove itself particularly useful in

situations where local three dimensional strain non-uniformities need to be measured with high resolution. It is expected that the newly developed DVC technique will play a major role in characterizing time dependent cell interactions with its surrounding extracellular matrix including artificially engineered proteins [31], in three dimensions, which will provide valuable insights into the role of mechanical forces on biological processes.

B.7 Acknowledgements

We acknowledge the support provided by the National Science Foundation (DMR # 0520565) through the Center for Science and Engineering of Materials (CSEM) at the California Institute of Technology. GR acknowledges the support of the Army Research Office for providing the DURIP funds for the acquisition of the confocal microscope used in this study. GR gratefully acknowledges the Ronald and Maxine Linde Venture Fund that enabled the acquisition of instrumentation used in this investigation. We would like to thank Mr. Petros Arakelian for his valuable help with the experimental setup.

B.8 References

1. Ingber DE, Dike L, Hansen L, Karp S, Liley H, Maniotis A, McNamee H, Mooney D, Plopper G, Sims J, Wang N (1994) Cellular Tensegrity - Exploring How Mechanical Changes in the Cytoskeleton Regulate Cell-Growth, Migration, and Tissue Pattern During Morphogenesis. *International Review of Cytology - a Survey of Cell Biology* 150: 173-224.

2. Lo CM, Wang HB, Dembo M, Wang YL (2000) Cell movement is guided by the rigidity of the substrate. *Biophysical Journal* 79(1): 144-152.
3. Petronis S, Gold J, Kasemo B (2003) Microfabricated force-sensitive elastic substrates for investigation of mechanical cell-substrate interactions. *Journal of Micromechanics and Microengineering* 13(6): 900-913.
4. Wong JY, Velasco A, Rajagopalan P, Pham Q (2003) Directed movement of vascular smooth muscle cells on gradient-compliant hydrogels. *Langmuir* 19(5): 1908-1913.
5. Tan JL, Tien J, Pirone DM, Gray DS, Bhadriraju K, Chen CS (2003) Cells lying on a bed of microneedles: An approach to isolate mechanical force. *Proceedings of the National Academy of Sciences of the United States of America* 100(4): 1484-1489.
6. Gray DS, Tien J, Chen CS (2003) Repositioning of cells by mechanotaxis on surfaces with micropatterned Young's modulus. *Journal of Biomedical Materials Research Part A* 66A(3): 605-614.
7. Zaari N, Rajagopalan P, Kim SK, Engler AJ, Wong JY (2004) Photopolymerization in microfluidic gradient generators: Microscale control of substrate compliance to manipulate cell response. *Advanced Materials* 16(23-24): 2133-2137.
8. Cukierman E, Pankov R, Stevens DR, Yamada KM (2001) Taking cell-matrix adhesions to the third dimension. *Science* 294(5547): 1708-1712.
9. Even-Ram S, Yamada KM (2005) Cell migration in 3D matrix. *Current Opinion in Cell Biology* 17(5): 524-532.

10. Zaman MH, Kamm RD, Matsudaira P, Lauffenburger DA (2005) Computational model for cell migration in three-dimensional matrices. *Biophysical Journal* 89(2): 1389-1397.
11. Berfield TA, Patel HK, Shimmin RG, Braun PV, Lambros J, Sottos NR (2006) Fluorescent image correlation for nanoscale deformation measurements. *Small* 2(5): 631-635.
12. Luo PF, Chao YJ, Sutton MA, Peters WH (1993) Accurate Measurement of 3-Dimensional Deformations in Deformable and Rigid Bodies Using Computer Vision. *Experimental Mechanics* 33(2): 123-132.
13. Vendroux G, Knauss WG (1998) Submicron deformation field measurements: Part 2. Improved digital image correlation. *Experimental Mechanics* 38(2): 86-92.
14. Sutton MA, Cheng MQ, Peters WH, Chao YJ, McNeill SR (1986) Application of an Optimized Digital Correlation Method to Planar Deformation Analysis. *Image and Vision Computing* 4(3): 143-150.
15. Bay BK, Smith TS, Fyhrie DP, Saad M (1999) Digital volume correlation: Three-dimensional strain mapping using X-ray tomography. *Experimental Mechanics* 39(3): 217-226.
16. Roeder BA, Kokini K, Robinson JP, Voytik-Harbin SL (2004) Local, three-dimensional strain measurements within largely deformed extracellular matrix constructs. *Journal of Biomechanical Engineering-Transactions of the Asme* 126(6): 699-708.

17. Smith TS, Bay BK, Rashid MM (2002) Digital volume correlation including rotational degrees of freedom during minimization. *Experimental Mechanics* 42(3): 272-278.
18. Corle TR, Kino GS (1996) *Confocal scanning optical microscopy and related imaging systems*. Academic Press. San Diego: xv, 335 p.
19. Sheppard C, Shotton D (1997) *Confocal laser scanning microscopy*. BIOS Scientific; Springer, in association with the Royal Microscopical Society. Oxford; New York: xii, 106 p.
20. Chen DJ, Chiang FP, Tan YS, Don HS (1993) Digital Speckle-Displacement Measurement Using a Complex Spectrum Method. *Applied Optics* 32(11): 1839-1849.
21. Takita K, Aoki T, Sasaki Y, Higuchi T, Kobayashi K (2003) High-accuracy subpixel image registration based on phase-only correlation. *Ieice Transactions on Fundamentals of Electronics Communications and Computer Sciences* E86A(8): 1925-1934.
22. Hong S, Ravichandran G (2006) FFT-based digital image correlation algorithm for large deformation measurements. in preparation.
23. Born M, Wolf E (1970) *Principles of optics; electromagnetic theory of propagation, interference and diffraction of light*. (4th ed). Pergamon Press. Oxford, New York: xxviii, 808p.
24. Gu M (1996) *Principles of three dimensional imaging in confocal microscopes*. World Scientific. Singapore ; River Edge, NJ: xii, 337 p.

25. Lucy LB (1974) Iterative Technique for Rectification of Observed Distributions. *Astronomical Journal* 79(6): 745-754.
26. Torok P, Varga P, Booker GR (1995) Electromagnetic Diffraction of Light Focused through a Planar Interface between Materials of Mismatched Refractive-Indexes - Structure of the Electromagnetic-Field .1. *Journal of the Optical Society of America a-Optics Image Science and Vision* 12(10): 2136-2144.
27. Sheppard CJR, Torok P (1997) Effects of specimen refractive index on confocal imaging. *Journal of Microscopy-Oxford* 185: 366-374.
28. Visser TD, Oud JL, Brakenhoff GJ (1992) Refractive-Index and Axial Distance Measurements in 3-D Microscopy. *Optik* 90(1): 17-19.
29. Diaspro A, Federici F, Robello M (2002) Influence of refractive-index mismatch in high-resolution three-dimensional confocal microscopy. *Applied Optics* 41(4): 685-690.
30. Ghahremani F (1980) Effect of Grain-Boundary Sliding on Anelasticity of Polycrystals. *International Journal of Solids and Structures* 16(9): 825-845.
31. Welsh ER, Tirrell DA (2000) Engineering the extracellular matrix: A novel approach to polymeric biomaterials. I. Control of the physical properties of artificial protein matrices designed to support adhesion of vascular endothelial cells. *Biomacromolecules* 1(1): 23-30.

List of Tables

Table B-1. Standard deviation values for measured displacement and strain fields in the undeformed condition.

	Stationary	Translation
u_1 [voxel]	0.0605	0.1392
u_2 [voxel]	0.0541	0.1238
u_3 [voxel]	0.2106	0.6491
ϵ_{11} (%)	6.39×10^{-3}	4.18×10^{-2}
ϵ_{22} (%)	9.80×10^{-3}	4.96×10^{-2}
ϵ_{33} (%)	0.260	0.718

Table B-2. Mean and standard deviation values for measured strain fields under uniaxial compression.

	No stretch-correlation		Stretch-correlation	
	Mean	Standard deviation	Mean	Standard deviation
ϵ_{11} (%)	7.69×10^{-3}	7.07×10^{-2}	-3.55×10^{-2}	7.37×10^{-2}
ϵ_{22} (%)	1.14×10^{-2}	6.83×10^{-2}	7.75×10^{-2}	7.11×10^{-2}
ϵ_{33} (%)	-9.25	0.866	-9.34	0.392

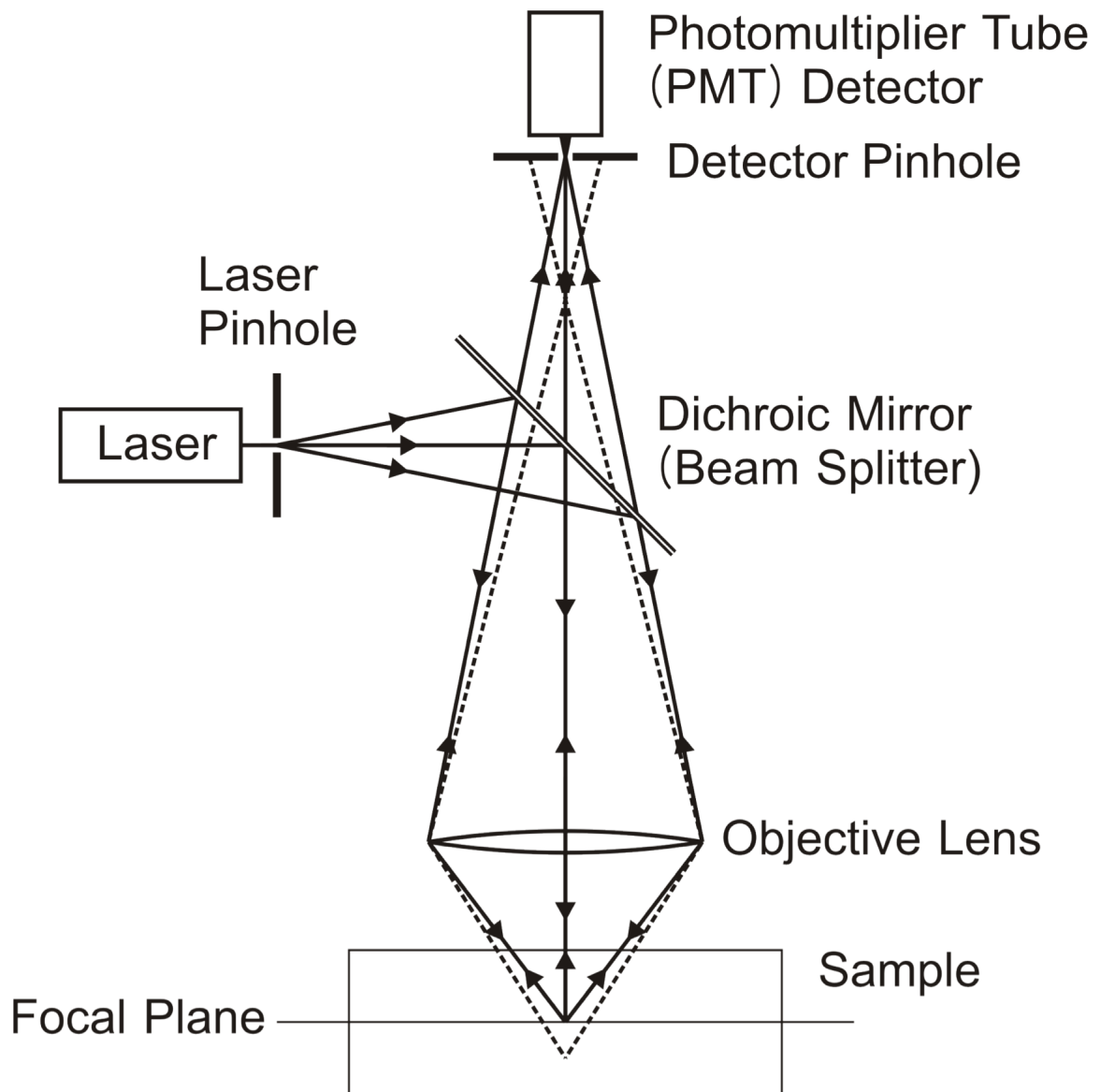


Figure B-1. Illustration of the confocal imaging principle
(solid lines = in-focus light; dashed lines = out-of-focus light)

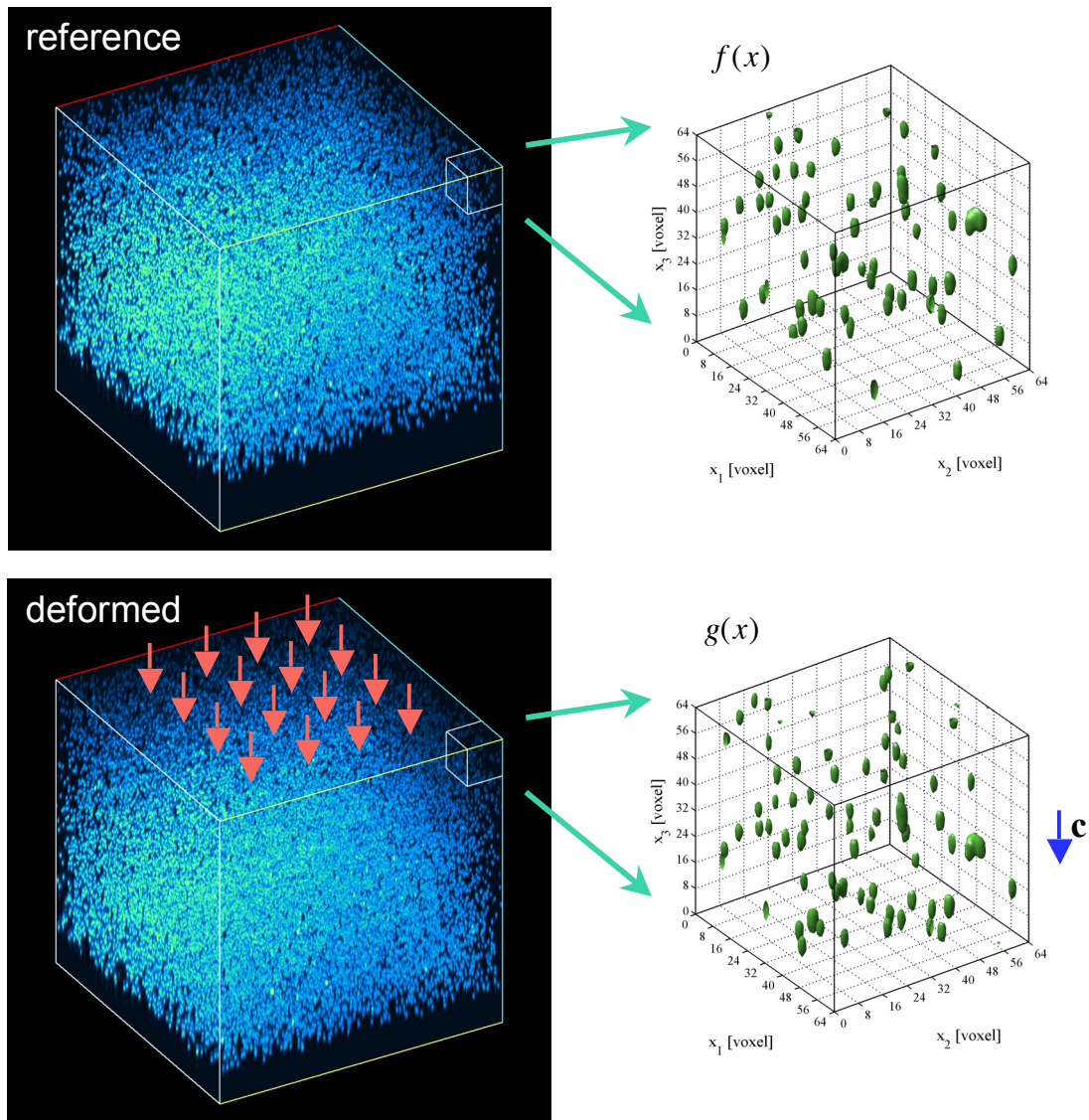


Figure B-2. Schematic illustration of the digital volume correlation (DVC)

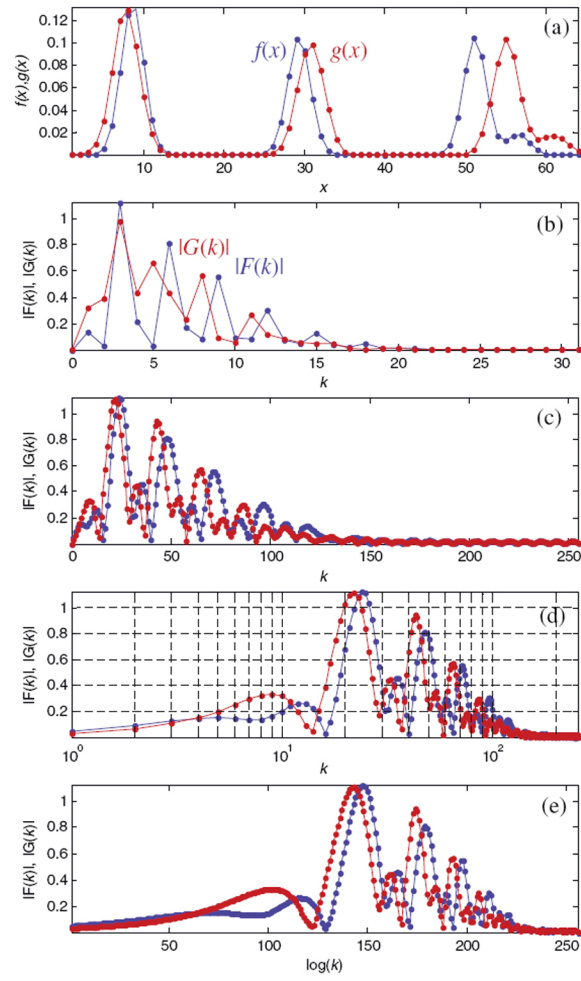
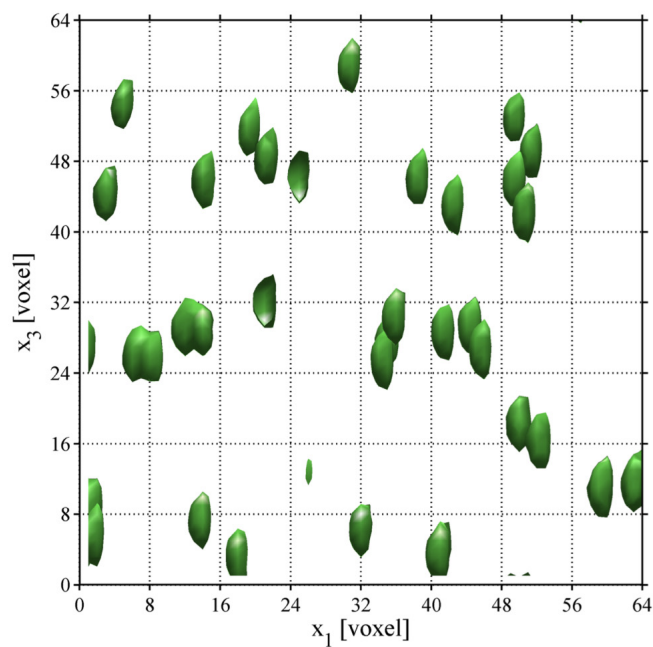
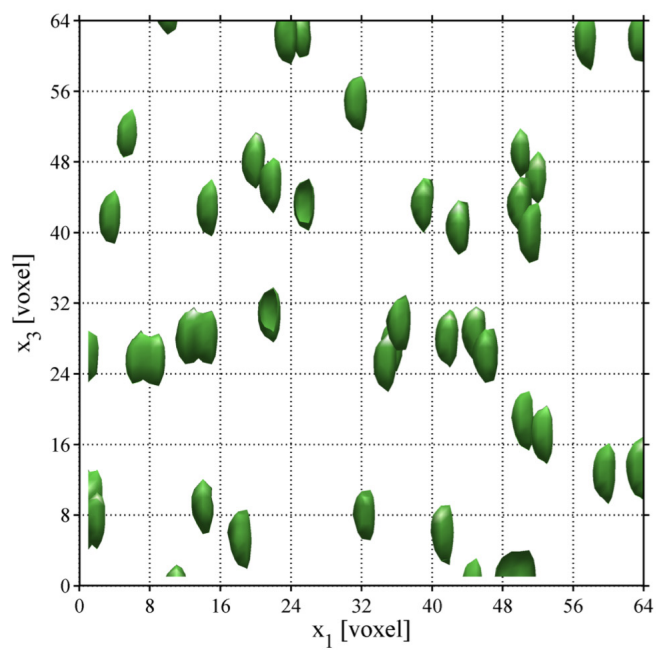


Figure B-3. One dimensional example of the stretch-correlation procedures



(a)



(b)

Figure B-4. 2-dimensional projection of confocal subvolume images
 (a) before and (b) after uniaxial compression of 10% in x_3 -direction.

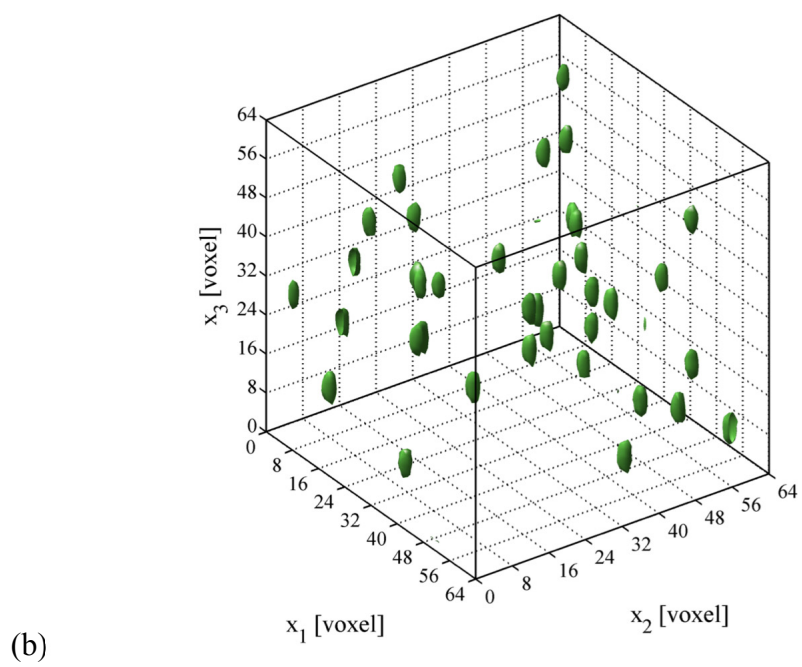
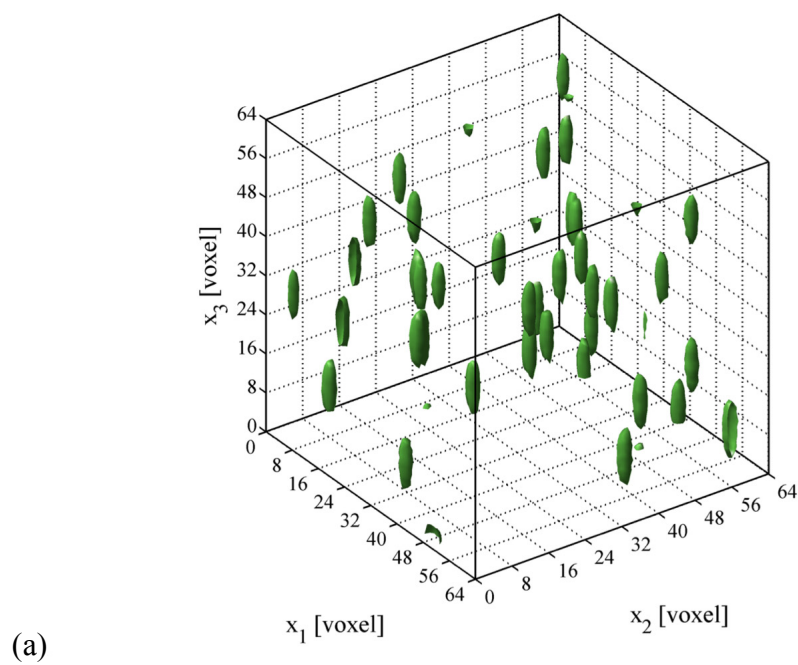


Figure B-5. Isosurface plots of confocal subvolume images
(a) before and (b) after deconvolution

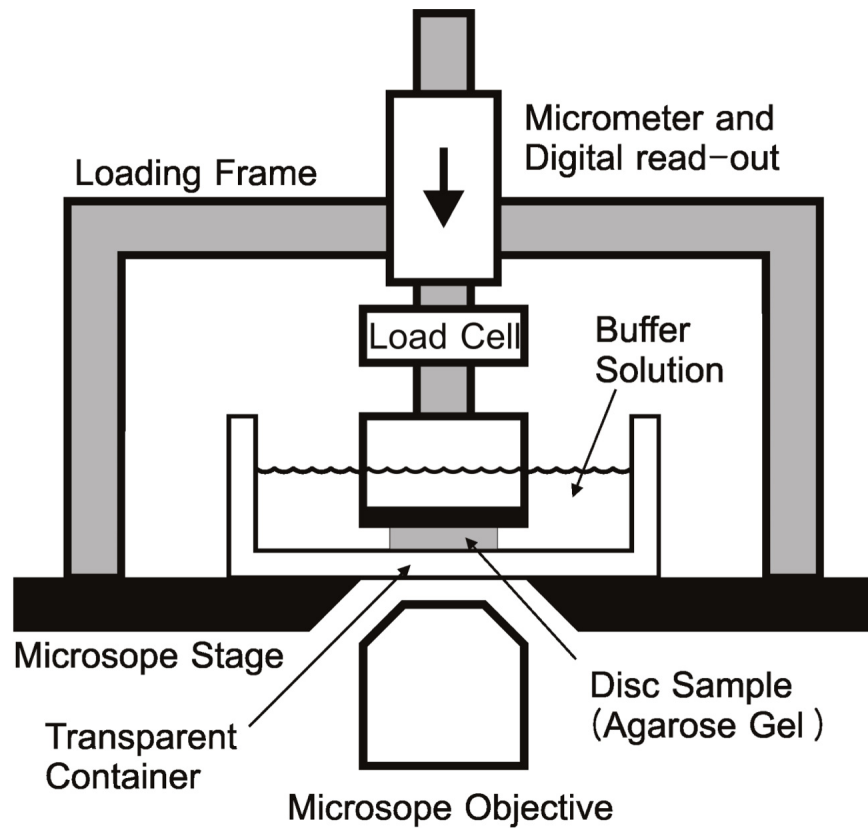


Figure B-6. Loading fixture for uniaxial compressive loading of soft materials

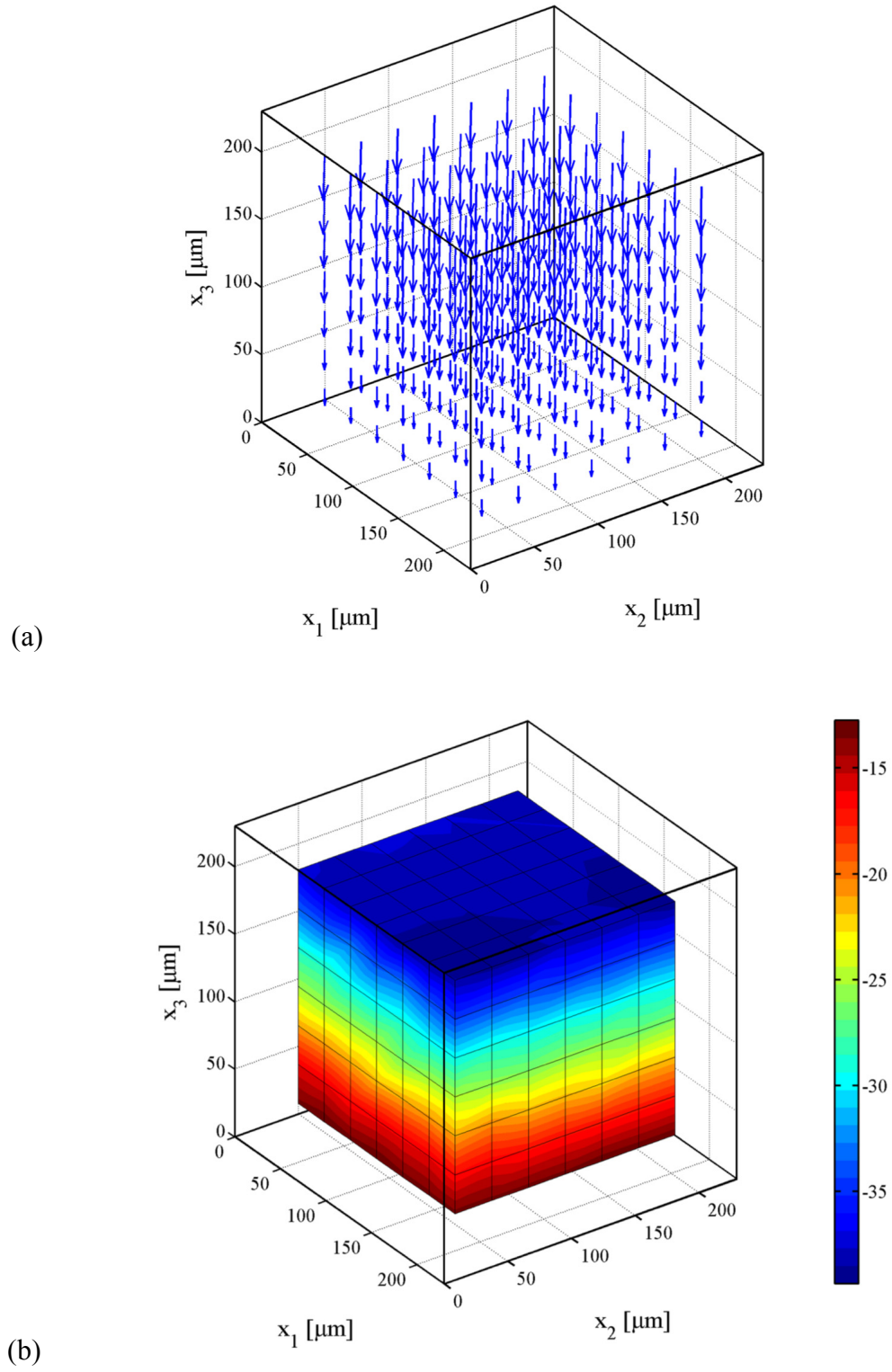


Figure B-7. Experimentally measured displacement fields under uniaxial compression
 (a) 3-dimensional displacement vector field and (b) vertical displacement field, u_3

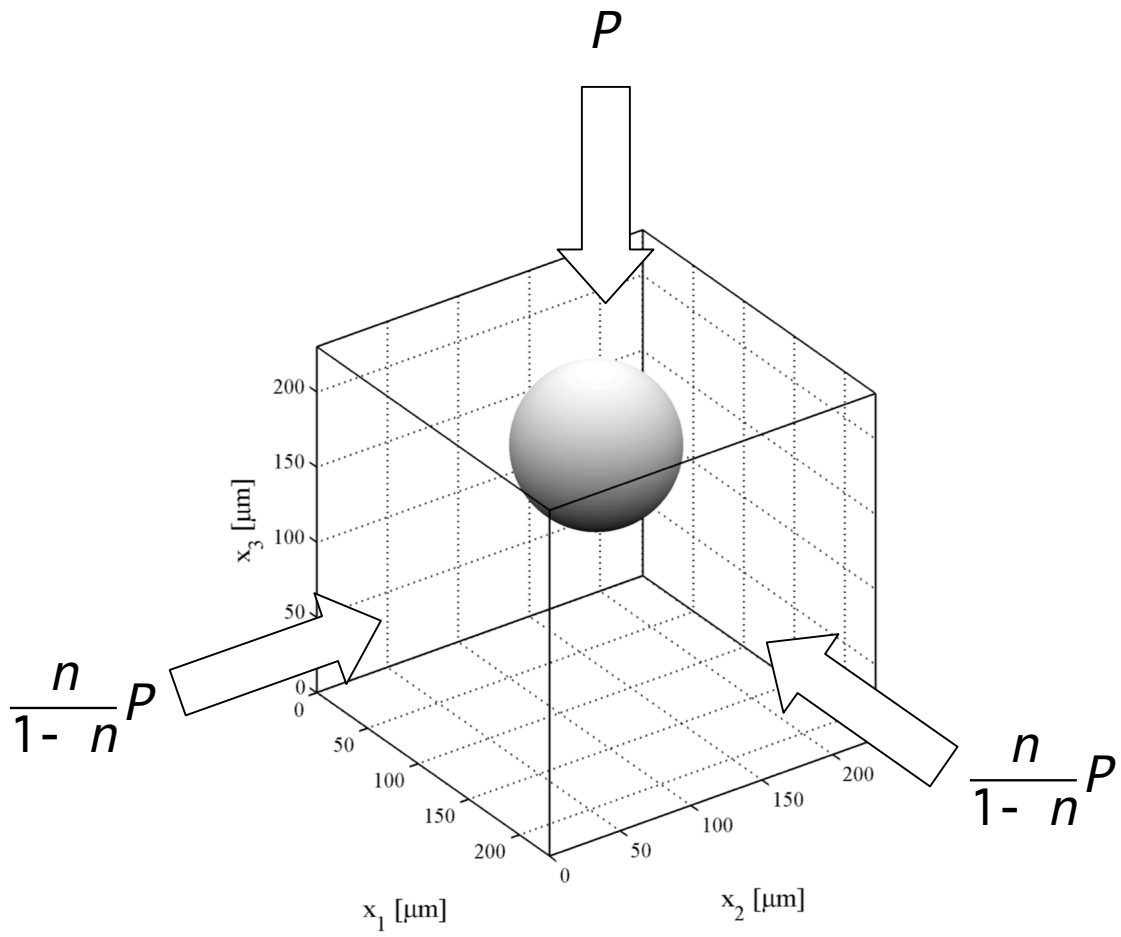


Figure B-8. Schematic of uniaxial constrained compression of a spherical inclusion in a matrix with a sliding interface

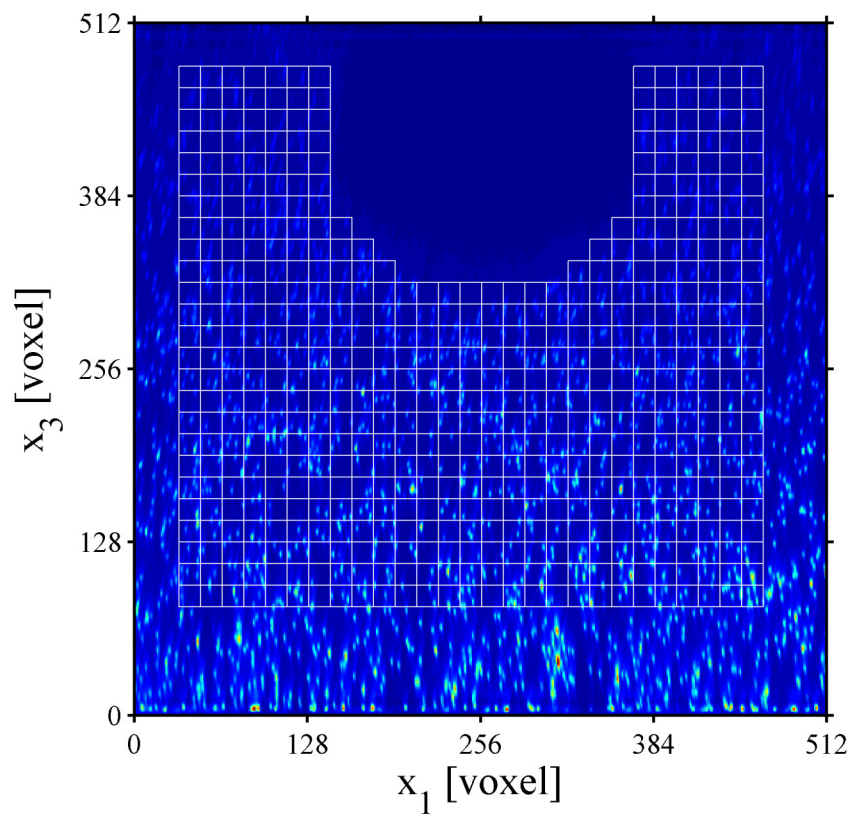
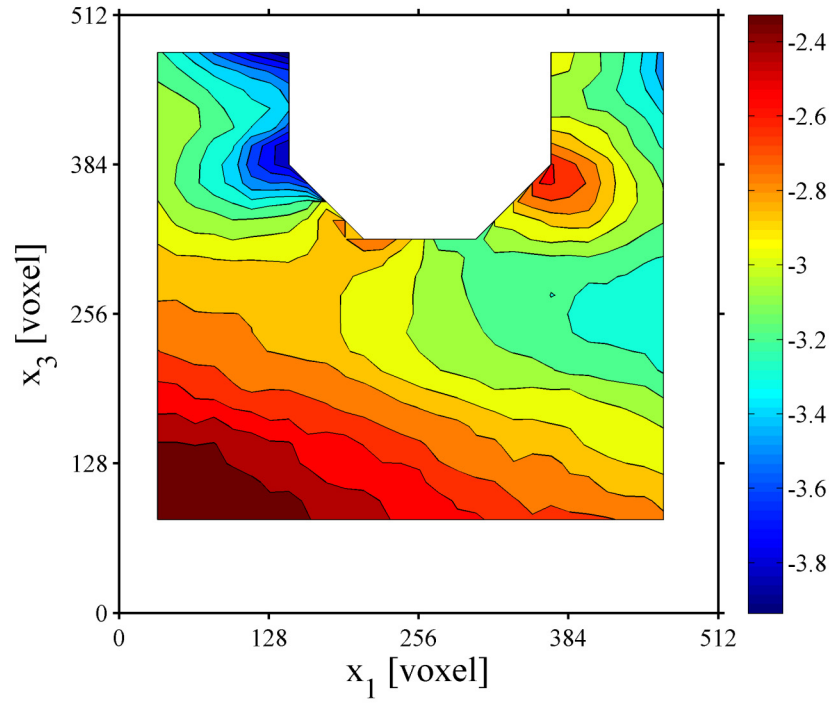
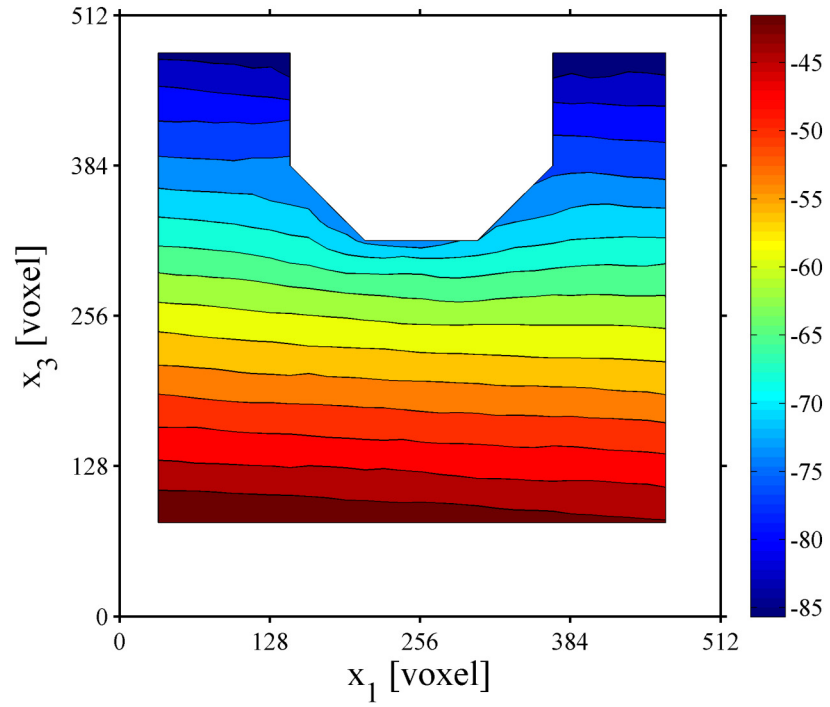


Figure B-9. A confocal slice along the meridian plane of an embedded 100 μm PMMA bead within the agarose sample



(a)



(b)

Figure B-10. Experimentally measured displacement fields near a spherical inclusion under uniaxial compression; (a) horizontal and (b) vertical displacement components

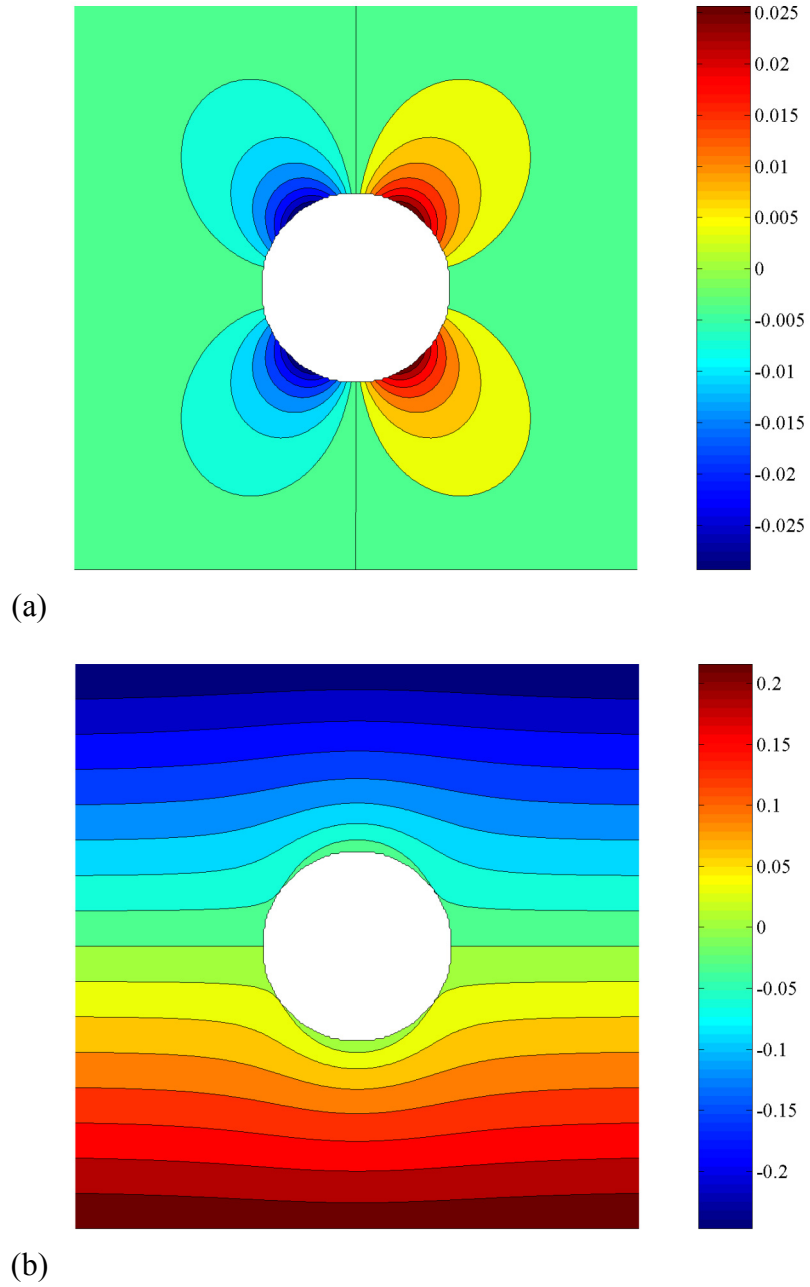
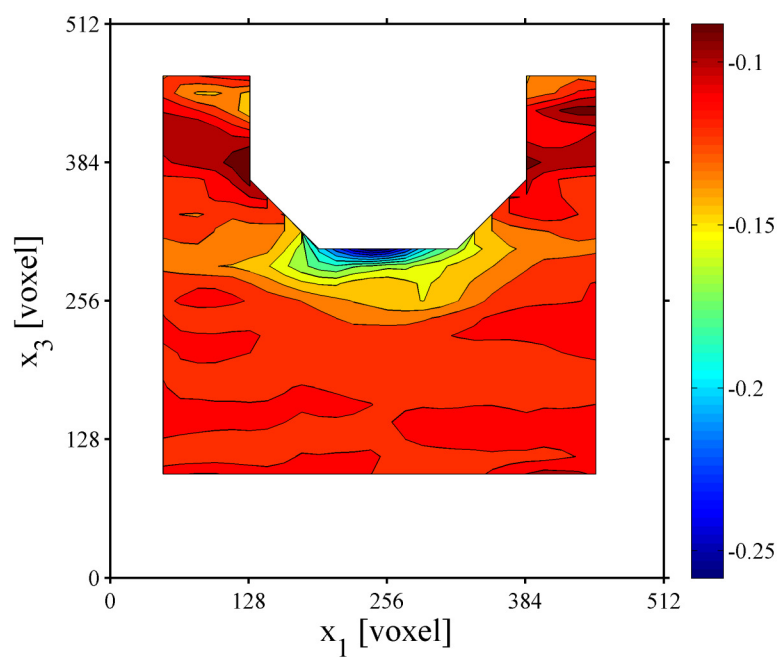
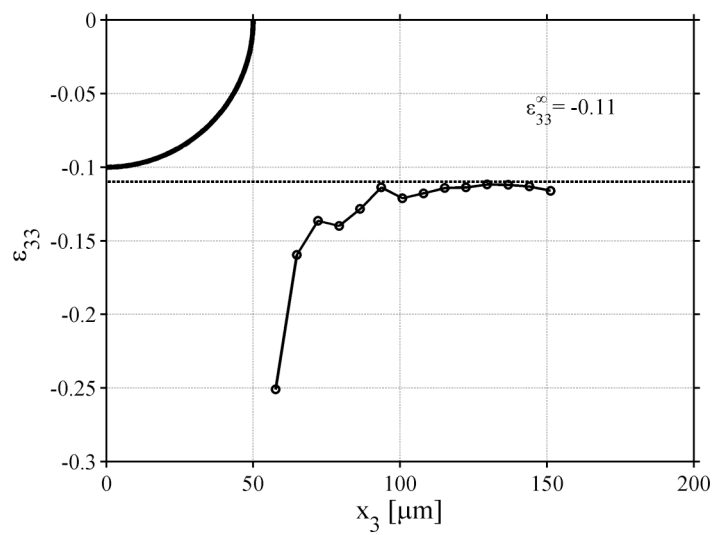


Figure B-11. Analytical displacement fields near a rigid inclusion with a sliding interface under uniaxial constrained compression; (a) horizontal and (b) vertical displacement components



(a)



(b)

Figure B-12. Experimentally measured strain fields ϵ_{33} near a spherical inclusion under uniaxial compression.

Appendix C

Strain/Plasmid Collection

<u>Bacterial Expression Strain:</u>	AF Phenylalanine auxotrophic <i>E. coli</i> derived from BL21(DE3)
<u>Genotype:</u>	<i>HsdS gal(λcIts857 ind 1 Sam7 nin5 lacUV5-T7 gene 1) pheA</i>
<u>Reference:</u>	Yoshikawa E, Fournier MJ, Mason TL, Tirrell DA. <i>Macromolecules</i> 1994. 27: 5471-5475.
<u>Submitted by:</u>	Stacey Maskarinec (March 2009)
<u>Strain name:</u>	AF pETRW-[RGD-(ELF) ₅] ₃ -PheRS
<u>Strain name:</u>	AF pETRW-[RDG-(ELF) ₅] ₃ -PheRS
<u>Sequence:</u>	See provided sequences. pETRW-[RGD-(ELF) ₅] ₃ -PheRS (p. 208-210) pETRW-[RDG-(ELF) ₅] ₃ -PheRS (p. 211-213)

[illegible]

